FEDERAL UNIVERSITY OF SANTA CATARINA
JOINVILLE TECHNOLOGY CENTER
AEROSPACE ENGINEERING B.S.

LILLIAN RODRIGUES

ANALYTICAL MODEL OF THE TEMPERATURE DISTRIBUTION IN THE CUTTING TOOL FOR ORTHOGONAL CUTTING PROCESS

Joinville
2022

LILLIAN RODRIGUES

ANALYTICAL MODEL OF THE TEMPERATURE DISTRIBUTION IN THE CUTTING TOOL FOR ORTHOGONAL CUTTING PROCESS

This bachelor thesis is presented to fulfill the partial requirement to obtain the tittle of bachelor in the course of Aerospace Engineering at the Joinville Technology Center from the Federal University of Santa Catarina.

Advisor: Prof. Dr. Maurício de Campos Porath

Co-advisor: M. Sc., Hiu Liu

Joinville
2022

LILLIAN RODRIGUES

ANALYTICAL MODEL OF THE TEMPERATURE DISTRIBUTION IN THE CUTTING TOOL FOR ORTHOGONAL CUTTING PROCESS

Este Trabalho de Conclusão de Curso foi julgado adequado para obtenção do título de bacharel em Engenharia Aeroespacial, na Universidade Federal de Santa Catarina, Centro Tecnológico de Joinville.

Joinville (SC), 14 de março de 2022.

Banca Examinadora:

_____

Prof. Dr. Maurício de Campos Porath
Orientador
Presidente

_____

Prof. Dra. Talita Sauter Possamai
Membra
Universidade Federal de Santa Catarina

_____

Prof. Dr. Adriano Fagali de Souza
Membro
Universidade Federal de Santa Catarina

ACKNOWLEDGEMENTS

I would like to thank Werkzeugmaschinenlabor der RWTH Aachen (Laboratory for Machine Tools and Production Engineering WZL of RWTH Aachen University) for the opportunity to work as a student assistant, funding my studies, and encouraging me to apply, improve and develop different concepts seen throughout my graduation course.

Furthermore, I would like to thank my mentor in Brazil, Professor Maurício de Campos Porath, for the possibility of my first contact with the institute. I also would like to thank my supervisor Hui Liu, whose experience and understanding have made it possible to make significant progress with precision and reliability in many kinds of research over the last months. These properties will undoubtedly be considered as a model for me from now on.

I also acknowledge Professor Alexandre Mikowiski, who presented me with the first opportunity for undergraduate research. I must also remember Professor Gary B. Hughes, for the opportunity to participate in a NIAC project. I thank Professor Helton da Silva Gaspar and Professor Diogo Merguizo Sanchez who contributed to enhancing my acknowledgments to develop undergraduate research at the National Institute for Space Research. I also would like to thank all my professors who have taught and challenged me to always seek the best.

I am grateful for my friends from Brazil, but also for the friendships that I made in Aachen that became for life. I thank my boyfriend, Marcos Pereira Campos, who always have supported and encouraged me. Finally, I would like to thank my family, who are present even far away for all the encouragement and teachings that have been given to me so far.

What we know is not much.
What we do not know is immense.
– Pierre-Simon Laplace.

RESUMO

Este trabalho apresenta um modelo analítico do campo de distribuição de temperatura da ferramenta para o processo de corte com uma nova consideração de limite geométrico em relação aos modelos atuais presentes na literatura. A maior parte da energia mecânica durante o corte de metais é convertida em energia térmica. Dessa forma, muitos problemas, tais como distribuição de tensão térmica, queima da superfície e desgaste da ferramenta podem ser causados pelo calor excessivo gerado durante o processo de corte. Além disso, em processos de usinagem de corte intermitentes, as ferramentas são submetidas a um aquecimento cíclico, e podem falhar devido a mecanismos de fadiga térmica. Uma análise precisa da temperatura de corte é uma base possível para prever e entender melhor os principais problemas do corte de metal. A modelagem dos processos de corte permite melhorar a produtividade dos processos e a economia de custos, otimizando as condições de corte e evitando ou reduzindo a necessidade de realizar testes experimentais onerosos. Dessa forma, o principal objetivo deste trabalho de conclusão de curso é contribuir para a pesquisa de modelagem para o processo de corte, desenvolvendo um modelo analítico com a função de Green para condições de contorno finitas e tridimensionais, a fim de prever os campos de temperatura variáveis no tempo da ferramenta. Com essa finalidade, o modelo analítico será comparado com modelos térmicos presentes no estado da arte da tecnologia de corte para o estado estacionário e o estado transiente. Além disso, experimentos ortogonais de corte foram conduzidos para validar o modelo desenvolvido, em que apresentaram menos de 6% de erro relativo para a ponta da ferrmenta. Após boa concordância dos resultados, foi possível aplicar este modelo a um processo de corte de fresamento.

Palavras-chave: Solução térmica analítica. Função de Green. Condições de contorno finitas. Corte ortogonal. Fresamento.

ABSTRACT

This work presents an analytical model of the tool temperature distribution field for the cutting process with a new geometrical boundary assumption regarding the current models in the literature. Most of the mechanical energy during metal cutting is converted into thermal energy. Besides, many serious problems such as thermal stress distribution, surface burning, work hardening and tool wear can be induced by the excessive cutting heat generated during the cutting process. Furthermore, in interrupted processes tools are subjected to cyclic heating, and may fail by thermal fatigue mechanisms. An accurate analysis of the cutting temperature is a possible basis for predicting and better understanding the main metal cutting issues. Modeling of cutting processes allows the productivity of cutting processes and costs savings to be improved by optimizing cutting conditions and by avoiding or reducing the need to perform costly and laborious experimental tests. Thus, the main objective of this bachelor thesis is to contribute to the research of modeling for the cutting process, developing an analytical model with finite three-dimensional Green's Function in order to predict time-variant temperature fields in the tool. For this purpose, this analytical model will be compared to previous thermal models in the cutting technology's state of the art for the stationary and the transient state. Moreover, orthogonal cutting experiments were conducted to validate the model developed, which presented less than 6% of relative error for the edge of the tool. Finally, after good accordance of the results, it was possible to accomplish a step forward to apply this model to a milling process.

Keywords: Analytical thermal solution. Green's function. Finite boundaries assumption. Orthogonal cutting. Milling.

LIST OF FIGURES

LIST OF TABLES

LIST OF ABBREVIATIONS

CFRP – Carbon Fiber Reinforced Plastics
FOV – Field of View
GF – Green's Function
GFs – Green's Functions
GFSE – Green's Function Solution Equation
GFSE-3D – Green's Function Solution Equation for Three-Dimensional Body
IR – Infrared
PCC – Phantom Camera Control
TC – Thermocouple

LIST OF SYMBOLS

α	Thermal diffusivity	$[m/s]$
α_F	Flank angle	$[rad]$
β	Wedge angle	$[rad]$
γ	Rake angle	$[rad]$
γ_s	Cutting edge inclination	$[rad]$
λ	Thermal conductivity	$[W/(m.K)]$
$\lambda_{1,2}$	Wavelength band	$[\mu m]$
ϕ	Shear angle in orthogonal cutting/ Cutter rotation angle in milling	$[rad]$
ϕ_c	Contact angle in milling process	$[rad]$
ϕ_{ex}	Cutter exit angle in milling process	$[rad]$
ϕ_{st}	Cutter entry angle in milling process	$[rad]$
ρ	Density	$[kg/m^3]$
θ_M	Temperature rise at a point M	$[^\circ C]$
$\theta_{t,f}$	Apparent temperature	$[^\circ C]$
a_e	Width of cut in milling process	$[m]$
a_p	Depth of cut in milling process	$[m]$
A_γ	Trace of the plane of rake face	
A_α	Trace of the plane of flank face	
A'_α	Minor flank face	
B	Heat partition ratio	
d	Distance of the median plane from the lateral face	$[m]$
D	Characteristic dimension	$[m^{1/2}]$
$F(x, y, z, 0)$	Initial temperature	$[^\circ C]$

F_a	Active force in milling process	$[N]$
F_a	Active force in milling process	$[N]$
F_c	Cutting force	$[N]$
F_{cn}	Cutting normal force in milling process	$[N]$
F_f	Friction force	$[N]$
F_{fn}	Cutting feed force in milling process	$[N]$
F_n	Normal force	$[N]$
F_s	Shear force	$[N]$
F_p	Passive force	$[N]$
F_t	Thrust force	$[N]$
f_z	Feed per tooth in the milling process	$[m]$
$G(r,t\|r',\tau)$	Green's Function	$[^\circ C]$
G_{XIJ}	Green's Function to the rectangular coordinate type of boundary condition I and J.	$[^\circ C]$
G_{X22}	Green's Function for the second kind's boundary condition.	$[^\circ C]$
h	Uncut chip thickness or depth of cut	[m]
$h(\phi)$	Undeformed chip thickness in milling process	[m]
h_{max}	Maximum undeformed chip thickness in milling process	[m]
k	Heat conductivity	$[W/(m.K)]$
k_r	Cutting edge angle	$[rad]$
K_0	Bessel function of the second kind, order zero	
l_c	Cutting length	[m]
L	Thickness of a finite body	$[m]$
L_f	Contact length between chip and tool on the rake face	$[m]$
L_s	Shear length	[m]
R	Total cutting force	$[N]$

$R^{'}$	Total cutting force in the opposite direction	$[N]$
S	Major cutting edge	
S'	Minor cutting edge	
P_c	Cutting power duo to the cutting force in the milling process	$[W]$
P_f	Working plane	
P_o	Tool orthogonal plane	
P_p	Tool back plane	
P_r	Tool reference plane	
P_s	Tool cutting edge plane	
P_{total}	Cutting power in the milling process	$[W]$
$\dot{q}''$	Heat flux	$[W.m^{-2}]$
q_f	Heat flux generated at the tool-chip interface	$[W.m^{-2}]$
q_s	Heat flux generated on the shear plane	$[W.m^{-2}]$
$\dot{Q}_{chip}$	Heat flow in the chip	$[W]$
Q_{pt}	Heat flux at a point	$[W]$
$\dot{Q}_{tool}$	Heat flow in the tool	$[W]$
$\dot{Q}_{workpiece}$	Heat flow in the workpiece	$[W]$
t	Time	$[s]$
t_{ch}	Deformed chip thickness	$[m]$
$T(r,t)$	Temperature distribution	$[^{\circ}C]$
U_{st}	Increment of the temperature of a semi-infinite solid due to a stationary rectangular heat source	$[^{\circ}C]$
v	Velocity of the moving heat source	$[m/s]$
v_c	Cutting velocity in the milling process	$[m/s]$
v_f	Feed speed in the milling process	$[m/s]$
V_c	Cutting speed in the orthogonal cutting process	$[m/s]$

V_{ch}	Chip velocity	$[m/s]$
V_e	Effective speed in the orthogonal cutting process	$[m/s]$
V_f	Feed speed in the orthogonal cutting process	$[m/s]$
V_s	Shear velocity	$[m/s]$
w	Width of cut	$[m]$
W	Width of workpiece	$[m]$
x	Coordinate of x-axis	$[m]$
X	Thickness of the rectangular parallelepiped's x-axis	$[m]$
y	Coordinate of y-axis	$[m]$
Y	Thickness of the rectangular parallelepiped's y-axis	$[m]$
y_q	Position of the q imaginary heat source	$[m]$
z	Coordinate of z-axis	$[m]$
Z	Thickness of the rectangular parallelepiped's z-axis	$[m]$

SUMMARY

1 INTRODUCTION

During a cutting process, the mechanical energy from the plastic deformation developed at the primary shear plane and the chip–tool interface is converted into heat. Studies have shown that the chip and the environment dissipate a great deal of this heat while the reminiscent is conducted into the workpiece and the cutting tool. However, this small quantity of heat conducted into the tool is enough to create high temperatures near the cutting edges, which in the same cases can reach the level of 1100 $^{\circ}C$ (ONYECHI; OLUWADARE; OBUKA, 2013). As a result, various serious problems such as thermal stress distribution, surface burning, work hardening, and tool wear can be caused by the excessive cutting heat generated during the cutting process. Furthermore, the cutting heat has a potential to affect the fatigue life and machining distortion of thin-walled titanium alloy parts, especially those used in the aerospace field (CHENWEI et al., 2019).

The combined effect of the thermal and mechanical loads directly affects the stress field during the cutting process. In addition, residual stresses affect the surface integrity (MAGDA, 2008). In the literature, the term "surface integrity" was suggested to indicate the surface characteristics that influence the part functionality, such as surface roughness, residual stresses and microstructure (CAPELLO, 2005). According to a Boeing report from 2001, the total cost of rework and scrap due to residual stress-related machining distortion for four different aircraft types was $290 million (LANDWEHR, 2021). As Ma et al. (2016) presented, cutting forces and cutting temperature might be useful in predicting the machining-induced residual stress.

Furthermore, the tool temperature is an important parameter needed to determine tool life and wear (RADULESCU; KAPOOR, 1994). Diffusion between tool and workpiece at the tool-chip interface is one of the primary causes of wear mechanisms that is dependent on temperature (ISLAM, 2018). Consequently, accurate analysis and measurement of the cutting temperature is a possible basis for predicting the residual stress and the other consequences in machining (CHENWEI et al., 2019). For this purpose, techniques like numerical simulation, analytical and experimental methods have been used for the prediction of cutting temperatures (BHIRUD; GAWANDE, 2017).

Modeling cutting processes is an essential tool for virtual manufacturing because it allows the productivity of cutting processes and cost savings to be improved by optimizing cutting conditions and avoiding or reducing the need to perform costly and laborious experimental tests. In recent years, there has been significant progress in the development of models to predict cutting forces, machining vibrations and thermal damage. Cutting temperatures are one of the limiting factors in cutting processes due to their impact on the thermal damage of machined workpieces, the generation of tensile residual stresses, tool wear etc. Thus, modeling and prediction of cutting temperatures have become of great interest since it allows for a better understanding of

main metal cutting issues (VEIGA et al., 2021). Compared with numerical simulation methods, analytical models have the advantage of being able to provide a clear description of the cutting mechanism (CHENWEI et al., 2019).

Cutting is a manufacturing process with strongly interconnected thermal and mechanical physics, which are until today a challenge to understand. Whereas modeling the temperature can predict thermal issues during the cutting process and save costs. With this motivation, in this bachelor thesis, it is presented an analytical model of the temperature distribution in the tool for the orthogonal cutting process. A comparative study of analytical thermal models, which are present in the literature, to predict the orthogonal cutting temperature is conducted to analyze the model developed in this work. Moreover, orthogonal experimental tests were realized to validate the new analytical model's results. After its validation, the last procedure was to apply the methodology to the milling process, aiming to show its usability for the industry.

This bachelor thesis is organized as follows: the theoretical fundamentals of the cutting process and the existing thermal models are reviewed in Chapter 2. The methodology of the analytical models and the experiments are presented in Chapter 3. The results are discussed in Chapter 4, followed by the conclusion and outlook in Chapter 5.

1.1 GENERAL OBJECTIVE

The main objective of this work is to develop a new analytical model of the tool temperature distribution based on Green's Function with a finite boundary assumption for the orthogonal cutting process.

1.2 SPECIFIC OBJECTIVES

The specific objectives are:

- Implementing the analytical models from the previous cutting technology's literature to calculate the tool temperature in the cutting processes for the transient and steady-state;
- Defining a new geometrical boundary assumption for the tool and demonstrate the equations to be used to describe a new analytical model to calculate the tool temperature in orthogonal cutting for transient state;
- Presenting a comparative study of the analytical thermal models to predict the orthogonal cutting temperature;
- Validating the analytical model developed in this bachelor thesis with orthogonal cutting experiments in order to attest its reliability and accuracy;
- Applying the methodology of the analytical model's temperature field in the cutting tool to the milling process.

2 STATE OF THE ART

For the purpose of understanding the contents discussed in this work, some essential foundations are presented. Firstly, it is given an introduction of the machining mechanism and in the sequence is explained the mechanics of the orthogonal cutting and milling process. Further, a review of the analytical models for steady-state and transient temperatures in the literature and the main aspects of its theory is introduced. Hence, two Sections will be presented: one for orthogonal cutting, based on Jeager's Solution; and another for interrupted cutting, based on Green's Function. Concluding, methods for measuring the temperatures in cutting processes are provided.

2.1 CUTTING PROCESS

Machining is an essential manufacturing operation in the industry. The purpose of a machining process is to generate a surface with a specified shape and acceptable surface finish and prevent tool wear and thermal damage that leads to geometric inaccuracy of the finished part (ONYECHI; OLUWADARE; OBUKA, 2013).

Besides, DIN (2003) classifies machining as all process variants of the main group "Cutting", in which form is altered by means of reducing material cohesion. This deformation is achieved through a relative motion between the tool and the workpiece that generates energy transfer. In addition, Klocke e Kuchle (2011a) defines the term "machining" in the sense of cutting with geometrically defined cutting edges. All processes in the group of geometrically defined cutting edges have in common that it is used a tool, which the cutting edge number, geometry, and position to the workpiece are determined.

The cutting part is the active part of the tool where the cutting wedges are located with the cutting edges. The idealized cutting wedge is comprised of two faces: A rake face and a flank face, which cut in a line, cutting edge S. The angle between these two faces is designated as the wedge angle β. Figure 1 shows an idealized cutting wedge. Up to this point, the concepts have been explained using a simple cutting wedge formed by two faces. Generally, more complex tools are used, composed of several cutting wedges, in the simplest case of one major cutting wedge and one minor cutting face as shown in Figure 2 (KLOCKE; KUCHLE, 2011a).

All the basic process variants of cutting can all be subdivided into two categories:

a) Uninterrupted cut;
b) Interrupted cut.

The interrupted cut is the general variant among them, in which the cut takes place only intermittently. In the case of the uninterrupted cut, temporal interruption is infinitely small, i.e.,

Figure 1 – Description of the cutting wedge in the cutting process.

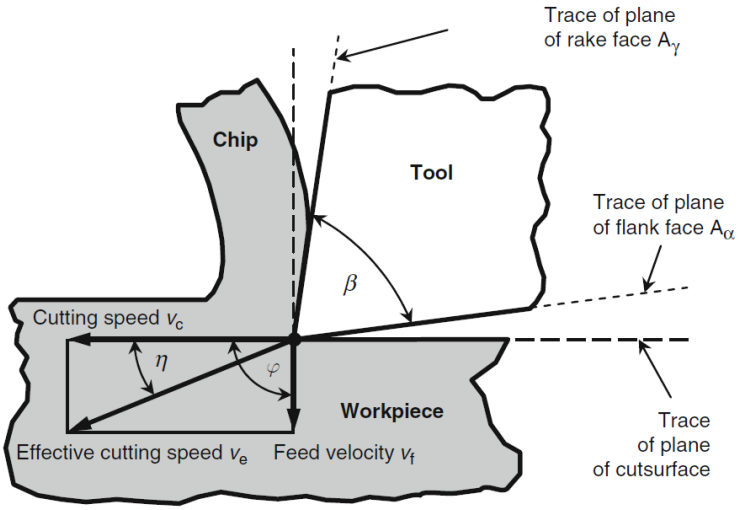

Source: (KLOCKE; KUCHLE, 2011a).

Figure 2 – Cutting edges and faces of the wedge in the cutting process.

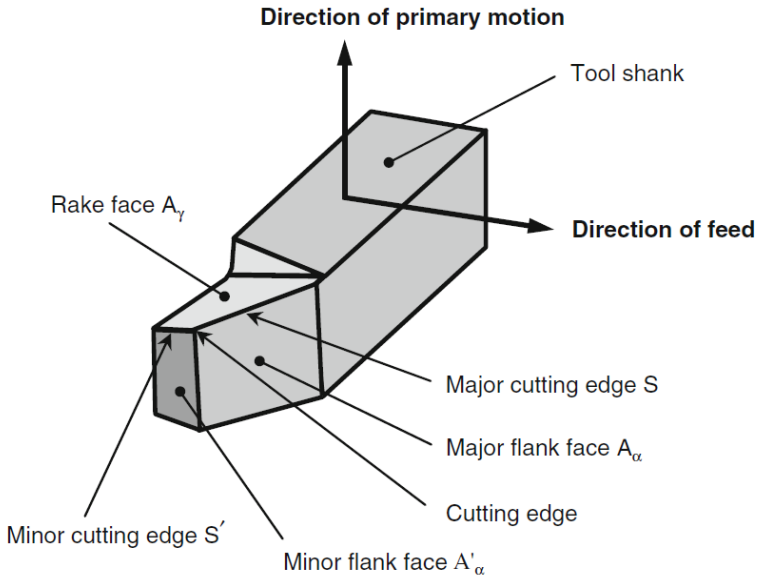

Source: (KLOCKE; KUCHLE, 2011a).

the cut is continuous (KLOCKE; KUCHLE, 2011a).

Despite a large number of cutting process variants, they can be further extended by three main categories (KLOCKE; KUCHLE, 2011a):

a) free, orthogonal cuts (Figure 3);
b) free, diagonal cuts (Figure 3);
c) bound, diagonal cuts.

Figure 3 – (a) Free, orthogonal and (b) free, diagonal cut.

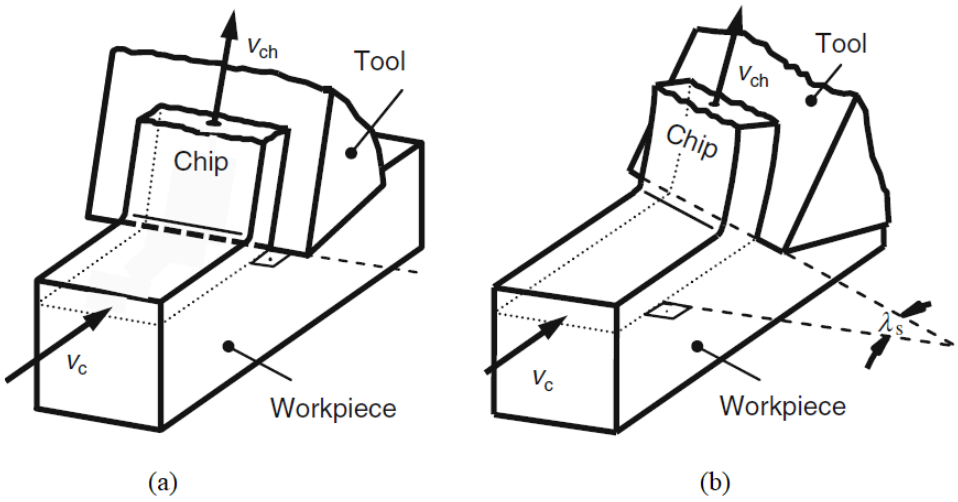

Source: (KLOCKE; KUCHLE, 2011a).

2.1.1 Orthogonal Cutting

In this work, it will be studied the free, orthogonal cut case, which can be brought about by the following marginal conditions (KLOCKE; KUCHLE, 2011a):

a) Only the major cutting edge is being engaged (free);
b) The tool cutting edge angle k_r is $90°$ (orthogonal);
c) Tool cutting edge inclination γ_s is equal to $0°$ (orthogonal).

Therefore, orthogonal cutting occurs when the cutting tool is perpendicular to the direction of tool motion. Moreover, the direction of chip flow is perpendicular to the direction of movement of the cutting edge. The chip formation takes place by the process of intense plastic shearing in a region known as the primary shear zone extending from the tip of the cutting tool to the free surface, as indicated in Figure 4. The chip has a freshly created and thus clean surface, and as it flows up the rake face of the tool, it is subject to a very high normal stress. Under these conditions, strong adhesion may occur between chip and tool, giving rise to additional shear in the chip region adjacent to the tool surface known as the secondary shear zone (LIEW; HUTCHINGS; WILLIAMS, 1998).

Orthogonal cutting is a cutting process in which the straight edge of a wedge-shaped cutting tool is moved relative to a workpiece with a cutting speed V_c perpendicular to the cutting edge (Figure 5a). Two angles define the tool geometry: rake angle γ and flank angle α_F, as shown in Figure 5b. This figure shows a cross-section of the workpiece, chip and tool through the median plane (Figure 5a) (VEIGA et al., 2021).

In orthogonal cutting, the cutting edge is positioned at a depth below the workpiece surface to remove a layer of the workpiece. The depth of cut corresponds to the uncut chip thickness h . The simplest cutting model assumes that the chip is formed along a plane named the shear plane or primary deformation zone, with shear length L_s (Figure 5b). The shear plane

Figure 4 – Geometry of the orthogonal cutting: Primary and secondary shear zone.

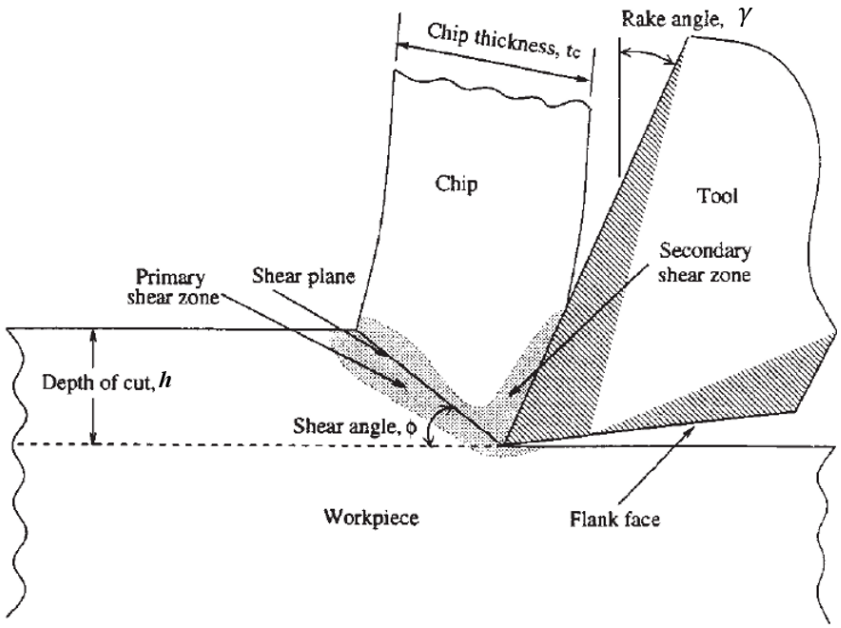

Source: adapted from (LIEW; HUTCHINGS; WILLIAMS, 1998).

forms an angle ϕ with the direction of cutting speed V_c , while the shear deformation of the material layer at the shear plane forms a chip with a larger deformed chip thickness t_{ch}. The chip then slides over the tool rake face along a distance named L_f (VEIGA et al., 2021).

Figure 5 – (a) Geometry of orthogonal cutting process. (b) Cross-section by the median plane.

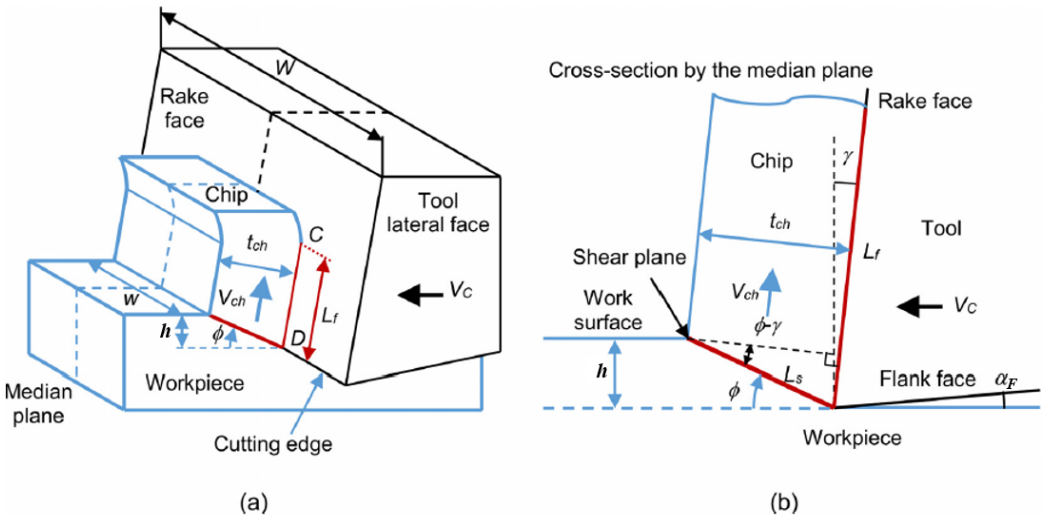

Source: (VEIGA et al., 2021).

Merchant (1945) in the early 1940s developed a model of the metal cutting process that culminated in the development of what is popularly known as a Merchant Circle or a condensed force diagram. This diagram shows the relationships between various force components, velocity components, and angle relationships (KOMANDURI, 1993), as shown in Figure 6 at the upper

right side and in Figure 8.

In addition to cutting speed V_c, which was already presented before, two other velocities are involved in the cutting process: shear velocity V_s (Equation 1) and chip velocity V_{ch} (Equation 2) (MERCHANT, 1944). These velocities can be analyzed in Figure 6.

$$V_s = V_c \frac{cos(\gamma)}{cos(\phi - \gamma)} \tag{1}$$

$$V_{ch} = V_c \frac{sin(\gamma)}{cos(\phi - \gamma)} \tag{2}$$

Figure 6 – Cutting speeds and forces and at the orthogonal cutting.

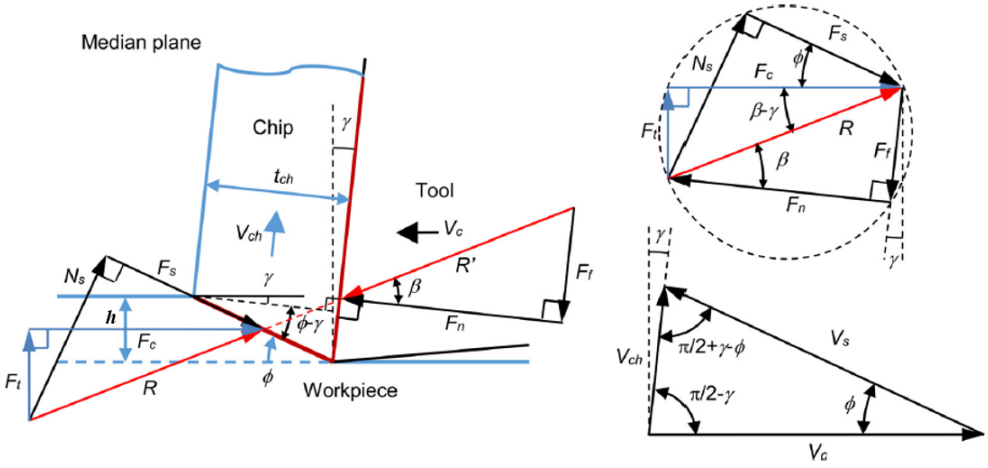

Source: (VEIGA et al., 2021).

For the analysis of the system's mechanics, a physically consistent picture of the nature of the force system associated with the cutting process is essential. A simple approach to the obtaining of such a picture is to treat the chip as a "separate" body in stable mechanical equilibrium under the action of two equal, opposite resultant forces — the force which the tool exerts on the back surface of the chip and the force which the workpiece exerts on the base of the chip (shear plane). The resulting force system for the case of orthogonal cutting is shown in Figure 7, in which R and R' represent the two equal, opposite forces that hold the chip in equilibrium. The force R' which the tool exerts on the chip may be resolved along the tool face into a component F_f, the friction force, which is responsible for the work expended in friction as the chip slides over the tool face and into a component F_n, the normal force, perpendicular to F_f (MERCHANT, 1945).

Figure 8 illustrates these forces involved in orthogonal machining by a Merchant Circle. Besides, the total cutting force R can be resolved into components F_c (cutting force) and F_t (thrust force), which are in directions respectively parallel and normal to the cutting direction. R may also be resolved into the components F_f (friction force) and F_n (normal force) parallel and normal to the tool rake face (LIEW; HUTCHINGS; WILLIAMS, 1998).

Thus, applying the force balance principle to the chip, the resulting forces R and R' must be equal in magnitude and direction, but in the opposite direction. Aiming to obtain the

forces F_s, N_s, F_f and F_n, two force components that can be measured in orthogonal cutting tests as follows:

a) A cutting force component F_c in the direction of cutting speed V_c;
b) And a thrust force component F_t, or named as feed force, perpendicular to the cutting force F_c.

These two force components F_c and F_t can be measured in the orthogonal cutting using a dynamometer. As well as the passive force F_p are usually detected metrologically with the help of piezoelectric force sensors (KLOCKE; KUCHLE, 2011a).

Figure 7 – Force system holds chip in stable mechanical equilibrium in the orthogonal cutting.

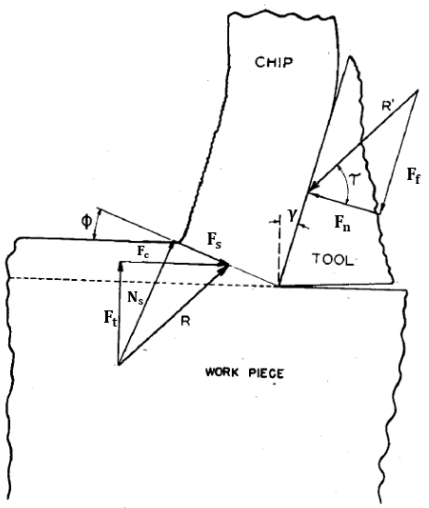

Source: adapted from (MERCHANT, 1945).

Figure 8 – Merchant circle to determine various forces acting in the cutting edge.

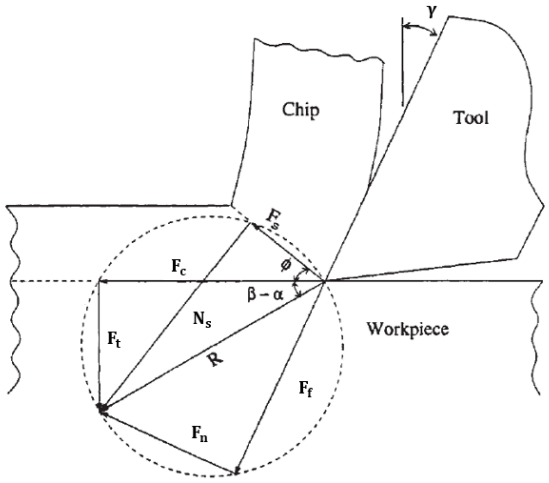

Source: adapted from (LIEW; HUTCHINGS; WILLIAMS, 1998).

Taking into account the force circle diagram (Merchant circle diagram) shown in Figure 8 and also in Figure 6, shear force F_s and normal force N_s can be expressed as a function of cutting force F_c, thrust force F_t and shear angle ϕ (MERCHANT, 1944):

$$F_s = F_c \cdot cos(\phi) - F_t \cdot sin(\phi) \tag{3}$$

$$N_s = F_c \cdot sin(\phi) + F_t \cdot cos(\phi) \tag{4}$$

Similarly, friction force F_f and normal force F_n can be expressed as a function of forces F_c and F_t and tool rake angle γ (MERCHANT, 1944):

$$F_f = F_c \cdot sin(\gamma) + F_t \cdot cos(\gamma) \tag{5}$$

$$F_n = F_c \cdot cos(\gamma) - F_t \cdot sin(\gamma) \tag{6}$$

The heat generation sources can be then estimated using these speeds (V_s and V_s, Equation 1 and Equation 2) and the cutting forces (F_s and F_f, Equation 3 and Equation 5) generated during the orthogonal cutting process (VEIGA et al., 2021). Research has shown that at least 99% of the input energy is converted into heat by deformation of the chip and by the friction of the chip and workpiece on the tool (ONYECHI; OLUWADARE; OBUKA, 2013). The interface at which the chip slides over the tool is normally the hottest region during cutting. The actual temperature is strongly affected by workpiece material, cutting speed, feed, depth of cut, tool geometry, coolant, and many other variables. (ONYECHI; OLUWADARE; OBUKA, 2013)

The illustration in Figure 9 left gives information about the heat that is absorbed/dissipated by the workpiece, chip and tool. Most of the heat is dissipated by the chip. Most of the mechanical energy (in this case 75% and generally more than 50%) is converted in the shear zone. The heat arising in the individual development locations is dissipated by thermal conduction, radiation and convection to the environment. As a result of this heat balance, corresponding temperature fields form in the workpiece and tool that change until equilibrium between added and removed heat is achieved. The right side of the figure shows such a temperature field (KLOCKE; KUCHLE, 2011a).

Thus, the most crucial part of the work generated during the cutting process is converted into heat (ONYECHI; OLUWADARE; OBUKA, 2013). It is well known that two principal heat sources cause a temperature rise in metal cutting — the shear plane (or the shear zone) heat source at the primary shear plane and the frictional heat source at the tool-chip interface (KOMANDURI; HOU, 2001a). Based on this previous modeling of the orthogonal cutting process, the heat sources that emerge in the primary shear zone and the secondary deformation zone can be evaluated. For a sharp cutting tool without flank wear, the heat sources are (VEIGA et al., 2021):

Figure 9 – Distribution of heat and temperature in workpiece, chip, and tool in the process of steel cutting.

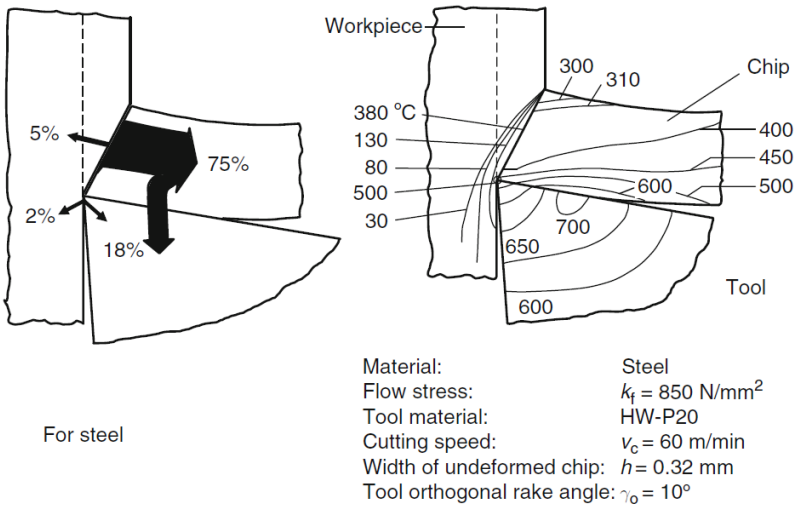

Source: (KLOCKE; KUCHLE, 2011a)

a) The primary heat source, due to plastic deformation in the shear plane: This source affects the temperatures of workpiece and chip and is modeled as an oblique moving heat source with heat flux q_s .The heat flux q_s generated on the shear plane can be expressed as a function of shear force F_s , shear speed V_s and shear plane area ($L_s \cdot w$), where L_s is the length of the shear plane and w is the width of cut (Figure 5):

$$q_s = \frac{F_s \cdot V_s}{L_s \cdot w} \tag{7}$$

b) The secondary heat source, due to friction at the tool-chip interface: This heat source, acting on the tool-chip interface, is assumed to be rectangular with dimensions $L_f \cdot w$, where L_f is the contact length between chip and tool on the rake face. This heat source is modeled as a stationary heat source for the tool and as a moving heat source for the chip. The heat flux q_f generated in the tool-chip interface due to friction can be expressed as a function of friction force F_f, chip speed V_{ch} and secondary heat source area $L_f \cdot w$:

$$q_f = \frac{F_f \cdot V_{ch}}{L_f \cdot w} \tag{8}$$

Using Blok's approach of heat partition (BLOK, 1937), it is considered only a fraction of the total heat generated by the frictional heat source, $B \cdot q$ to flow into the chip and the remaining portion, $(1 - B)q$ to flow into the tool. Whereas heat intensity at the primary shear zone due to shearing can be modeled uniformly. However, Chao (1953) assumed uniform heat intensity with a non-uniform heat partition ratio at the tool-chip interface, i.e., the heat intensity acting on the chip along the tool-chip interface can be expressed as $B(x)q_f(x)$, and that acting

on the tool is $[1 - B(x)]q_f(x)$. Komanduri e Hou (2001a) extended the functional analysis based on the work of Chao (1953). Thus, the secondary heat source cannot be assumed as uniform because of plastic and elastic zones along contact length. Huang e Liang (2003) used the nonuniform heat intensity along the tool-chip interface in their model (KARPAT; ÖZEL, 2006a).

2.1.2 Milling Process

Milling is a machining production method with a circular cutting movement of a usually multi-tooth tool for producing flat and curved surfaces (KLOCKE; KUCHLE, 2011c);(SHAW; COOKSON, 2005). The direction of the cut is perpendicular or sometimes transverse to the tool's axis of rotation. (KLOCKE; KUCHLE, 2011c). Also, milling is a process of removing the excess material from the workpiece in the form of small individual chips. These chips are formed by the intermittent engagement with the workpiece of a plurality of cutting edges or teeth integral with or inserted in a cylindrical body known as the milling cutter (MARTELLOTTI, 1941).

The principal differences between milling and other machining processes are (COMMITTEE et al., 1989):

a) The interruptions in cutting that occurs as the teeth of the milling cutter alternately engage and leave the workpiece;
b) The relatively small size of the chips in milling force;
c) The variation in thickness within each chip;

There are three basic types of milling cutters: plane, face and end milling. In the plane milling (Figure 10a), the cutting edge may be parallel to or inclined to the axis of the cutter. While for the face milling (Figure 10b), the axis of the cutter is perpendicular to the finished surface. An end mill closely resembles a face mill but is a very much smaller cutter.

Figure 10 – Principal types of milling cutters: (a) Plane. (b) Face.

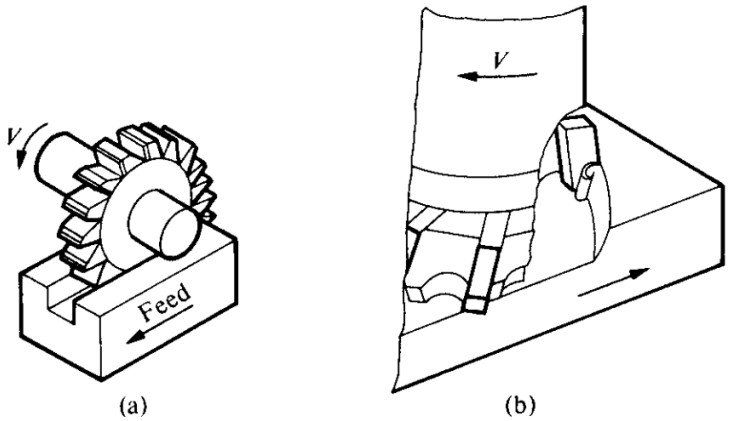

Source: (SHAW; COOKSON, 2005).

If the workpiece surface is produced by the front face of the tool with the minor cutting edge, it is called face milling (Figure 10b and Figure 11). Analogously, milling processes in which the surface is manufactured by the cutting edges on the milling cutter periphery are called peripheral milling Figure 12 (KLOCKE; KUCHLE, 2011c).

Figure 11 – Kinematics of Face Milling.

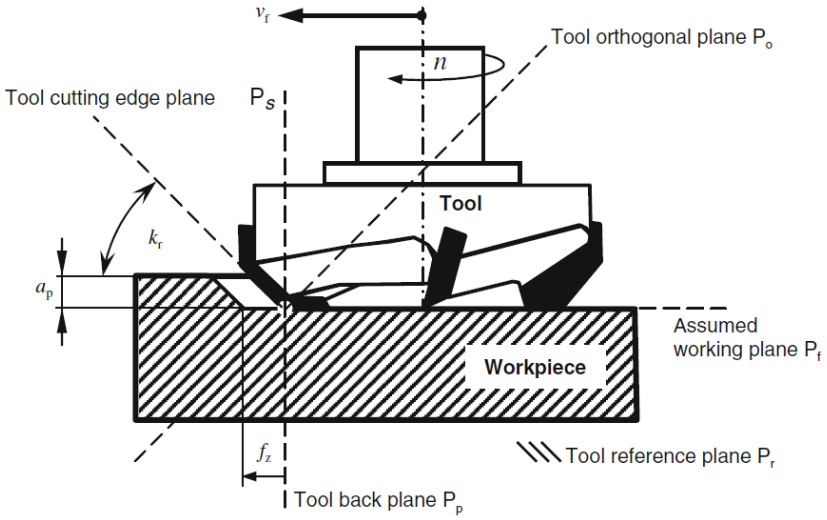

Source: (KLOCKE; KUCHLE, 2011c).

Figure 12 – Kinematics of Peripheral Milling.

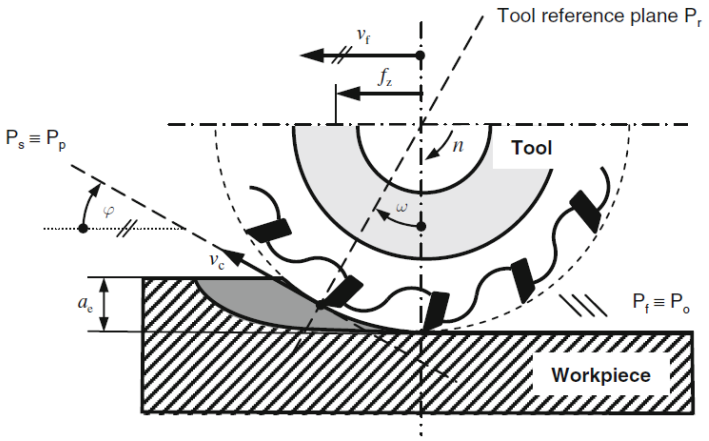

Source: (KLOCKE; KUCHLE, 2011c).

The process can also be distinguished by further implications regarding chip formation and affiliated non-steady-state cyclic conditions of the forces, heat sources, and thus temperatures. Subsequently, the fluctuating heat sources and generated temperature fields lead to cyclic thermal loads of the tool and workpiece with effects on tool wear, surface integrity, and machinability in general (AUGSPURGER et al., 2020; KLOCKE; KUCHLE, 2011c).

Following the kinematics representation in Figure 13 and according to (KLOCKE; KUCHLE, 2011a) for peripheral milling, the active force on the edge F_a is split in the normal cutting force F_{cn} and in the cutting force F_c. Those can be obtained from the cutting force components $F_{x,y}$ regarding the engagement angle Φ by (AUGSPURGER et al., 2020).

Figure 13 – Kinematics of the Peripheral Milling Process.

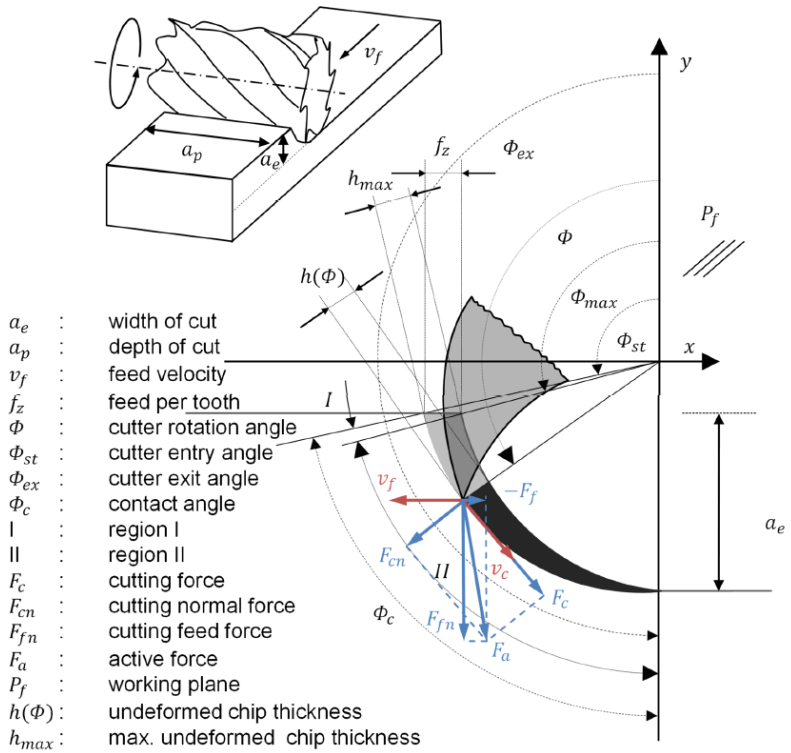

Source: (AUGSPURGER, 2018).

$$\begin{bmatrix} F_c \\ F_{cn} \end{bmatrix} = \begin{bmatrix} sin(\Phi) & -cos(\Phi) & 0 \\ cos(\Phi) & sin(\Phi) & 0 \end{bmatrix} \cdot \begin{bmatrix} F_x \\ F_y \end{bmatrix} \tag{9}$$

2.2 ANALYTICAL MODELS FOR TEMPERATURES IN THE CUTTING PROCESS

As presented before in the Introduction of this work, cutting is a manufacturing process with strongly interconnected thermal and mechanical physics, which are until today a challenge to understand. An accurate analysis of the cutting temperature is a basis for metal cutting issues such as surface integrity, tool life and thermal distortions of machined parts. In literature, analytical and numerical modeling have been presented. Due to limited computational capacity years ago, the first models for temperatures in cutting were analytical.

The following sections will discuss analytical models for predicting temperature in the cutting process. In this Section, it will be presented the theories for temperature in orthogonal cutting. The state of the art regarding analytical models for steady-state temperature in orthogonal cutting is the basis for transient temperature fields in the milling process, i.e., in the interrupted cutting. Thus, the literature is divided into two parts: one regarding steady-state temperature in orthogonal cutting, based on Jeager Solution, and another regarding application to transient

temperature in orthogonal cutting, based on Green's Function. The theoretical fundamentals for the methodology of this work will be discussed in detail: Jaeger solution and Green's Function.

2.2.1 Analytical Steady-State Thermal Models in the Orthogonal Cutting Process

Pioneering work on the analytical modeling of temperatures in the cutting process was conducted by Blok (1937), Jaeger (1942) and Jaeger e Carslaw (1959). The moving heat source method has been widely used by many researchers to study the cutting temperature. This method was proposed by Jaeger (1942), in which analytical modeling of moving heat sources in semi-infinite and infinite solids is taken into consideration. Jeager's work introduced into the study of cutting temperature by Rosenthal (1946) and has been carried out since 1950 in order to predict temperatures at the shear plane (HAHN, 1951; LEONE, 1953), at the tool-chip interface (TRIGGER; CHAO, 1955) and in the cutting tool (LOEWEN, 1954).

Therefore, many of the first analytical models of the cutting process are based on the so-called Jaeger's solution for moving heat sources, which gives a solution of the prevailing differential equations for the steady-state temperature field caused by a moving heat source on a semi-infinite solid. This approach can be used with the aim of calculating temperature fields as the result of the shear plane or rake face heat source in mathematically linked sub-regions of the cutting zone like the tool, the workpiece and the chip region considering adequate boundary conditions, e.g., adiabatic.

The principle of the heat source method is the superposition of the temperature fields for individual heat sources. The basis of the heat source method is the solution for the instantaneous point heat source, Equation 10 (RICHARDSON; KEAVEY; DAILAMI, 2006):

$$\theta_M = \frac{Q_{pt}\alpha}{8k(\pi\alpha t)^{3/2}} e^{-R^2/4\alpha t} \tag{10}$$

Where Q_{pt} is the heat flux at a point (W), α is the thermal diffusivity (m^2/s), θ_M is the temperature rise at point $M(^\circ C)$. This is then integrated along the length of the heat source in the feed direction, x, from $-l_i$ to $+l_i$ to provide the solution for a moving band heat source in an infinite solid and multiplied by two in a semi-infinite solid (RICHARDSON; KEAVEY; DAILAMI, 2006; AUGSPURGER, 2018), Equation 11:

$$T_M = \frac{\dot{q}''}{\pi k} \int_{-l_i}^{+l_i} e^{-\frac{v(X-x)}{2\alpha}} \cdot K_0 \cdot \left[\frac{(v)}{2\alpha} \cdot \sqrt{(X-x)^2 + Z^2} \right] dx \tag{11}$$

The variable K_0 represents the BESSEL function of the second kind, order zero, v the velocity of the moving heat source, x the coordinate parallel to the workpiece's surface, α the temperature diffusivity, k the heat conductivity and X respectively Z the coordinates of the points the temperature T_M is calculated.

The modified Bessel function of the second kind is the function $K_n(x)$ which is one of the solutions to the modified Bessel differential equation. This modified Bessel function of the second kind is sometimes called as the Bessel function, modified Bessel function of the third kind, or Macdonald function.

Thereby, this Equation 11 is Jaeger's classical solution for a moving band heat source in an infinite solid, which can be applied for the workpiece. However, for other applications, a stationary rectangular heat source on a semi-infinite solid can be calculated by $U_{st}(x, y, z; a, b, \lambda_0)$, the increment of the temperature at a point $M(x, y, z)$ of a semi-infinite solid due to a stationary rectangular heat source with dimensions $(2a) \cdot (2b)$ and acting on the solid surface (Figure 14), which can be expressed as Equation 12:

Figure 14 – Stationary rectangular heat source on a semi-infinite solid.

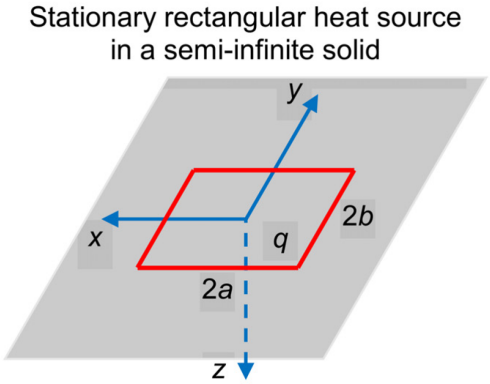

Source: (VEIGA et al., 2021).

$$U_{st}(x, y, z; a, b, \lambda_0) = \frac{1}{2\pi\lambda_0} \int_{-a}^{a} \int_{-b}^{b} \frac{1}{\sqrt{(x - x'^2) + (y - y'^2) + z^2}} dx'dy' \tag{12}$$

Where λ_0 is the thermal conductivity of the solid. In the 2000s, Komanduri and Hou proposed an analytical model that predicts the temperature distribution near the shear zone, both in the chip and the workpiece, incorporating a modification to this Jaeger's stationary rectangular heat source solution considering the effect of additional boundary, that is, appropriate image sources (KOMANDURI; HOU, 2000; KOMANDURI; HOU, 2001a; KOMANDURI; HOU, 2001b). An image heat source is a mirror image of the heat source regarding the boundary surface with the same heat liberation intensity. Komanduri and Hou used non-uniform heat partition distribution between tool and chip to account appropriate boundaries using the functional analysis approach, originally proposed by (TRIGGER, 1951).

As already mentioned in Section 2.1.1, Huang e Liang (2005) investigated a model that considered nonuniform heat intensity along the tool-chip interface. Also, they developed a model for predicting temperature along the tool-workpiece interface of a worn tool (HUANG; LIANG, 2003). Chou e Song (2005) used an analytical approach to develop a thermal model for

temperature predictions in finish hard turning, in particular, the machined-surface temperature that can be used for part thermal damage evaluation, and validated their models based on white layers generated on the workpiece surface. Karpat and Özel presented a model for cutting and ploughing forces and temperatures that included the effect of flank wear (KARPAT; ÖZEL, 2006a; KARPAT; ÖZEL, 2006b), subsequently developed a thermal model to predict the temperature in chamfered tools (KARPAT; ÖZEL, 2008).

Also based on Komanduri e Hou (2001b)'s thermal model, M'Saoubi e Chandrasekaran (2011) analyzed tool temperature distribution by taking a non-uniform heat produced along with the tool-chip interface into consideration and investigated the effect of workpiece material treatment on tool temperature.

Later, Deppermann e Kneer (2015) measured the temperatures of the workpiece during an orthogonal turning process of carbon steel (AISI 1045). An analogous thermal model was used to solve the ill-posed inverse heat conduction problem by the sequential estimation method, introduced by (BECK; BLACKWELL; JR, 1985). Still in 2015, Gierlings adapted and validated Komanduri e Hou (2001b)'s analytical temperature model to the broaching process on super alloy Inconel 718 intending to confirm the connection between cutting zone temperatures and thermal induced surface integrity defects. Furthermore, the model was extended by a tool-workpiece contact heat source, considering the different tool wear states until the end of the tool lifetime. Finally, he used the adapted model for a process monitoring solution (GIERLINGS, 2015).

Hu et al. developed an analytical thermo-mechanical model of orthogonal cutting using tools with a negative rake face and chamfered tools (HU et al., 2019a; HU et al., 2020). Based on slip-line field theory, material plasticity, and ploughing theory, the modeling allows for the estimation of slip-line field geometry, cutting forces, and cutting temperature distribution. Then, Hu et al. (2019b) developed a modified heat partition model to estimate the heat partition ratio on the tool-chip interface based on the expressions for non-uniform heat partition ratio defined by Komanduri e Hou (2001a). Besides, in Zhao e Liu (2019), the transient partition ratio at the tool-chip interface of coated tools in continuous and interrupted cutting was modeled considering the coating thickness and thermal properties in the modeling.

In Chenwei et al. (2019), an improved analytical model based on the moving heat source method is developed for predicting the distribution of the cutting temperature in orthogonal cutting of titanium alloy Ti6Al4V. Also in 2019, Mirkoohi, Bocchini e Liang (2019) developed an iterative nonlinear regression model to predict the cutting conditions for a required cutting temperature. In Ning e Liang (2019a), the analytical thermal models proposed in the literature by Oxley (1989) — which is a monograph that presents a very thorough continuum mechanics approach to steady-state metal cutting where the chips produced are in the form of continuous ribbons — Komanduri e Hou (2001b), Ning e Liang (2018) and Ning e Liang (2019b) were compared in terms of prediction accuracy, computational efficiency and experimental complexity.

Wang et al. (2020) has recently used analytical modeling to predict the steady temperature generated in cryogenic machining. The model considers the heat losses due to

cryogenic cooling employing a convective heat transfer coefficient in the rake and flank faces of the tool. The influences of some important factors, including the shear deformation at the primary zone, the friction at the tool-chip interface, and the heat losses at both rake and flank faces of the tool caused by liquid nitrogen jetting, were all considered in the thermal model.

For last, Veiga et al. (2021) presented a new methodology that considers the temperature-dependent thermal conductivity of materials for estimating the heat partition ratio along with the secondary heat source, which is assumed to be non-uniform.

2.2.2 Analytical Transient Thermal Models in Interrupted Cutting

It has long been realized that thermal conditions in interrupted cutting processes such as milling differ from those in continuous processes such as turning. In interrupted processes tools are subjected to cyclic heating and cooling as they pass in and out of the workpiece, and may fail by thermal fatigue mechanisms not encountered in the continuous case (STEPHENSON; ALI, 1992). Recently, analytical models for temperature prediction in other cutting processes such as milling have also been developed in literature (VEIGA et al., 2021). Already Jaeger e Carslaw (1959) suggested the possibility to use Green's functions in order to solve inhomogeneous, transient heat conduction problems for the application in one-, two- and three-dimensional space with heat generation.

Green's functions are named after the British mathematician George Green, who first developed the concept in the 1820s (CANNELL, 1999). Under the many-body theory, the term is also used in physics, specifically in quantum field theory, aerodynamics, aeroacoustics, electrodynamics, seismology and statistical field theory, to refer to various types of correlation functions (BONCH-BRUEVICH; TYABLIKOV, 1962). Furthermore, Green's Functions (GFs) have been used in the solution of heat conduction for many decades, for example in the classic books by Morse e Feshbach (1954) and Jaeger e Carslaw (1959). Also, Ozisik (1993) presented a fine derivation of the GF solution equation. Cole et al. (2010) provided a book containing the following components: a careful derivation of the GF solution equation; a systematic and practical approach to the solution of diffusive-type problems; and, an extensive compilation of GFs.

One advantage of GFs is that they are flexible and powerful. The same GF for a given geometry and a given set of homogeneous boundary conditions is a building block for the temperature distribution resulting from (a) space-variable initial temperature distribution, (b) time- and space-variable boundary conditions, and (c) time- and space-variable volume energy generation (COLE et al., 2010).

The Green's function $G(r, t \mid r', \tau)$ represents the temperature at the location r, at time t, due to an instantaneous point source of unit strength, located at the point r', releasing its energy spontaneously at time $t = \tau$. Based on this definition, the physical significance of Green's function may be interpreted as follows (AUGSPURGER, 2018):

$$G(r,t \mid r',\tau) = G(effect \mid impulse) \tag{13}$$

The first part of the argument, "r,t", represents the "effect", the temperature in the medium at the location r at time t, while the second part, "r',τ", represents the impulse, the impulsive instantaneous point source located at r'. It releases its heat spontaneously at time τ. The usefulness of Green's function lies in the fact that the solution of the original problem can be represented in terms of Green's function. Therefore, once the Green's function is known, the temperature distribution $T(r,t)$ in the medium may be determined (AUGSPURGER, 2018).

For the application of Green's Function to the cutting process, Chakraverti, Pandey e Mehta (1984) presented a unidimensional model for temperature distribution in the tool during intermittent cutting. Years later, Stephenson e Ali (1992) picked up the approach in order to model the temperature in a semi-infinite rectangular corner , $x \geqslant 0$, $y \geqslant 0$, and $z \geqslant 0$, heated by a time-varying heat flux (as shown Figure 15) with various spatial distributions and to investigate the general nature of the temperature distribution within the tool assuming adiabatic conditions at the boundaries. More details of this geometry assumption can be noticed in Figure 16.

Figure 15 – Tool insert model in the milling process.

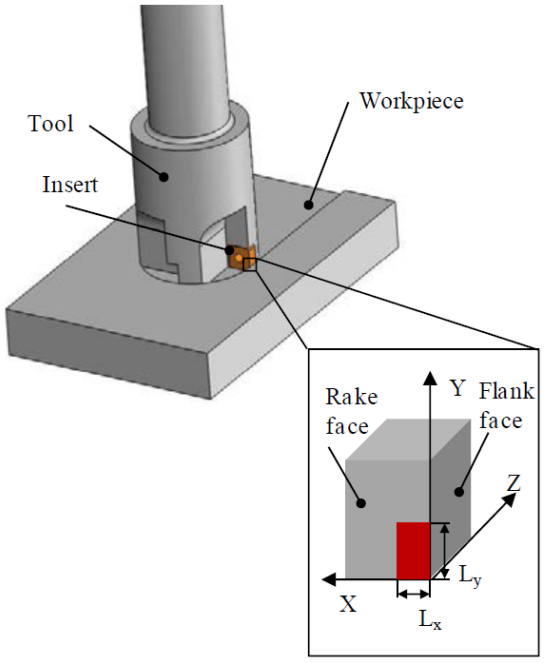

Source: (KARAGUZEL; BAKKAL; BUDAK, 2016).

A semi-infinite body is described by a body occupying the region $x \geq 0$. Although it represents an idealized body extending to positive infinity, it is a good model for many problems. A finite body of thickness L can be represented by a semi-infinite body, $0 < x < \infty$, when the boundary condition at $x = L$ does not influence the temperature distributions near $x = 0$. This happens for the small dimensionless times of $\alpha t/L^2 < 0,05$. Isothermal and insulation boundary

conditions at $x = 0$ can be constructed from the infinite region solutions (COLE et al., 2010).

Figure 16 – Approximation of the cutting tool by a semi-infinite corner. The secondary heat source in orthogonal cutting is the x, y-plane (the rake face).

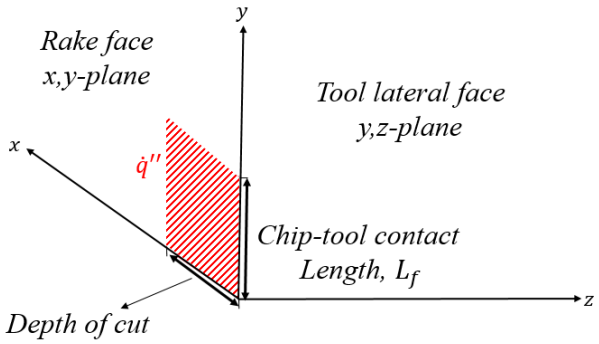

Source: adapted from (AUGSPURGER, 2018).

According to Stephenson e Ali (1992), the Green's function for the temperatures in a semi-infinite corner due to an instantaneous point source at time τ at the surface point $x = x_p$, $y = y_p$, $z = 0$, assuming adiabatic conditions at the boundaries, can be obtained by multiplying the Green's function for three mutually perpendicular instantaneous plane sources in semi-infinite half spaces which intersect to form an eighth space or corner as shown in Figure 16. The x, y-plane represents the tool's rake face, where the planar heat source, extending over chip-tool contact length Ly and the depth of cut Lz, is applied. The clearance face is represented by the x, z-plane and the tool's lateral face by the y, z-plane. Thus, the temperature field $T(x, y, z, t)$ at a point x, y, z in the corner at the time t can be calculated by a solution of:

$$\begin{gathered} \frac{\partial^2 T}{\partial x^2}+\frac{\partial^2 T}{\partial y^2}+\frac{\partial^2 T}{\partial z^2}=\frac{1}{\alpha}\frac{\partial T}{\partial t} \\ -\lambda \cdot \frac{\partial T}{\partial z}=\dot{q}''(x,y,t);\ 0 \leqslant y \leqslant L_y;\ 0 \leqslant x \leqslant L_x;\ z=0 \end{gathered} \tag{14}$$

$$T(x,y,z,t)=\frac{\alpha}{\lambda}\int_0^t\int_0^{L_x}\int_0^{L_y} G(x,y,z,t,x_p,y_p,0,D)\cdot\dot{q}''(x_p,y_p,\tau)dx_p dy_p d\tau \tag{15}$$

For D determined by Equation 16, $G(x, y, z, t \mid y', z', 0, D)$ can be defined as Equation 17, which is the Green's Function of the semi-infinite corner. Physically D is the scaling factor or characteristic dimension for the penetration of the temperature field at time t due to an instantaneous heat source at the time τ (AUGSPURGER, 2018).

$$D=\sqrt{4\alpha(t-\tau)} \tag{16}$$

$$
\begin{aligned}
G(x,y,z,t\,|\,x',y',z',D) = \\
&= \frac{1}{(\sqrt{\pi}D)^3}\left\{exp\left[-\frac{z^2}{D^2}\right]\right\} \\
&\cdot\left\{exp\left[-\frac{(y-y')^2}{D^2}\right]+exp\left[-\frac{(y+y')^2}{D^2}\right]\right\} \\
&\cdot\left\{exp\left[-\frac{(x-x')^2}{D^2}\right]+exp\left[-\frac{(x+x')^2}{D^2}\right]\right\}; \\
&t-\tau \geq 0
\end{aligned}
\tag{17}
$$

Using the error function, $erf()$, that is defined by Equation 18 (COLE et al., 2010), for a spatial uniform heat source the temperature field an instantaneous heat impulse over the patch $0 \leq x \leq L_x$ and $0 \leq y \leq L_y$, the Equation 26 can be defined as Equation 19.

$$
erf(x) = \frac{2}{\sqrt{\pi}}\int_0^x e^{-t^2}dt \tag{18}
$$

$$
\begin{aligned}
T(x,y,z,L_y,L_z,D) = \frac{a}{\lambda}\int_0^t \frac{1}{2\sqrt{\pi}D}\left\{exp\left[-\frac{(z)^2}{D^2}\right]\right\} \\
\cdot\,\Theta_{GU}(y,L_y,D)\cdot\Theta_{GU}(x,L_x,D)\cdot\dot{q}''(x_p,y_p,\tau)\,d\tau
\end{aligned}
\tag{19}
$$

This Equation is presented at (AUGSPURGER, 2018) for thermal analysis and its simulation is used for comparing the model developed during this work. Where,

$$
\Theta_{GU}(u,L,D) = erf\left(\frac{L+u}{D}\right)+erf\left(\frac{L-u}{D}\right) \tag{20}
$$

Besides the application of Green's Function, the transient behavior has been solved via assuming quasi-steady-state conditions to determine heat partition and heat flux towards tool (ISLAM, 2018). Richardson, Keavey e Dailami (2006) introduced an analytical model for the temperature fields in the workpiece by a modified Jaeger's solution for the flat moving heat source in the semi-infinite solid. It was simulated the peripheral milling process by using a method of moving heat sources, and the heat flux value for the workpiece was determined via the temperature measurements from the workpiece.

Using a point heat source Green's function solution, Sato, Tamura e Tanaka (2011) extended Stephenson e Ali (1992) approach to end milling temperature modeling. They considered the changing chip load and contact length via introducing time-dependent plane heat sources. However, heat flux and heat partition were approximated based on the assumptions in (STEPHENSON; ALI, 1992).

In 2013, Jiang et al. (2013) modeled induced temperature of both tool and workpiece during interrupted cutting. An inverse heat-conduction method is proposed to calculate temperature distribution and heat flux flowing into the tool and workpiece based on the measured

temperature data in the interrupted cutting processes. Besides that, Lin et al. (2013) investigated the transient temperature variation in the workpiece for an end milling process considering the flank rubbing effect as a result of tool wear. Moving heat sources according to the Jaeger's solution were considered in order to model a flank wear-land heat source and a shear plane heat source, which induce heat into the workpiece. Subsequently, Liu et al. (2014) modeled workpiece temperature in helical end milling by introducing heat sources along the flank and bottom cutting edges. A nonhomogeneous partial differential equation (PDE) containing heat source term was derived and was solved using Green's function approach.

Using these models, the effects of microstructure evolution when milling Inconel 718 (FENG; PAN; LIANG, 2018) and of laser preheating in laser-assisted milling of Ti6Al4V (FENG et al., 2019) on cutting temperatures were studied. A transient heat conduction model for the prediction of the cutting tool temperature generated in end milling operations was developed by Karaguzel e Budak (2018). They discussed proposed a dual-zone model to calculate the heat flux at the too-chip interface and the Green functions to determine the temperature distribution in the cutting tool.

Augspurger (2018) analyzed the temperatures and heat flows in the milling process aiming to understand causal and statistical relationships between process parameters and thermal state variables. These have a direct influence on tool wear in the process, dimensional accuracy and surface integrity. In 2020, Augspurger et al. (2020) showed the results of a model extended measuring approach in order to monitor as well as investigate heat flows and their partitioning in the milling process under dry conditions.

Besides the literature that has used semi-infinite Green's Function for the interrupted cutting process, Green's Function can be applied for other geometry assumptions. Fernandes et al. (2010), with the aim of using a 3D-transient analytical solution based on Green's function to reduce computational time in inverse heat conduction problems, used a method of a rectangular parallelepiped geometry.

2.3 MEASUREMENT OF THE TEMPERATURES IN CUTTING PROCESS

It is obvious that temperature prediction is very important and is one of the most complex subjects in the metal cutting literature. Apart from the prediction, temperature measurement is an even more challenging part of this research area because it is very difficult to make temperature measurement very close to the cutting edge, and due to this fact there is a lack of experimental data verifying the proposed mathematical models in the literature (DINC; LAZOGLU; SERPENGUZEL, 2008).

Cutting temperatures are more difficult to measure accurately than cutting forces. The cutting force is a vector completely characterized by three components, while the temperature is a scalar field, which varies throughout the system and which cannot be uniquely described

by values at a few points. For this reason, no simple analog to the cutting force dynamometer exists for measuring cutting temperatures; rather, several measurement techniques based on various physical principles have been developed. Particular methods generally yield only limited information on the complete temperature distribution (STEPHENSON; AGAPIOU, 2018).

Numerous attempts have been made to measure the temperature in the machining operations (DINC; LAZOGLU; SERPENGUZEL, 2008), which vary according to technique, experimental setup and measurement position. The measurement of temperature in material removal processes has an extremely long history which we have summarized in Figure 17, where it tabulates the introduction of important work in the field by method. The only metrological techniques that come into question for measuring temperature during the cutting process are time-resolution measurement techniques, since the cutting process duration (and thus the achievement of a thermally stationary state) is too short for other methods. Of the processes, temperature measurement with thermocouples, pyrometers and photo thermometry are of technical interest (KLOCKE; KUCHLE, 2011a) as shown in Figure 18.

Figure 17 – Historical outline of thermal measurements in material removal processes.

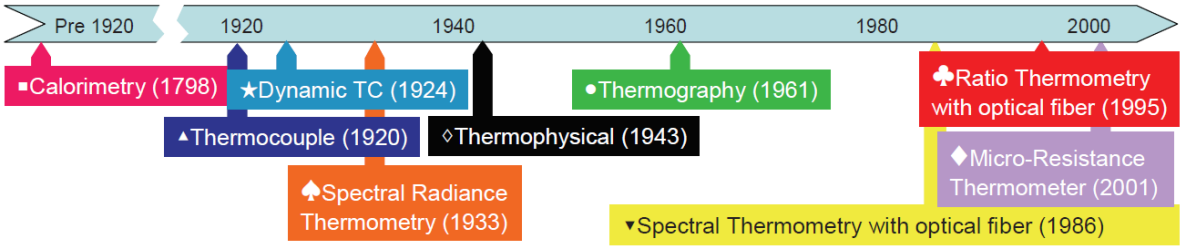

Source: (DAVIES et al., 2007).

Figure 18 – Technical interest in thermal measurements for material removal processes.

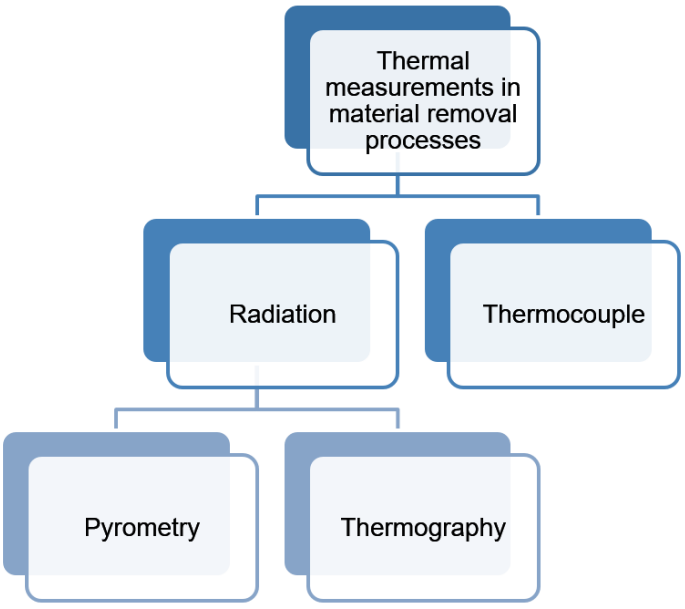

Source: Author.

2.3.1 Thermocouple Method

The tool–work thermocouple method (Figure 19), first developed in the 1920s by Verbeek (1920) as shown in Figure 17, uses the tool and workpiece as the elements of a thermocouple (STEPHENSON; AGAPIOU, 2018). The thermocouple (TC) is the most widely used temperature sensor, which consists of two dissimilar metals that produce a voltage in the vicinity of the point where the two metals are in contact. The voltage produced is dependent on the difference of temperature of the junction to other parts of those conductors Nee (2015).

Figure 19 – Tool-workpiece thermocouple arrangement.

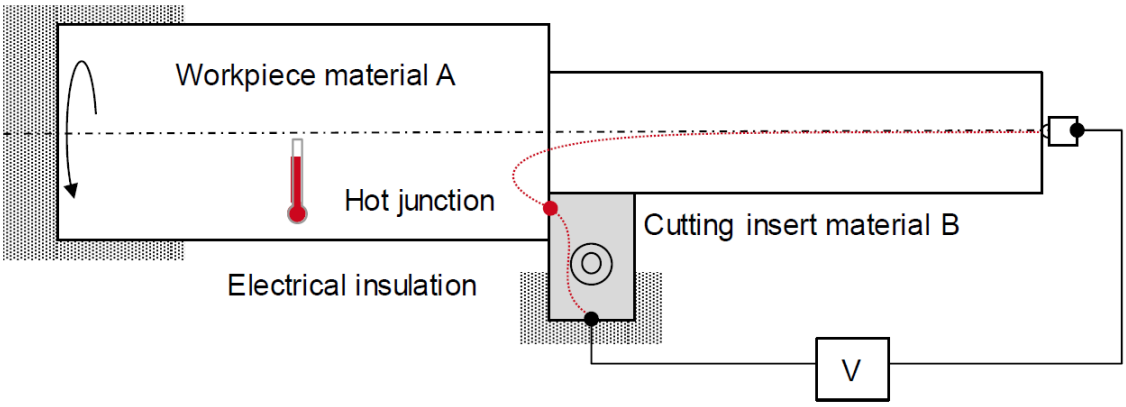

Source: (AUGSPURGER, 2018).

This method can only be used when both the tool and workpiece are electrical conductors, and thus cannot be used with many ceramic cutting tools. The thermoelectric power of the circuit is usually low and must be estimated by calibrating the circuit against a reference thermocouple (STEPHENSON; AGAPIOU, 2018).

Installing a thermocouple into the tool or workpiece allows for a point-wise determination of the temperature. Thermocouples can be applied in blind holes in the tool or the workpiece. Temporal resolution is influenced by the response time of the thermocouple and heat transfer between the thermocouple and the device under test. These techniques generally have low temporal resolution (KLOCKE; KUCHLE, 2011a). However, it is characterized by the main advantages of low cost, simple construction, ease of remote measurement, flexibility in construction, simplicity in operation, a broad temperature range (-300$°C$ to 1200$°C$) and low inherent uncertainties (< 1$°C$). Yet, for the application in the metal cutting process, besides method specific errors, it suffers from signal lag and settling errors, uncertainties regarding the thermal resistance at the sensor contact in the immersion and the alteration of the temperature field by the sensor. Further difficulties are the structural weakening by the required immersion, thus restricted accessibility (except thin film solutions) and the incapability to resolve high temperature gradients by the principle (AUGSPURGER, 2018).

Stephenson (1993) considered several issues associated with the implementation of the chip–tool thermocouple technique. He points out it is necessary to isolate only the tool, since a potential difference is measured and the machine is usually well-grounded. Removing the

necessity of insulating the work eliminates the possibility of reducing the stiffness of the system (SHAW; COOKSON, 2005).

It may be pointed out that extensive experimental work on tool-work interface temperatures in machining steel with cemented tungsten carbide using a chip-tool thermocouple technique at various cutting conditions by Trigger (1948), Trigger (1949) and Komanduri (1993). In 1963, Administration, Group e Boothroyd (1963), with the probe thermocouple investigated the temperature distribution over the top and side surfaces of the tool close to the chip in the orthogonal metal cutting process.

In the 1990s, Stephenson, as it was already discussed, developed an analytical model using Green's functions to calculate the tool temperatures during interrupted cutting. In order to validate their model, they performed a series of experiments and measured cutting temperature by tool-workpiece thermocouple technique (STEPHENSON; ALI, 1992). They concluded that the temperatures in interrupted cutting are lower than those obtained in continuous cutting. Radulescu e Kapoor (1994) also performed measurements using a tool-chip thermocouple method to compare to an analytical model for prediction of tool temperature fields during continuous and interrupted cutting.

Komanduri e Hou (2001b) distinguished between embedded thermocouples, tool-workpiece (dynamic) thermocouples (two bodies in motion as the two elements of the thermocouple), thin-film thermocouples (constituted by vapor deposited coatings) and traverse thermocouples (modification of the tool-workpiece thermocouple) (AUGSPURGER, 2018).

In the work carried out by Lima, Machado e Guimaraes (2001) and Chen, Tsao e Liang (1997), the numerical technique used is the finite volume method and the temperatures are obtained by inserting a thermocouple in the tool. Carvalho et al. (2006) also used the finite volume method to study the temperature fields generated in the cutting processes. The temperatures were measured on accessible locations of the insert, the shim and the tool holder by using thermocouple.

Karpat e Özel (2006a) presented a novel experimental technique to measure transient tool temperatures in dry milling operation with a K-type thermocouple. Richardson, Keavey e Dailami (2006) developed a model to determine the magnitude and distribution of workpiece temperatures for dry milling of aerospace aluminum alloys. The transient temperature profiles predicted by the model were compared with the temperature profiles obtained from the high response speed thermocouple experiments.

In 2013, thermocouples were used to measure the transient temperatures by Onyechi, Oluwadare e Obuka (2013) to compare a three-dimensional steady heat transfer finite element model. A multichannel acquisition system of contact measurement by using thermocouples is developed by Jiang et al. (2013) to accomplish continuous measurement of cutting induced temperature. Also, Lin et al., for the transient workpiece temperature profiles due to the tool getting close to and far away from measuring positions were measured by fast response thermocouples. The thermocouples are K-type thermocouples and two thermal couple wires are

encapsulated in each one (LIN et al., 2013).

Liu et al. (2014) with the purpose of predicting the heat transfer process in helical milling and to gain the accurate measurement temperature, the type K thermocouples were used in the experiments. Still for the milling process, a single wire thermocouple was employed to measure the tool temperature in the conducted milling experiments by Baohai et al. for a developed cutting tool temperature prediction method using an analytical model for end milling (BAOHAI et al., 2016). Recently, other works also used thermocouple method to compared against the prediction results, as Islam (2018), Xiong et al. (2018), Ribeiro et al. (2018), Karaguzel e Budak (2018), Mirkoohi, Bocchini e Liang (2019), Chenwei et al. (2019), Wang et al. (2020), Zhou (2020) and Chenwei et al. (2020).

2.3.2 Pyrometry

Besides thermocouples, radiation is another technique to measure temperature (Figure 18). The most important techniques in this type of measurement, which determines temperature by measuring the heat radiation emitted from a surface, are pyrometry and thermography. Pyrometry, a.k.a. spectral radiance thermometers, is the contact-free determination of absolute temperature by measuring the inherent radiation of a body without spatial scanning of the object field. Thermography will be explained in Section 2.3.3. Radiation techniques have decisive advantages compared with thermoelectric methods: the time resolution is much higher (whereby pyrometers are principally faster than infrared cameras), and they are also contact-free (KLOCKE; KUCHLE, 2011a).

A radiation thermometer/pyrometer uses an optical system to collect the energy emitted by the target, followed by a detector that converts this energy to an electrical signal. An emissivity adjustment is used to match the thermometer calibration to the specific emitting characteristics of the target and an ambient temperature compensation circuit, to ensure that temperature variations inside the thermometer due to ambient conditions do not affect accuracy (NEE, 2015).

One significant problem when measuring for an exact absolute temperature with a radiation method is the dependence of the radiation emitted on the grade of emission of the surface. Since the emission grade is the function of many factors like temperature, wavelength, angular position, material and surface condition, calibrating the measurement device for a particular surface is very difficult. The precision of total radiation and broadband partial radiation pyrometers are especially influenced by factors that alter the spectral grade of emission of the surface. In cutting, effects such as surface roughness and oxidation influence the grade of emission of different surfaces greatly. To limit the influence of the grade of emission on measured temperatures, narrow-band partial radiation, two-color and multi-color pyrometers have been developed (KLOCKE; KUCHLE, 2011a).

The two-color pyrometer (Figure 20) has the advantage that the spectral grades of emission ε_1 and ε_2 of the surface need not be known. Since the two selected wavelengths lie

directly next to each other, $\varepsilon\lambda_1 \sim \varepsilon\lambda_2$. A measurement error will only result if both wavelengths λ_1 and λ_2 differ greatly. Further advantages of this principle are that the measured temperature is independent of signal dampening, due to dust for example, so long as both signals are dampened equally. Moreover, the temperature of objects that are smaller than the optical field of vision can be measured without error (KLOCKE; KUCHLE, 2011a).

Figure 20 – Two-color pyrometer principle.

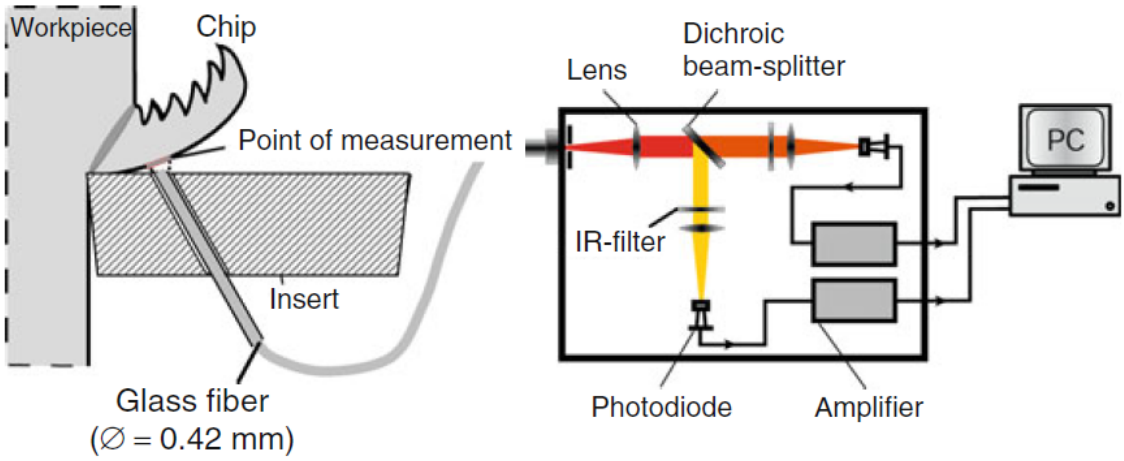

Characteristics

- Measurement of two discrete wavelength bands $\lambda_1 = 1.7$ µm, and $\lambda_2 = 2$ µm which are set into ratio
- High temporal resolution (approx. 2 µs)
- Independence from grade of emission (no calibration required)
- Large range of temperature measurement (250–1200 °C)
- Contact free measurement

Source: (KLOCKE; KUCHLE, 2011a).

Spectral band radiance measurements of material removal processes dates to Schwerd (1933) (as shown in Figure 17) and Kraemer (1937) who focused light from a cutting process directly onto a thermocouple (DAVIES et al., 2007).

As a radiation method, Ueda et al. (2001) measured a flank face temperature in high-speed end milling by a two-color pyrometer with an optical fiber. The effects of cutting speed, feed rate, and depth of cut on the temperature were investigated. Abukhshim, Mativenga e Sheikh (2005) did cutting tests on ASIS 4140 steel with uncoated carbide tools and measured temperature values by using a pyrometer.

Sato, Tamura e Tanaka (2011) used the Green's function model in order to predict punctual temperatures in the milling tool, which they validated by a tool integrated ratio pyrometer in a distance from 0.1 to 0.5 mm to the rake face. In the work of Feng et al. (2019), the surface temperature of the workpiece was measured through an infrared pyrometer. The pyrometer measured the temperature at about 0.2 mm below the machined surface corresponding to the laser beam spot. The measurement range for the pyrometer was between 800 and 2500$^{\circ}C$ and for the infrared thermal camera was up to 2000$^{\circ}C$.

Augspurger et al. (2020) presented a model extended measuring approach in order to

monitor as well as investigate heat flows and their partitioning in the milling process under dry conditions. Therefore, the cutting power in the process was measured through a dynamometer as well as the temperature in the tool by an embedded thermocouple and a ratio pyrometer. As the milling process is complex, the measured temperature is only the average value in a small zone when considering the size effect.

2.3.3 Thermography

While pyrometry is the contact-free determination of the absolute temperature of one point of the object. Thermography provides a pictorial representation of temperature distribution. Thus, infrared cameras can be used as an alternative to pyrometrical measurements. Thermo cameras allow for non-contact, extensive measurement of temperature. They function according to the principle of thermography (KLOCKE; KUCHLE, 2011b). The advantage to this is the pictorial representation of temperature information. Commercial cameras usually work with long wavelengths and large broad-bands, which makes it possible to measure lower temperatures but which also has a negative effect on the attainable accuracy. Scanning cameras that work with a single detector are too slow for fast processes. Some high-speed infrared cameras offer integration times in the range of microseconds, making it possible to capture fast processes without motion blur (KLOCKE; KUCHLE, 2011a).

Boothroyd (1961), Salmon, McCulloch e Rice (1968) and Mayer (1966) developed the first thermal images of the tool-chip interface using infrared (IR) sensitive film. Jeelani (1981) and Lauscher (1989) improved on earlier IR photographic techniques by taking advantage of the development of more sensitive films and more accurate calibration techniques to measure the temperature distribution orthogonal machining.

In the experimental measurements obtained from Dinc, Lazoglu e Serpenguzel (2008), a high precision thermal infrared camera was employed to estimate the cutting temperature during the dry turning process of AISI 1050 with carbide inserts in their work. Yan et al. (2014) also used an infrared camera to measure the cutting temperature distribution. the objective was the modeling and the analysis of coated tool temperature variation in dry milling of Inconel 718 turbine blade considering flank wear effect. The instrument was Type HY-2688, which can automatically measure and capture the maximum temperature in the full screen with the temperature range of 0–800$^{\circ}C$. Temperature resolution is 0.07$^{\circ}C$ at the external temperature of 20$^{\circ}C$.

In Deppermann e Kneer (2015), high-speed infrared (IR) camera was fixed perpendicular to the workpiece's front surface, providing a temporal resolution of 1250 Hz and a temperature resolution of 25 mK at 25$^{\circ}C$. Feng, Pan e Liang (2018) applied a Maurer model QKTR 1075 two-color optical pyrometer and an infrared thermal camera of ThermoVision® model A40 to measure the surface temperature at the laser spot. The measurement range for the pyrometer is between 800 and 2500$^{\circ}C$ and for the infrared thermal camera is up to 2000$^{\circ}C$.

Aiming to verify model predictions by comparing them to tool temperature distributions, Veiga et al. (2021) performed orthogonal cutting tests and used an IR camera. In Hu et al. (2020), inserts with various edge preparations were carried out on a CNC lathe. Predicted chip-tool interface temperature distributions were compared against the measurements from the dynamometer and infrared camera, respectively.

2.4 STATE OF THE ART'S SUMMARY

During a cutting process, the mechanical energy from the plastic deformation developed at the primary shear plane and the chip–tool interface is converted into heat. This heat conducted into the tool is enough to create high temperatures near the cutting edge. As a result, various serious problems such as thermal stress distribution, surface burning, work hardening and tool wear can be caused (ONYECHI; OLUWADARE; OBUKA, 2013). Because of this, it is important to understand or predict the temperature during the cutting processes.

Firstly, in the State of the Art of this work, some essential theoretical fundamentals were presented. It was introduced the machining mechanism, with a focus on the orthogonal cutting and milling process. An orthogonal cutting occurs when the cutting tool is moved relatively perpendicular to a workpiece with a cutting speed V_c. The cutting edge is positioned at a depth below the workpiece surface to remove a layer of the workpiece. The depth of cut corresponds to the uncut chip thickness h. However, milling is a more complex process than orthogonal cutting. Milling is a machining production method with a circular cutting movement of a usually multi-tooth tool. Moreover, the undeformed chip thickness for milling is a function of the cutter rotation angle. As an interrupted process, during the milling process, the tools are subjected to cyclic heating and cooling as they pass in and out of the workpiece. These transient temperature changes may cause cycling strains and alterations of the microstructure and thus material properties in the tool as well as the workpiece.

An accurate analysis of the cutting temperature is a basis for metal cutting issues. With this motivation, the literature has been presented analytical and numerical models. Compared with numerical simulation methods, analytical models have the advantage of being able to provide a clear description of the cutting mechanism and require less computational time.

For orthogonal process, as a continuous process, analytical models of temperatures have been developed for steady-state. Pioneering work was conducted for this purpose especially by Jaeger (1942), who proposed the moving heat source method. Jaeger's classical solution for a moving band heat source in an infinite solid, which can be applied for the workpiece. However, for other applications, as an example for the tool, Komanduri e Hou (2001a) considered the theory of stationary heat sources in semi-infinite solid considering the effect of additional boundary.

Nevertheless, interrupted cutting processes such as milling differ from those in continuous processes. In interrupted processes, tools are subjected to cyclic heating and cooling, that is, to a transient state. For this cutting process, Green's Functions have been used, in which

a tool geometry is considered a semi-infinite rectangular corner.

Another methodology regarding temperature analysis during the cutting process is the measurement. The literature shows that this method might be an even more challenging part of this research area, because it is very difficult to make temperature measurements very close to the cutting edge. The main types of measurement are thermocouple, pyrometer and thermometry. The first was developed in the 1920s, which consists of two dissimilar metals that produce a voltage, dependent on the difference of temperature, at the point where the two metals are in contact. The second, pyrometer, is the contact-free determination of absolute temperature by measuring the radiation of a body without spatial scanning of the object field. While thermography provides a pictorial representation of temperature distribution.

Therefore, all of the analytical models in the literature consider the boundaries as an infinite or semi-infinite assumption. Furthermore, for continuous processes, the solution is obtained for steady-state. However, not all processes of this kind will reach a stationary condition. Furthermore, the solutions for the transient state, i.e., that utilizes Green's Function, are suitable only for a tool as a semi-infinite rectangular corner, with the heat source in the edge. With this motivation, a study of a new analytical model to obtain the transient temperature distribution in the tool will be conducted in this work. It will be defined the tool as finite boundaries and the heat in the chip-tool contact interface as not only defined in the corner. In order to validate the analytical model developed in this bachelor thesis to calculate the tool temperature distribution, orthogonal cutting experiments will be conducted with thermography measurements.

3 METHODOLOGY

In this chapter, the methodology for modeling and implementing an analytical model of the temperature at cutting process is presented, and, subsequently, the experimental test's materials and method are discussed with the purpose of comparing, afterward, the results in Chapter 4.

The procedure for establishing the analytical thermal model in the cutting process will be presented firstly at steady-state: an image method to the tool temperature distribution. Subsequently, the thermal model in the interrupted cutting process will be presented at transient state for the tool's temperature field using Green's Function: with semi-infinite boundaries assumption from the previews literature and with finite geometry assumption, which is completely developed in this thesis.

For a detailed overview of the methodology, Figure 21 shows a flowchart. It can be analyzed the two different groups of the method as explained: analytical and experimental. But since it is necessary some input data from experimental tests, firstly, it is chosen the cutting conditions. Thus, the cutting force measurement gives the necessary force values, while with the high-speed camera measurement it is possible to obtain the chip-tool contact length L_f (see Figure 5), which is necessary to determine the geometry for the analytical models. Besides, with the chip-tool contact length and the force, it is possible to calculate the heat flux for the secondary heat boundary (Equation 8). After the simulated analytical models, it is possible to compare the new transient analytical model for orthogonal cutting simulation. Subsequently, the thermal camera measurement can generate the temperature distribution fields to compare them to analytical results. For last, after good comparison results, the analytical model can be applied to the milling process.

Figure 21 – Methodology summary in details.

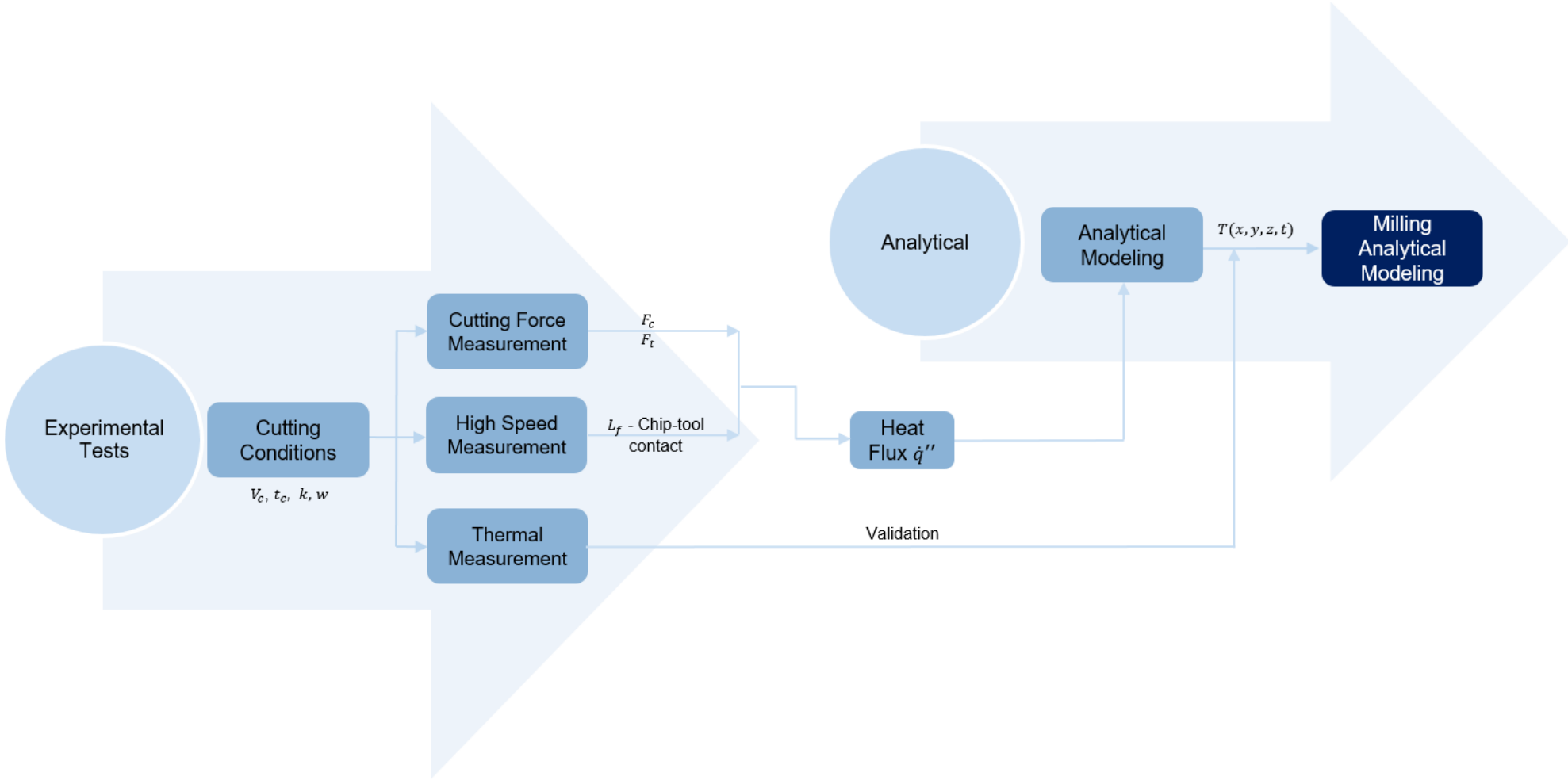

Source: Author.

3.1 MODELING OF THE TEMPERATURE IN THE CUTTING PROCESS USING ANALYTICAL METHOD

It is important to highlight that compared with numerical simulation methods, analytical models have the advantage of being able to provide a clear description of the cutting mechanism, besides resulting in a faster simulation. With this motivation, in order to analyze analytically the temperature in the tool and workpiece during the orthogonal cutting process, it was used different models described in Figure 22 separated in steady and transient states. The fundamentals of the image method and the semi-infinite Green's Function were explained in Chapter 2. The finite three-dimensional Green's Function approach will be developed in this bachelor thesis. All of the integrations were calculated numerically with Python language.

The first analytical model used from the literature was for steady-state, thus, a modification to Jaeger's stationary rectangular heat source solution considering the effect of additional boundary, that is, appropriate image source is considered. This model will be used to analyze after the new transient model. For the transient thermal model from the literature, a semi-infinite geometry Green's Function is considered. After, it is proposed and demonstrated the new geometrical boundary assumption: finite three-dimensional boundary regions. This new model will be compared to semi-infinite geometry and to the steady-state solutions. Subsequently, this model will be compared to orthogonal cutting's experimental data. Figure 23 shows this sequence of the steps for the analytical modeling in detail for the flowchart of the general methodology in Figure 21. For last, the methodology will be applied to the milling process.

Orthogonal cutting was chosen for the analytical model development, so it is possible to compare to experimental data. An orthogonal cutting process has as main cutting conditions a cutting speed V_c and an undeformed chip thickness h. While a milling process presents a rotation of the cutter, and consequently, the undeformed chip thickness varies dependently on the cutter rotation angle. Besides that, with the milling process, due to the complexity of the process, it would be more difficult to measure the temperature in the tool. Thus, the analytical model validated for orthogonal cutting will be applied to a more complex process, in order to show its usability in the industry.

As shown in Figure 22 and Figure 23, some experimental data is necessary as input to the analytical simulation. This data is explained better in Figure 21. The cutting conditions as the definition of the velocity of the experiment, as well as the geometry and material of the tool and geometry of the workpiece are necessary. But also, some values of the tests' results are important to calculate the heat. The forces are taken by the cutting force measurement and the length of chip-tool contact is taken by the high-speed camera measurement. The setup experiment will be explained in Section 3.2. Therefore, with force, velocity, geometries and length of chip-tool contact, it is possible to calculate the heat flux at the secondary heat source, Equation 8 presented in Chapter 2.1.1. Also, with the length of chip-tool contact is possible to determine the geometry of the modeling. It is important to highlight that the heat to the tool for

steel, as the illustration in Figure 9 shows, is about 18%.

Figure 22 – Analytical modeling methodology summary.

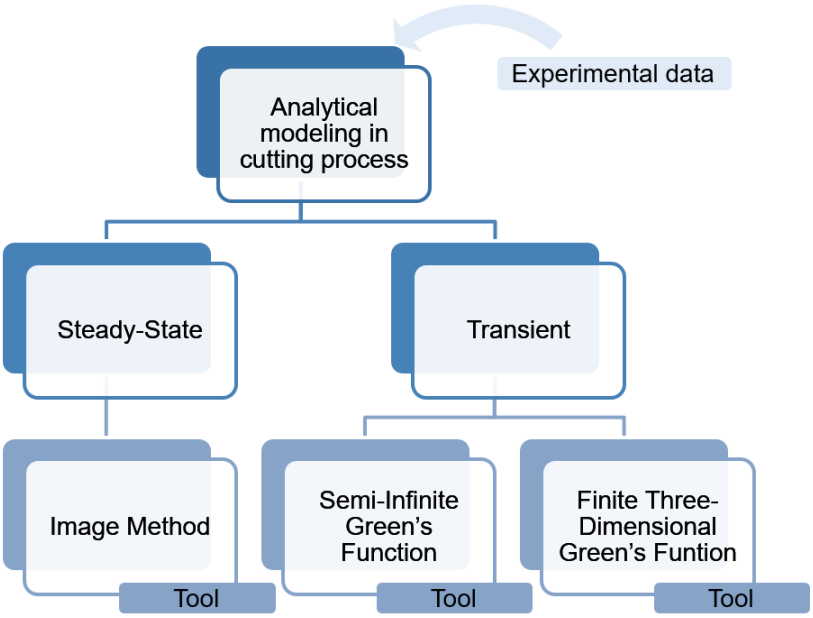

Source: Author.

Figure 23 – Scientific approach for analytical modeling.

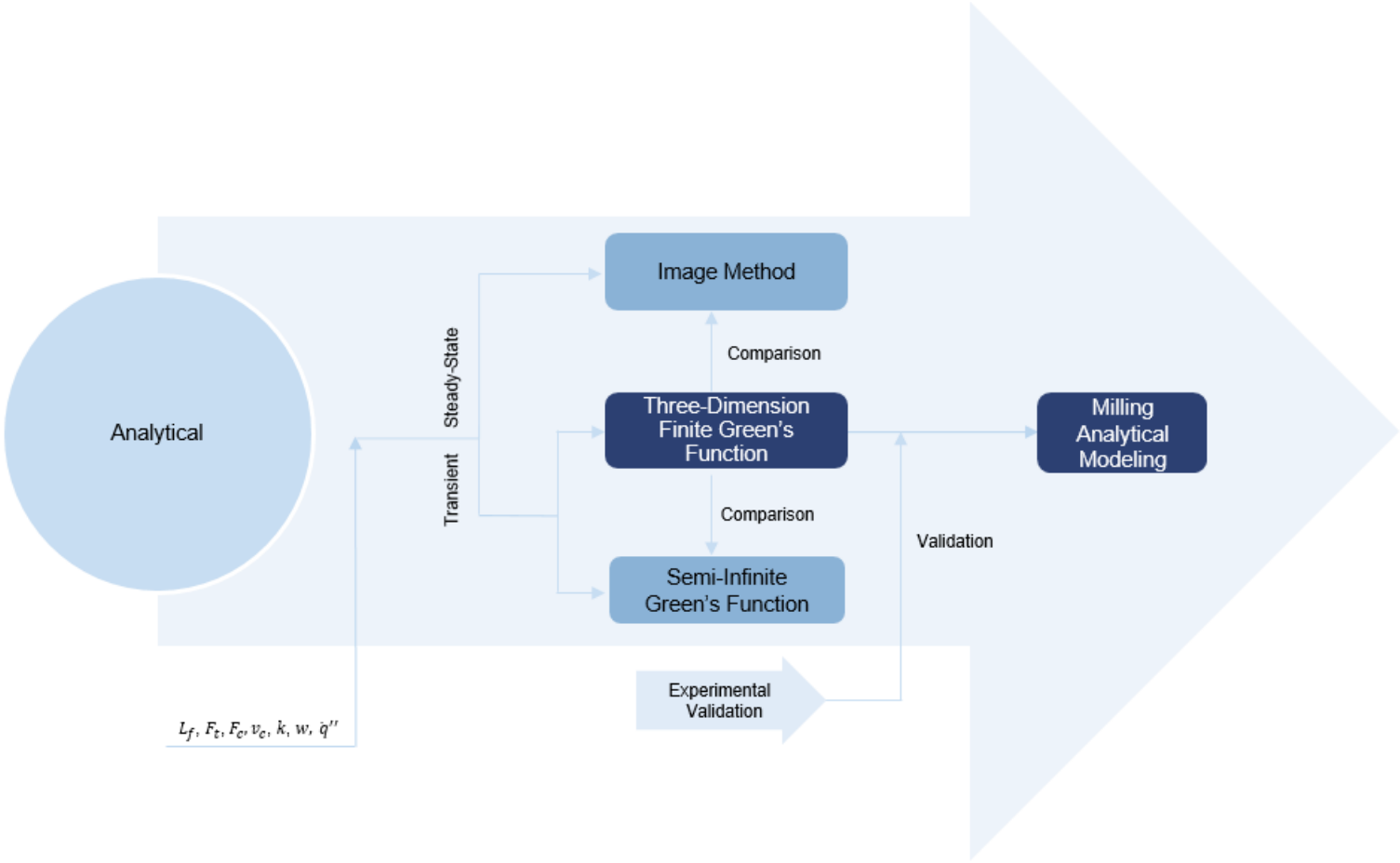

Source: Author.

3.1.1 Steady-State Temperature Fields

In this Section, a thermal model of the orthogonal cutting process to the tool for steady-state is presented. This analytical model will be used to compare its results to the finite three-dimension Green's Function (Section 3.1.2.2), in order to observe if the cutting process in analysis happens in a transient state and how it differs from the steady-state. The model utilized is based on the application of the assumptions and methodology of Veiga et al. (2021). As can be observed from Figure 24, a sharp tool is only affected by the secondary heat source. The effect of this heat source on tool temperature is calculated considering that:

Figure 24 – (a) View of the rake face and secondary zone at the tool-chip interface. (b) Schematic of the stationary rectangular heat source, discretization in the secondary zone and boundary conditions at the tool.

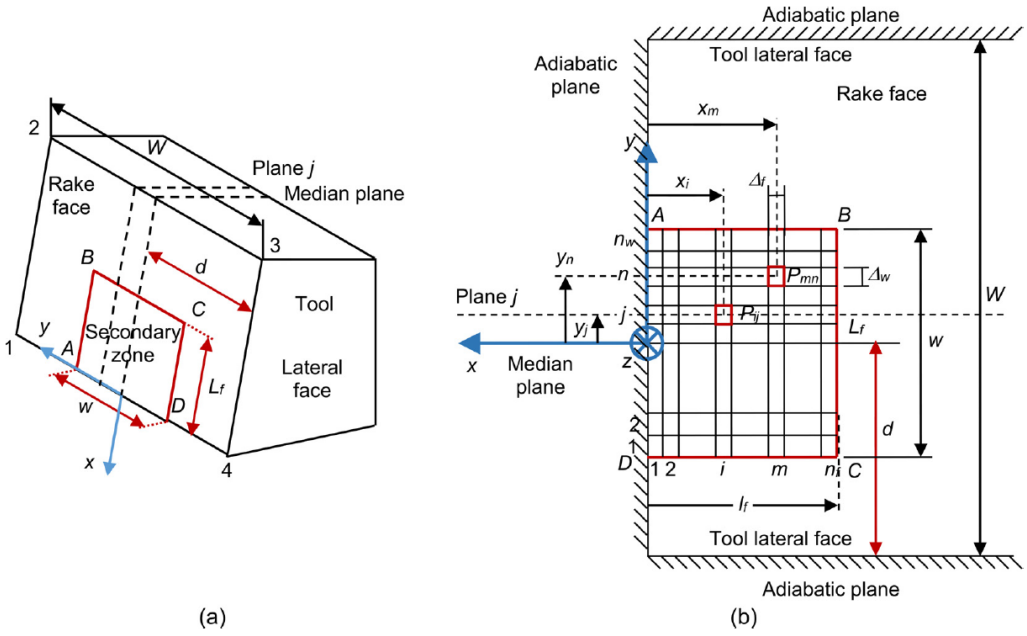

Source: (VEIGA et al., 2021).

a) The secondary heat source acts on the rake face of an edge-shaped cutting tool of width W (Figure 5), as a stationary rectangular heat source with dimensions $L_f \cdot w$, chip-tool contact length.
b) this zone is discretized into a finite number of source elements (Figure 24) in which a constant heat partition coefficient $1 - B(i,j)$ for the tool side is assumed in the source element (i,j). Therefore, the heat that flows into the tool in this source element is $[1 - B(i,j)] \cdot q_f$. The secondary heat source, q_f, can be calculated byEquation 8 presented in Chapter 2.1.1. And the heat partition coefficient, $B(i,j)$, was considered constant, as $B(i,j) = 82\%$. Because how it was delighted before, the heat to the tool for steel is about 18%.
c) As a sharp tool, the flank face of the tool is considered to be adiabatic (KOMANDURI; HOU, 2001a; HUANG; LIANG, 2005; VEIGA et al., 2021).

d) In the model proposed, the lateral faces of the tool (Figure 24) are also assumed to be adiabatic (Figure 24).

Moreover, this model considers two important aspects:

a) Firstly, it is considered the theory of stationary heat sources in semi-infinite solid in order to model secondary deformation zones.
b) Besides that, it is necessary to apply imaginary heat sources (image method) to meet adiabatic boundary conditions in the chip and tool. Imaginary heat sources were defined in the thermal model proposed in such a way that the effect of the tool-chip interface dimensions and of cutting tool width on the tool temperature could be taken into account. This allows the temperature on the rake face and lateral faces of the tool to be predicted (VEIGA et al., 2021).

This model incorporates modifications to Jaeger's solutions for a stationary square heat source for the tool as is used in the literature, e.g., (KOMANDURI; HOU, 2001a). The theory of stationary heat sources in semi-infinite solid was presented in Chapter 2.2.1 can be calculated by Equation 12, as the increment of the temperature at a point $M(x, y, z)$ of a semi-infinite solid due to a stationary rectangular heat source with dimensions $(2a) \cdot (2b)$ and acting on the solid surface.

While the theory of stationary heat source possibilities calculates the temperature in a semi-infinite solid. The imaginary heat sources shown in Figure 25 are taken into consideration in order to meet these boundary conditions, i.e., build the adiabatic planes. The method of images (or method of mirror images) is a mathematical tool for solving differential equations, in which the domain of the function is extended by the addition of its mirror image concerning a symmetry hyperplane. As a result, certain boundary conditions are satisfied automatically by the presence of a mirror image, greatly facilitating the solution of the original problem. As in Figure 26, the plane insulated in Figure 26a is the same as Figure 26b.

Taking the previous discretization of the secondary heat source into account, imaginary heat sources along the y-axis are defined for a source element (i, j). Considering the tool geometry and the position, shape and dimensions of a source element (i, j) acting on the tool rake face, apparent temperature $\theta_{t,f}(x, y, z; x_i, y_j)$ at a tool point $P(x, y, z)$ due to this heat source element (i, j) and its corresponding imaginary heat sources, can be expressed as:

$$\theta_{t,f}(x, y, z; x_i, y_j) = [1 - B(i, j)]\, q_f U_{t,f}(x, y, z; x_i, y_j) \tag{21}$$

Where,

$$\begin{aligned} U_{t,f}(x, y, z; x_i, y_j) = \sum_{q=-n_q}^{n_q} \Bigg[& U_{st}(x - x_i, y - y_q, z; \frac{\Delta f}{2}, \frac{\Delta w}{2}, \lambda_{t0}) \\ & + U_{st}(x + x_i, y - y_q, z; \frac{\Delta f}{2}, \frac{\Delta w}{2}, \lambda_{t0}) \Bigg] \end{aligned} \tag{22}$$

Figure 25 – View of the tool rake face, secondary heat source, the imaginary heat sources and the source element (i, j).

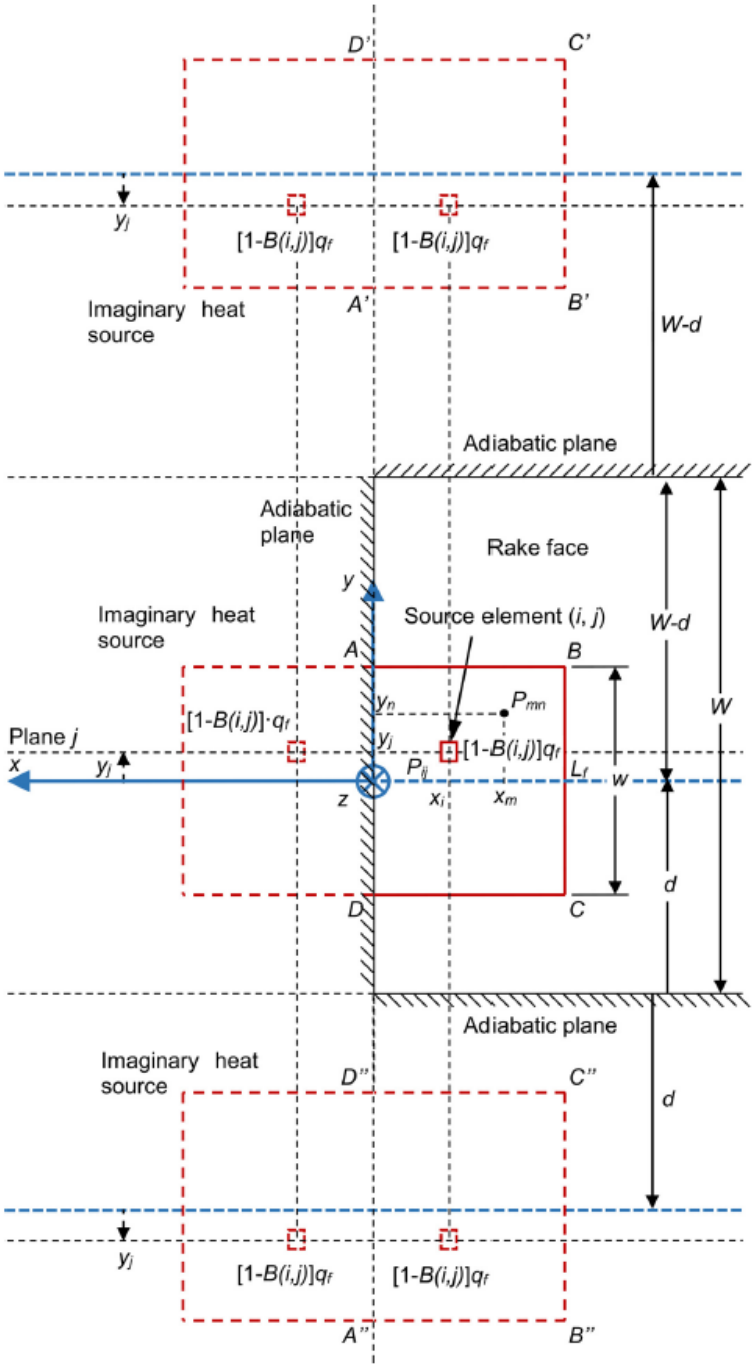

Source: (VEIGA et al., 2021).

In Equation 22, $U_{st}(x, y, z, a, b, \lambda_0)$ represents the increment in temperature at point $P(x, y, z)$ due to a heat source located at point $(xi, yj, 0)$, with dimensions $\Delta f \cdot \Delta w$ and unit heat flux, and can be calculated by Equation 12.

Position y_q of the q imaginary heat source can be expressed as a function of the tool width W (Figure 5), the distance d of the median plane from the tool lateral face (Figure 24) and the position y_j of the source element being taken into consideration (Figure 25):

Figure 26 – Example of how imaginary image method works: (a) Insulated boundary; (b) mirror image source has the same result as insulated boundary.

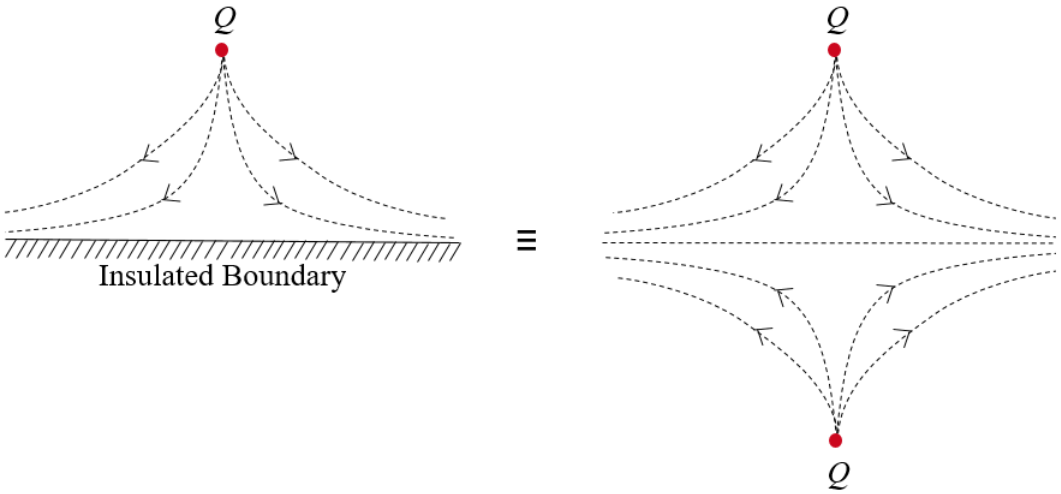

Source: Author.

$$y_q = q \cdot W + (W - 2d) \cdot \frac{1}{2}\left[(-1)^{q+1} + 1\right] + (-1)^q \cdot y_i \tag{23}$$

Finally, the temperature $\theta_{t,f}(x, y, z)$ at point $P(x, y, z)$ of the tool due to secondary heat source can be calculated by considering the contribution made by the $n_f \cdot n_w$ elements in which the secondary zone is discretized:

$$\theta_{t,f}(x, y, z) = \sum_{i=1}^{n_f} \sum_{j=1}^{n_w} \theta_{t,f}(x, y, z; x_i, y_j) \tag{24}$$

This method was implemented using the programming language Python. The input data necessary to run the code is in Table 1, where the material and dimension of the tool, the workpieces' width and the cutting conditions will be presented in Section 3.2. Also, the other necessary parameters that will be obtained only after the experimental tests will be presented in Table 6 in Chapter 4.

3.1.2 Transient Temperature Fields

As explained before in Chapter 2, the thermal conditions in interrupted cutting processes such as milling differ from those in continuous processes such as turning. In interrupted processes, tools are subjected to cyclic heating and cooling, that is, to a transient state. For this reason, it is not possible to apply a stationary analytical method for interrupted cutting. In order to solve inhomogeneous, transient heat conduction problems, Green's Functions have been widely used. For the cutting process, a tool geometry of a semi-infinite rectangular corner has been presented in the literature as presented in State of the Art in Section 2.2.2. This method will be applied in the next Section. However, this solution is not suitable for orthogonal cutting conditions as

presented in Figure 5, in which the workpiece passes the inner surface of the tool. Besides, this type of experimental orthogonal cutting will be used in this bachelor thesis, which more details will be presented in Section 3.2. Furthermore, a finite geometry could result in a more acceptable temperature field for the tool. Thus, a new geometry assumption for the cutting process will be developed in this bachelor thesis: a three-dimension rectangular parallelepiped Green's Function Solution.

3.1.2.1 Tool Temperature for a Semi-infinite Body Assumption

As presented in Section 2.2.2, a solution for the tool temperature in the interrupted cutting process used in the literature is Green's Function for semi-infinite rectangular geometry. This model will be applied for comparison to the new geometry assumption in the next Section 3.1.2.2.

The Green's function for the temperatures in a semi-infinite corner due to an instantaneous point source at time τ at the surface point $x = x_p$, $y = y_p$ and $z = 0$, assuming adiabatic conditions at the boundaries, can be obtained by multiplying the Green's function for three mutually perpendicular instantaneous plane sources in semi-infinite half spaces. Those intersect to form an eighth space or corner as shown in (Figure 16). Where the x, y-plane represents the tool's rake face, the planar heat source, extending over chip-tool contact length L_x and the depth of cut L_y is applied. Thus, the transient temperature field $T(x, y, z, t)$ at a point (x, y, z) in the corner at the time t can be described as a solution of the governing differential equation for transient heat conduction within a continuous medium to

$$\begin{gathered} \frac{\partial^2 T}{\partial x^2}+\frac{\partial^2 T}{\partial y^2}+\frac{\partial^2 T}{\partial z^2}=\frac{1}{\alpha}\frac{\partial T}{\partial t} \\ -\lambda \cdot \frac{\partial T}{\partial z}=\dot{q}''(x,y,t);\ 0 \leqslant x \leqslant L_x;\ 0 \leqslant y \leqslant L_y;\ z=0 \end{gathered} \tag{25}$$

$$T(x,y,z,t)=\frac{\alpha}{\lambda}\int_0^t\int_0^{L_x}\int_0^{L_y} G(x,y,z,t,x_p,y_p,0,D)\cdot\dot{q}''(x_p,y_p,\tau)dx_p dy_p d\tau \tag{26}$$

The variable α represents the thermal diffusivity of the tool material and λ its heat conductivity. The term $\dot{q}''(x_p, y_p, \tau)$ describes the spatial and temporal distribution of the heat flux of the instantaneous, punctual heat sources, and the Green's function of the relevant geometry $G(x, y, z, t, x_p, y_p, 0, D)$. According to (Figure 16), for a spatial uniform heat source, the Green's function for an instantaneous heat impulse over the patch $0 \leqslant y \leqslant L_y$, $0 \leqslant x \leqslant L_x$ can be approximated by:

$$
\begin{aligned}
G(x,y,z,t\,|\,x',y',z',D) = \\
&= \frac{1}{(\sqrt{\pi}D)^3}\left\{exp\left[-\frac{z^2}{D^2}\right]\right\} \\
&\cdot\left\{exp\left[-\frac{(y-y')^2}{D^2}\right]+exp\left[-\frac{(y+y')^2}{D^2}\right]\right\} \\
&\cdot\left\{exp\left[-\frac{(x-x')^2}{D^2}\right]+exp\left[-\frac{(x+x')^2}{D^2}\right]\right\}; \\
&t-\tau \geq 0
\end{aligned}
\tag{27}
$$

$$
D = \sqrt{4\alpha(t-\tau)} \tag{28}
$$

As presented in Section 2.2.2, the final temperature field equation is:

$$
\begin{aligned}
T(x,y,z,L_y,L_z,D) = \frac{a}{\lambda}\int_0^t \frac{1}{2\sqrt{\pi}D}\left\{exp\left[-\frac{(x)^2}{D^2}\right]\right\} \\
\cdot\,\Theta_{GU}(y,L_y,D)\cdot\Theta_{GU}(x,L_x,D)\cdot\dot{q}''(x_p,y_p,\tau)\,d\tau
\end{aligned}
\tag{29}
$$

Where,

$$
\Theta_{GU}(u,L,D) = erf\left(\frac{L+u}{D}\right)+erf\left(\frac{L-u}{D}\right) \tag{30}
$$

Equation 29 was integrated using the programming language Python. The input data necessary to run the code is in Table 1, where the material and dimension of the tool and the cutting conditions will be presented in Section 3.2. Also, the others necessary parameters that will be obtained only after the experimental tests will be presented in Table 6 in Chapter 4.

3.1.2.2 Tool Temperature for a Three-Dimensional Finite Body Assumption

In this bachelor thesis, the model developed was defined for finite three-dimensional body assumption. The tool was considered a small parallelepiped shaped control volume in a stationary, homogeneous, and isotropic body. The energy equation, also called the heat conduction equation, based on the conservation of energy (COLE et al., 2010), when the thermal conductivity does not depend on position (for example, when the temperature gradients are not too large), can be written as Equation 31:

$$
\frac{\partial^2 T}{\partial x^2}+\frac{\partial^2 T}{\partial y^2}+\frac{\partial^2 T}{\partial z^2}+\frac{1}{k}g(x,y,z,t) = \frac{1}{\alpha}\frac{\partial T}{\partial t} \tag{31}
$$

Where $\alpha = k/(\rho c)$ is the thermal diffusivity (m^2/s), k is the thermal conductivity $(W/(m.K))$, ρ is the density (kg/m^3), c is the specific heat capacity $(J/(kg.K))$, and $g(x, y, z, t)$ is the energy generation (W/m^3).

In a solid body with a temperature gradient, heat flux has a magnitude and a direction, and it is denoted by vector $\vec{q}$. The component of heat flux, in a direction of coordinate x is given by the Equation 32:

$$\dot{q}''(x', y', \tau) = -k\frac{\partial T}{\partial z};\ L_{x_1} \leqslant x \leqslant L_{x_2};\ 0 \leqslant y \leqslant L_{y_2} \leqslant;\ z = c_1 = 0 \tag{32}$$

Figure 27 – Tool as three-dimension rectangular parallelepiped geometry with second kind of boundary conditions. The secondary heat source in orthogonal cutting is the x, y-plane (the rake face), which is defined by the chip-tool contact length and the depth of cut (length of $L_{x_2} - L_{x_1}$).

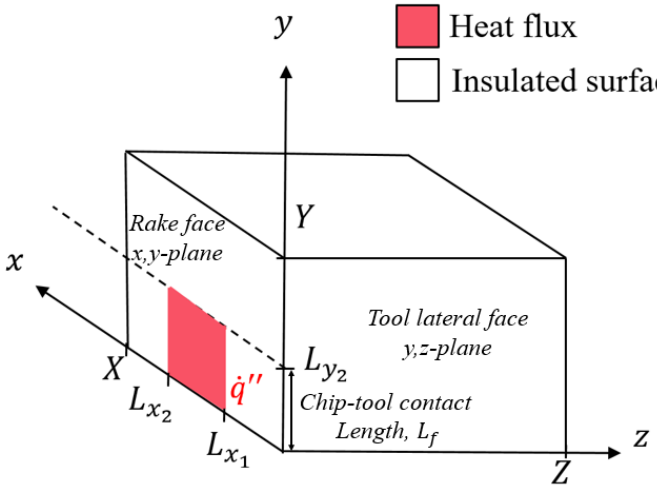

Source: Author, 2021.

Figure 28 – Orthogonal Cutting.

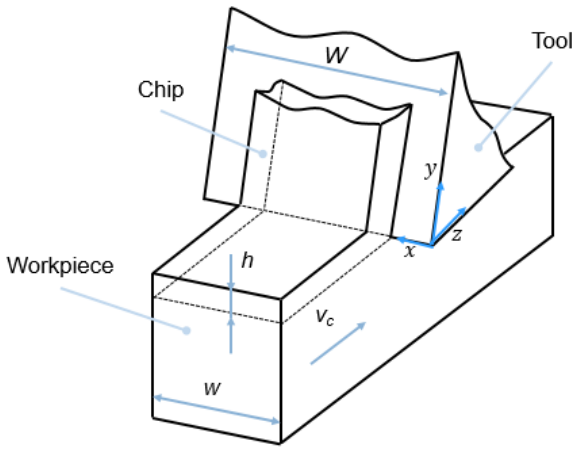

Source: provided by LIU, Hui; 2022.

The GFSE for a three-dimensional rectangular parallelepiped region of $a_1 \leq x \leq a_2$, $b_1 \leq y \leq b_2$, $c_1 \leq z \leq c_2$ as in Figure 28, with the initial temperature of $F(x, y, z)$, is determined

by Equation 33 (COLE et al., 2010).

$$
\begin{aligned}
T(x,y,z,t) = & \int_{x'=a_1}^{a_2}\int_{y'=b_1}^{b_2}\int_{z'=c_1}^{c_2} G(x,y,z,t\,|\,x',y',z',0)F(x',y',z')dx'dy'dz' + \\
& + \frac{\alpha}{k}\int_{\tau=0}^{t}\int_{x'=a_1}^{a_2}\int_{y'=b_1}^{b_2}\int_{z'=c_1}^{c_2} G(x,y,z,t\,|\,x',y',z',\tau)g(x',y',z',\tau)dx'dy'dz'd\tau \\
& + I_{x'=a_1} + I_{x'=a_2} + I_{y'=b_1} + I_{y'=b_2} + I_{z'=c_1} + I_{z'=c_2}
\end{aligned}
\tag{33}
$$

In rectangular coordinates, one-dimensional transient GFs can be multiplied together to form two- and three-dimensional GFs under the following restrictions: (1) the boundary conditions are of the type 0, 1, 2, or 3 (types 4 and 5 are not permitted); (2) if boundary conditions of the third type are present, the heat transfer coefficient h_i must be a constant for a given surface s_i. Some of this boundary conditions are determined by a body with an isothermal surface or an insulated surface. For example, a prescribed temperature at a boundary is called a boundary condition of the first kind. The homogeneous isothermal case is for the surface temperature (at $x = 0$) held at $0°C$. If the prescribed temperature is zero, the boundary condition is termed homogeneous. whereas for a prescribed heat flux at a surface, it is called a boundary condition of the second kind; if this heat flux is zero, the surface is said to be insulated and the boundary condition is also homogeneous.

For the geometry assumed, boundary conditions are of second kind, e.g., insulated surface (Figure 28). Thus, the three-dimensional GF in rectangular coordinates can be found from a product of three one-dimensional GFs; that is, $G_{XYZ} = G_X \cdot G_Y \cdot G_Z$ (COLE et al., 2010).

$$
G(x,y,z,t\,|\,x',y',z',\tau) = G(x,t\,|\,x',\tau)\ \cdot\ G(y,t\,|\,y',\tau)\ \cdot\ G(z,t\,|\,z',\tau) \tag{34}
$$

Therefore, Equation 33 can be written as Equation 35:

$$
\begin{aligned}
T(x,y,z,t) = & \int_{x'=a_1}^{a_2}\int_{y'=b_1}^{b_2}\int_{z'=c_1}^{c_2} G_{XIJ}(x,t\,|\,x',0)G_{YKL}(y,t\,|\,y',0) \\
& \cdot G_{ZMN}(z,t\,|\,z',0)F(x',y',z')dx'dy'dz' + \\
& + \frac{\alpha}{k}\int_{\tau=0}^{t}\int_{x'=a_1}^{a_2}\int_{y'=b_1}^{b_2}\int_{z'=c_1}^{c_2} G_{XIJ}(x,t\,|\,x',\tau)G_{YKL}(y,t\,|\,y',\tau) \\
& \cdot G_{ZMN}(z,t\,|\,z',\tau)g(x',y',z',\tau)dx'dy'dz'd\tau \\
& + I_{x'=a_1} + I_{x'=a_2} + I_{y'=b_1} + I_{y'=b_2} + I_{z'=c_1} + I_{z'=c_2}
\end{aligned}
\tag{35}
$$

The notation G_{XIJ} refers to the GF specific to the rectangular coordinate type of boundary condition on the boundaries $x = a_1$ and $x = a_2$. Similarly, G_{YMN} the GF for their

type of boundary conditions. The last six terms denoted I depend on the type of the boundary condition, of the zeroth, first, second, or third kinds.

The boundary condition at $x = a_1$ can be written as:

$$-k_{a_1}\frac{\partial T(a_1, y, z, t)}{\partial x} + h_{a_1}T(a_1, y, z, t) = f_{a_1}(y, z, t) \tag{36}$$

Where $Ta_1(y, z, t)$ is the prescribed temperature history at $x = a_1$. For the boundary condition of the second kind, the values are:

$$-k_{a_1} = k; \quad h_{a_1} = 0; \quad f_{a_1}(y, z, t) = q_{a_1}(y, z, t) \tag{37}$$

For example, boundaries conditions of second or third kinds at $x = a_1$ will have term $I_{x=a_1}$ as Equation 38. The same occurs if the other boundary conditions are the second kind.

$$I_{x=a_1} = \frac{\alpha}{k}\int_{\tau=0}^{t}\int_{y'=b_1}^{b_2} G_{XIJ}(x, t \,|\, a_1, \tau)G_{YMN}(y, t \,|\, y', \tau)G_{ZMN}(z, t \,|\, z', \tau)f_{x_1}(a_1, y', z', \tau)dy'dz'd\tau \tag{38}$$

Considering second kind of boundary conditions as the Figure 28 and $F(x, y, z, 0) = 20°C$ (room temperature), $g = 0$, $f_{c_1} = \dot{q}''$ and $f_{c_2} = f_{a_1} = f_{a_2} = f_{b_1} = f_{b_2} = 0$. As explained before in Section 3.1.1, a sharp tool is only affected by the secondary heat source, and $\dot{q}''$ can be calculated by 18% of Equation 8.So the temperature $T(x, y, t)$ is:

$$\begin{aligned} T(x, y, z, t) = &\int_{x'=a_1}^{a_2}\int_{y'=b_1}^{b_2}\int_{z'=c_1}^{c_2} G_{XIJ}(x, t \,|\, x', 0)G_{YKL}(y, t \,|\, y', 0) \\ &\cdot G_{ZMN}(z, t \,|\, z', 0)F(x, y, z, 0)dx'dy'dz' + \\ &+ \frac{\alpha}{k}\int_{\tau=0}^{t}\int_{x'=L_{x_1}}^{L_{x_2}}\int_{y'=L_{y_1}}^{L_{y_2}} G_{XIJ}(x, t \,|\, x', \tau)G_{YKL}(y, t \,|\, y', \tau) \\ &\cdot G_{ZMN}(z, t \,|\, c_1, \tau)\dot{q}''dx'dy'd\tau \end{aligned} \tag{39}$$

Besides, for boundaries conditions as $\frac{\partial G}{\partial x} = 0$ at $x = 0$ and $x = L$ (second kind), the best expression for small cotimes is (AUGSPURGER, 2018):

$$\begin{aligned} G_{X22}(x, t \,|\, x', \tau) = [4\pi\alpha(t-\tau)]^{-1/2}\sum_{n=-\infty}^{\infty}\Bigg\{&exp\left[-\frac{(2nL + x - x')^2}{4\alpha(t-\tau)}\right] \\ &+ exp\left[-\frac{(2nL + x + x')^2}{4\alpha(t-\tau)}\right]\Bigg\} \end{aligned} \tag{40}$$

For small values of $\alpha(t - \tau)/L^2 \leq 0,25$, it is possible to use the expression:

$$G_{X22}(x,t\,|\,x',\tau) \approx [4\pi\alpha(t-\tau)]^{-1/2}\left\{exp\left[-\frac{(x-x')^2}{4\alpha(t-\tau)}\right] + exp\left[-\frac{(x+x')^2}{4\alpha(t-\tau)}\right] + exp\left[-\frac{(2L-x-x')^2}{4\alpha(t-\tau)}\right]\right\} \tag{41}$$

Substituting Equation 41 in Equation 39, it is obtained the Equation 42:

$$\begin{aligned}
T(x,y,z,t) = {} & F(x,y,z,0)\int_{x'=a_1}^{a_2}[4\pi\alpha(t)]^{-1/2}\left\{exp\left[-\frac{(x-x')^2}{4\alpha(t)}\right] + exp\left[-\frac{(x+x')^2}{4\alpha(t)}\right]\right. \\
& \left. + exp\left[-\frac{(2L-x-x')^2}{4\alpha(t)}\right]\right\}dx' \\
& \cdot\int_{y'=b_1}^{b_2}[4\pi\alpha(t)]^{-1/2}\left\{exp\left[-\frac{(y-y')^2}{4\alpha(t)}\right] + exp\left[-\frac{(y+y')^2}{4\alpha(t)}\right]\right. \\
& \left. + exp\left[-\frac{(2L-y-y')^2}{4\alpha(t)}\right]\right\}dy' \\
& \cdot\int_{z'=c_1}^{c_2}[4\pi\alpha(t)]^{-1/2}\left\{exp\left[-\frac{(z-z')^2}{4\alpha(t)}\right] + exp\left[-\frac{(z+z')^2}{4\alpha(t)}\right]\right. \\
& \left. + exp\left[-\frac{(2L-z-z')^2}{4\alpha(t)}\right]\right\}dz' + \\
& + \frac{\alpha}{k}\int_{\tau=0}^{t}\int_{x'=L_{x_1}}^{L_{x_2}}[4\pi\alpha(t-\tau)]^{-1/2}\left\{exp\left[-\frac{(x-a_1)^2}{4\alpha(t-\tau)}\right] + exp\left[-\frac{(x+a_1)^2}{4\alpha(t-\tau)}\right]\right. \\
& \left. + exp\left[-\frac{(2L-x-a_1)^2}{4\alpha(t-\tau)}\right]\right\} \\
& \cdot\int_{y'=L_{y_1}}^{L_{y_1}}[4\pi\alpha(t-\tau)]^{-1/2}\left\{exp\left[-\frac{(y-y')^2}{4\alpha(t-\tau)}\right] + exp\left[-\frac{(y+y')^2}{4\alpha(t-\tau)}\right]\right. \\
& \left. + exp\left[-\frac{(2L-y-y')^2}{4\alpha(t-\tau)}\right]\right\} \\
& \cdot[4\pi\alpha(t-\tau)]^{-1/2}\left\{exp\left[-\frac{(z-c_1)^2}{4\alpha(t-\tau)}\right] + exp\left[-\frac{(z+c_1)^2}{4\alpha(t-\tau)}\right]\right. \\
& \left. + exp\left[-\frac{(2L-z-c_1)^2}{4\alpha(t-\tau)}\right]\right\}\dot{q}''(x',y',\tau)dx'dy'd\tau
\end{aligned} \tag{42}$$

It is important to remind D determined by Equation 16 in Section 2.2.2, which is the scaling factor or characteristic dimension for the penetration of the temperature field at time t due to an instantaneous heat source at the time τ.

$$D = \sqrt{4\alpha(t-\tau)} \tag{43}$$

Using the error function, $erf()$, that is defined by Equation 44 (COLE et al., 2010), a part of the integration at Equation 42 can be written as Equation 45, substituting $\frac{x+x'}{D}$ by w.

$$erf(x) = \frac{2}{\sqrt{\pi}} \int_0^x e^{-t^2} dt \tag{44}$$

$$\begin{aligned} \int_{x'=a_1}^{a_2} exp\left[-\left(\frac{x+x'}{D}\right)^2\right] dx' &= D \int_{\frac{x+a_1}{D}}^{\frac{x+a_2}{D}} exp\left(-(w)^2\right) dw \\ &= D\frac{\sqrt{\pi}}{2}\left[erf\left(\frac{x+a_2}{D}\right) - erf\left(\frac{x+a_1}{D}\right)\right] \end{aligned} \tag{45}$$

The same procedure can be applied for $\frac{x-x'}{D}$, substituting it by w:

$$\begin{aligned} \int_{x'=a_1}^{a_2} exp\left[-\left(\frac{x-x'}{D}\right)^2\right] dx' &= -D \int_{\frac{x-a_1}{D}}^{\frac{x-a_2}{D}} exp\left(-(w)^2\right) dw \\ &= -D\frac{\sqrt{\pi}}{2}\left[erf\left(\frac{x-a_2}{D}\right) - erf\left(\frac{x-a_1}{D}\right)\right] \end{aligned} \tag{46}$$

Moreover, for $\frac{2L-x-x'}{D}$:

$$\begin{aligned} \int_{x'=a_1}^{a_2} exp\left[-\left(\frac{2L-x-x'}{D}\right)^2\right] dx' &= -D \int_{\frac{x-a_1}{D}}^{\frac{x-a_2}{D}} exp\left(-(w)^2\right) dw \\ &= -D\frac{\sqrt{\pi}}{2}\left[erf\left(\frac{2L-x-a_2}{D}\right) - erf\left(\frac{2L-x-a_1}{D}\right)\right] \end{aligned} \tag{47}$$

Thus, one integration of Equation 42, it is defining by multiplying the term $[4\pi\alpha(t)]^{-1/2}$ by the sum of Equations 45, 46 and 47:

$$\begin{aligned} \int_{x'=a_1}^{a_2} G_{X22}(x,t|x',\tau)dx' = \frac{1}{2}\Bigg\{ &\left[erf\left(\frac{x+a_2}{D}\right) - erf\left(\frac{x+a_1}{D}\right)\right] \\ &- \left[erf\left(\frac{x-a_2}{D}\right) - erf\left(\frac{x-a_1}{D}\right)\right] \\ &- \left[erf\left(\frac{2L-x-a_2}{D}\right) - erf\left(\frac{2L-x-a_1}{D}\right)\right]\Bigg\} \end{aligned} \tag{48}$$

Finally, applying the Equation 48 for both y and z, and using them with Equation 43 in Equation 42, it results in Equation 49:

$$
\begin{aligned}
T(x,y,z,t) = \frac{F(x,y,z,0)}{8} \cdot \prod_{\substack{u\,=\,x,\,y,\,z \\ U\,=\,X,\,Y,\,Z}} & \left\{ erf\left[\frac{(u+U)}{D\Big|_{\tau=0}}\right] - erf\left[\frac{(u-U)}{D\Big|_{\tau=0}}\right] \right. \\
& \left. - erf\left[\frac{(U-u)}{D\Big|_{\tau=0}}\right] + erf\left[\frac{(2U-u)}{D\Big|_{\tau=0}}\right] \right\} \\
+ \frac{\alpha}{k} \int_{\tau=0}^{t_c} & \frac{1}{4\sqrt{\pi}D} \left\{ 2exp\left(-\frac{z^2}{D^2}\right) + exp\left[-\frac{(2Z-z)^2}{D^2}\right] \right\} \\
\cdot \prod_{\substack{u\,=\,x,\,y \\ U\,=\,X,\,Y}} & \left\{ erf\left[\frac{(u+L_{u_2})}{D}\right] - erf\left[\frac{u+L_{u_1}}{D}\right] \right. \\
& - erf\left[\frac{(u-L_{u_2})}{D}\right] + erf\left[\frac{u-L_{u_1}}{D}\right] \\
& \left. - erf\left[\frac{2U-u-L_{u_2}}{D}\right] + erf\left[\frac{2U-u-L_{u_1}}{D}\right] \right\} \\
& \cdot \dot{q}''(x',y',\tau)d\tau
\end{aligned}
\tag{49}
$$

This equation was integrated using the programming language Python. The input data necessary to run the code is in Table 1, where the material and dimension of the tool, the workpieces' width and the cutting conditions will be presented in Section 3.2. Also, the other necessary parameters that will be obtained only after the experimental tests will be presented in Table 6 in Chapter 4.

3.2 TEMPERATURE IN THE CUTTING PROCESS USING EXPERIMENTAL METHOD

All orthogonal cutting experiments were performed on a vertical external broaching machine tool of type FORST RASX 8 × 2200 × 600 M/CNC, as shown in Figure 31 by Number 1. With a turning machine, it would not be possible to have a good camera position to capture the process. The general setup for the orthogonal cutting process performed can be observed in Figure 29. Where the workpieces of size $42mm \times 3mm \times 200mm$ and material C45E (equivalent to AISI 1045) were fixed in the machine slide and performed the main cutting movement against the motionless tool.

DIN C45E steel is medium carbon steel. It also is a general engineering structural steel. It has good machinability and high tensile properties. C45E was selected because steel is the most important representative for metallic materials and for cutting technology. Especially, the steel grade C45E shows a continuous chip formation for the chosen cutting parameters, which is important for the measurement of tool-chip length contact (BRÖMMELHOFF et al., 2013).

The cutting tools used were 5TGN10NX-036182 B2F3 SANDVIK grooving inserts (coated cemented carbide). Cemented carbide is a hard material used extensively as cutting tool

material, as well as other industrial applications. It consists of fine particles of carbide cemented into a composite by a binder metal. The thermal conductivity utilized in analytical models, k, was $51,9W/(m.K)$, a density ρ of value $1,48E+04(kg/m^3)$, and a specific heat capacity, c, of $198,0(J/(kg.K))$ (VORNBERGER et al., 2020; OTAI, 2020). The tool has a rake angle $\gamma = 12.0°$ and a flank angle of $\alpha = 3°$ have been used. The approximated dimensions are $4,6mm$ x $25mm$ x $5mm$.

Figure 29 – Schematic drawing of the orthogonal cutting process performed. The workpiece is fixed in the machine slide and performs the cutting movement against the motionless tool.

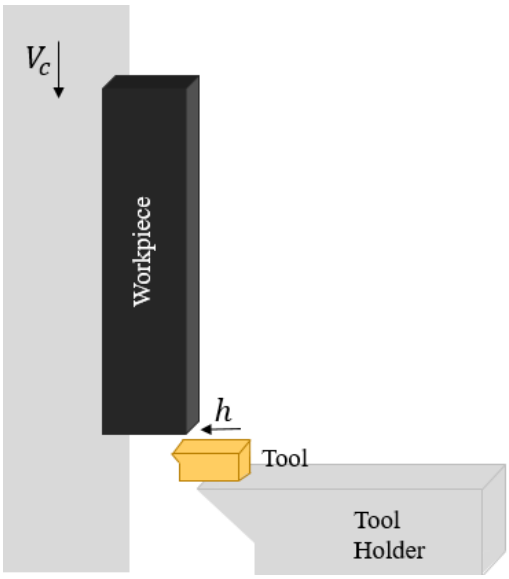

Source: Author.

A wide variation of cutting speed V_c was applied in this study. The used cutting parameters were $V_c = 100,0; 120,0$ and $150,0m/min$ for the cutting speed and $h = 0,30mm$ for the undeformed chip thickness. For each velocity, it is possible to calculate the time of cutting. The workpieces' height, as mentioned before, is 200 mm. Thus, the time of cutting is, $t = 200mm/V_c$, i.e., $t = 0,08; 0,1$ and $0,12s$ respectively. All experiments were repeated twice. The methodology is presented in three different kinds of experiments, as Figure 30 shows.

The grooving insert tool was clamped onto a KISTLER Z21289 piezoelectric dynamometer with a measurement range from -80 to 80 kN in cutting force direction (MEURER et al., 2020) to measure the forces during the cutting, which are necessary to calculate the heat flux utilized in the analytical models. In Figure 31 is possible to observe the dynamometer (Number 2). The resulted forces were cutting force, F_c, and thrust force, F_t were analyzed in the software DIAdem, where it is possible to calculate both average values. How each experiment was repeated twice for better accuracy, the value of each force was calculated by the average of both experiments.

Besides the measurement of the force, the experimental setup offers the possibility to capture the cutting process using ultra-high-speed camera techniques: Vision Research phantom

Figure 30 – Experimental methodology.

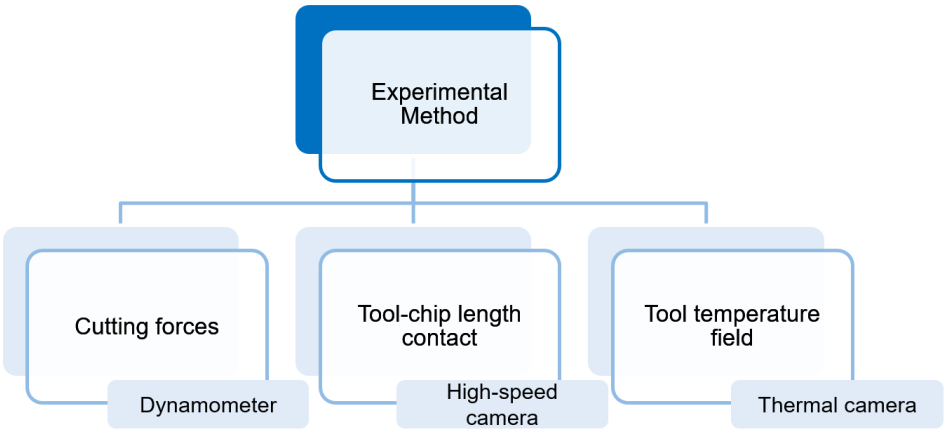

Source: Author.

v7.3 with an exposure of 25 μs and resolution of 800x600. This test was realized for measuring the length of tool-chip contact, L_f, which can be realized by the Phantom Camera Control (PCC) Software. In Figure 31 the high-speed Camera is identified by Number 6, and this experiment setup can be seen in the middle image. The LED Right light (Number 5), GDVitec MultiLed, was used to get better image results. This measurement captures the cutting process by the right lateral side of the experiment, as shown in Figure 31.

After the cutting conditions as velocity V_c and undeformed chip thickness h, and the material of the tool (k, rho, c) defined (Table 1), and with the results of the forces obtained by the dynamometer and the length of tool-chip contact, L_f, obtained by the high-speed camera, it is possible to apply these values in the analytical modeling. This sequence can be observed in Figure 21.

The last part of the methodology for experiments as Figure 30 shows is the tool temperature measurement. In the State of Art (Section 2.3) was presented the three principal methods in the literature and their principles: thermocouples, pyrometers and thermometry. While pyrometry is the contact-free determination of the absolute temperature of one point of the object. Thermography provides a pictorial representation of temperature distribution. For this reason, thermography was chosen as the measurement method of temperature. A thermographic camera Flir SC 7600 recorded the infrared radiation of the fixed tool's lateral face during the orthogonal cutting by the left side. It was used black coating in order to enhance and homogenize the absorptivity and emissivity. The thermo camera can be seen in Figure 31 by Number 8. Its setup can be analyzed in the upper right image. The resulting field of view (FOV) has a resolution of 380x400 pixels. The sensor had a pixel pitch of $15\mu m$.

Table 1 – List of parameter's values for the analytical models (Part I). The ■, ▲ and ★ symbols represent which parameters are necessary for the image method, semi-infinite Green's function solution and three-dimension finite Green's function solution, respectively.

Parameter	**Symbol**	**Value**
Thermal conductivity	k ■▲★	$51,9\ [W/(m.K)]$
Density	ρ ▲★	$1,48E+04\ [kg/m^3]$
Specific heat	c▲, ★	$198,0\ [J/(kg.K)]$
Workpiece's width	w ■▲★	$3,0\ [mm]$
Tool's width	$W = X$ ■★	$4,6\ [mm]$
Tool's height and length	Z x Y ★	5 x 25 $[mm^2]$
Rake Angle	γ ■▲★	$12,0°$
Shear angle	Φ ■▲★	$45,0°$
Cutting speed	V_c ■▲★	$100,0; 120,0; 150,0\ [m/min]$
Undeformed chip thickness	h	$0,3\ [mm]$
Time of cutting	t_c ■▲★	$0,08; 0,01; 0,12\ [s]$

Figure 31 – Experimental setup for the orthogonal cutting experiments.

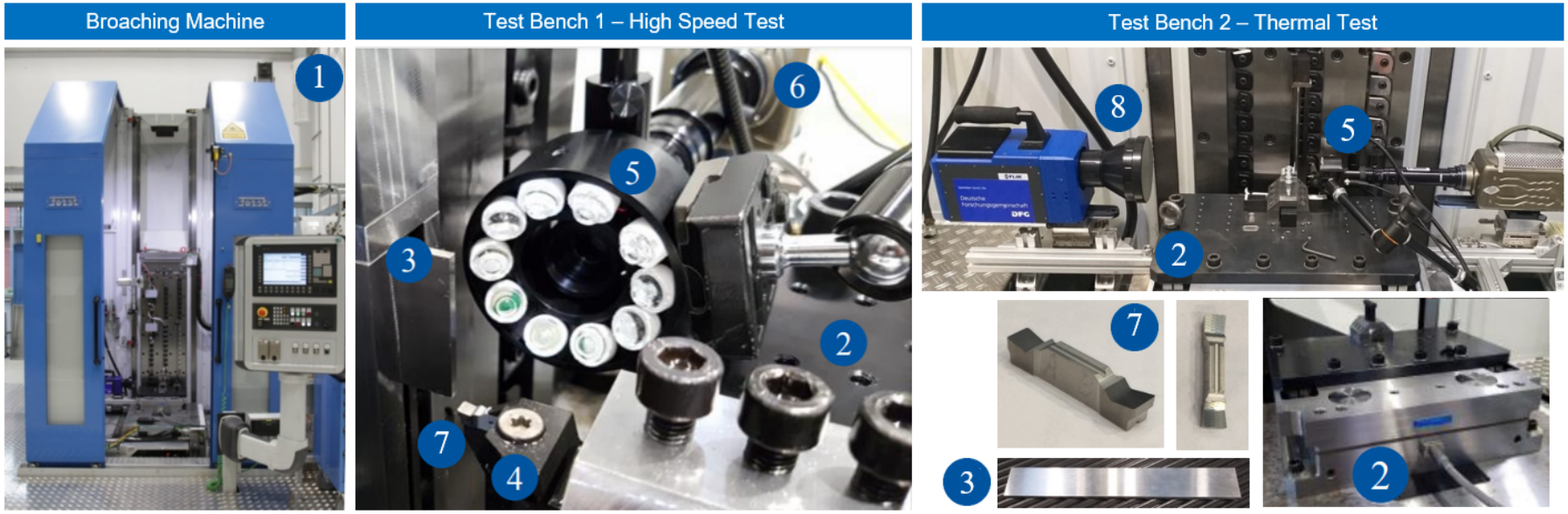

Source: Author.

3.3 APPLICATION OF THE TOOL TEMPERATURE ANALYTICAL MODEL TO MILLING PROCESS

Orthogonal cutting was chosen for the analytical model development, so it is possible to compare to experimental data. An orthogonal cutting process has as main cutting conditions a cutting speed V_c and an undeformed chip thickness h. While a milling process presents a rotation of the cutter, and consequently, the undeformed chip thickness varies dependently on the cutter rotation angle. Besides that, with the milling process, due to the complexity of the process, it would be more difficult to measure the temperature in the tool. Thus, the analytical model validated for orthogonal cutting will be applied to a more complex process, in order to show its usability in the industry.

After all the procedures for the analytical modeling for orthogonal cutting process in this bachelor thesis and its validation by experimental tests, as explained in Section 3.1, the GFSE-3D analytical model developed will be applied to the milling process as an example of application in a process widely used the industry. Moreover, understanding the high frequent temperature fluctuations in the interrupted process is crucial to predict the alternating strains in the material, tool wear and cracks. For a summary of this application methodology, Figure 23 shows the steps until the final analytical model to the milling. It was used the solution Green's Function for a three-dimension finite geometry assumption developed in Section 3.1.2.2.

Augspurger (2018) predicted the tool temperature for milling applying the GREEN'S function for a semi-corner, approximating the cutting-edge geometry, as the theory presented in Section 3.1.2.1. It simulated time-variant temperature fields $T(x, y, z, t)$ in the tool approximated by a semi-infinite corner during milling as the result of the former empirically modeled transient tool load $\dot{Q}_{tool}(t, v_c, a_e, d, f_z)$. This analytical temperature model is based on the solution of the partial differential equation for heat conduction through GREEN´S functions. Its specific characteristics make it potentially suitable for modeling transient temperature fields in the tool for the orthogonal cutting process as well as the milling process. Hence, it was capable to predict time-variant volumetric temperature fields in a defined geometry, even though the tools used in the milling experiments deviate from the assumption of the semi-infinite corner by the clearance as well as rake angle.

In this bachelor thesis, it will be used the same methodology utilized by Augspurger (2018), but for a different geometry assumption. It will be applied the three-dimension finite Green's Function presented in Section 3.1.2.2. Previously, it was applied the transient temperature fields in the tool for the orthogonal cutting process for continuous process, in order to compare the modeling results to the experimental data. For milling application, as explained before, the heat is non-continuous due to milling being an interrupted process. The following analytical formulation was used. The same Equation 39 can be utilized for $L_{x1} = 0$, $L_{x2} = L_x = w$, $L_{y1} = 0$, $L_{y2} = L_f$. The difference is that $\dot{q}''$ is non-uniform during the cutting time. Thus, the Equation 49 is utilized for:

$$\dot{q}''(t) = a_e \cdot \frac{d}{2} \cdot q_{tool,l_c,a_p}(h(\Phi), v_c) \cdot \frac{d\Phi}{dt} \cdot 1,188/(L_x \cdot L_y)$$
$$\dot{Q}''(t) = \dot{q}'' \cdot L_x \cdot L_y \tag{50}$$

$$h(\Phi) = f_z \cdot sin(\Phi) \tag{51}$$

Where, a_e is the width of cut, d is the diameter of the tool, l_c is the cutting length, a_p is the depth of cut, v_c is the velocity of cut, f_z is the feed per tooth, L_x is also the depth of cut, and L_y is the chip-tool contact length. In Figure 32, the geometry for the application of the modeling in Peripheral Milling can be observed. The coordinate system is rotated with the tool, with y in the rake face and x in the clearance face direction. Besides that, more details about the kinematics of this process can be seen in Figure 12 and Figure 13 in Section 2.1.2. The parameters for the simulation of this analytical model can be obtained in Table 2. These values were taken from the Augspurger (2018)'s doctoral thesis, as an empirically input model.

Figure 32 – Milling process.

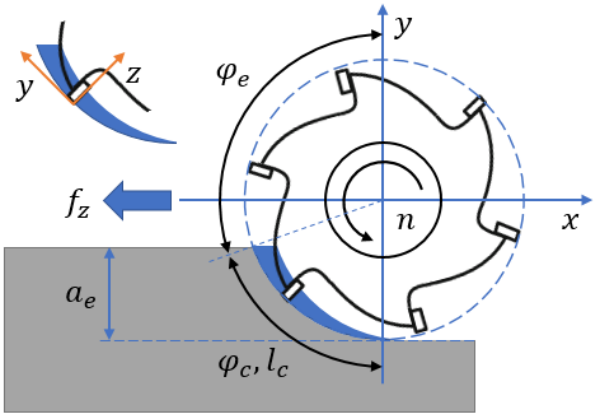

Source: provided by LIU, Hui, 2022.

Table 2 – List of parameter's values for the analytical milling model.

Parameter	Symbol	Value
Depth of cut	a_p	$3,0\ [mm]$
Width of cut	a_e	$3,75\ [mm]$
Tool diameter	d	$20,0\ [mm]$
Feed per tooth	f_z	$0,05\ [mm]$
Thermal diffusivity	α	$1,7E-05\ [m^2/s]$
Cutting speed	v_c	$35\ [m/min]$
Time	t	$1\ [s]$

The dependence $q_{tool,l_c,a_p}(h(\Phi), v_c)$ utilized is also provided by Auspurger, which is approximated via a three dimensional regression fitting a second degree polynomial h and v_c by measured specific heat inputs in the orthogonal cutting experiments. This way for the tool the following formulation was derived from the measurements (AUGSPURGER, 2018):

$$q_{tool,l_c,a_p}(h(\Phi), v_c) = p_{00} + p_{10} \cdot h + p_{01} \cdot v_c + p_{20} \cdot h^2 + p_{11} \cdot h \cdot v_c + +p_{02} \cdot v_c^2 \tag{52}$$

For AISI 1045 the formulation used the coefficients in Table 3. This formulation is valid between the parameter range from $v_c = 35m/min$ to $140m/min$ and $h = 0mm$ to $0,1mm$. With the cutting velocity, the heat flow into the tool rises yet the duration of the cut is shorter. The integral of the Equation 50 defines the heat input into the tool. In order to derive a continuous function of the heat flow over several engagements including the cutting interruption Q_{tool} a spline interpolation was applied to describe the heat flow piecewise by polynomials.

Table 3 – List of coefficient's values of Equation 52 for AISI 1045.

Coefficient	**Value**
p_{00}	$0,00292$
p_{10}	$0,1663$
p_{01}	$-6,089E-05$
p_{20}	$-0,5697$
p_{11}	$-5,243E-05$
p_{02}	$2,53E-07$

Source: (AUGSPURGER, 2018).

4 RESULTS AND DISCUSSION

In this chapter is presented the results of the analytical modeling in the continuous and interrupted cutting process and its experimental tests comparison. Firstly, it is approached the experimental measurement's results: the cutting forces and the high-speed camera measurements. Both present the necessary cutting parameters to utilize in the analytical models. In Figure 21 in the last chapter, it is shown this sequence of procedures. Whereas Figure 23 presents the steps for the analytical modeling. Following, the comparison between the GFSE-3D and the state of art's analytical models for the steady and transient state is discussed. Subsequently, the GFSE-3D is validated with thermal measurement results. Afterward, the methodology of the new analytical model for transient cutting is applied to the milling process.

4.1 EXPERIMENTAL RESULTS: PART I

As mentioned in Section 3.2, the orthogonal cutting experiments were performed for a variation of cutting speed $V_c = 100; 120$ and $150\ m/min$ and repeated twice for each velocity. The first measurement constitutes the measurement of the forces, which are necessary to calculate the heat transferred to the tool in the secondary heat source. The second measurement is the high-speed measurement to provide the chip-tool contact length, which is necessary to define the region of the secondary heat source and its heat flux. This approach's steps are present in the flowchart Figure 21.

4.1.1 Cutting Forces Measurement

The resulted forces, cutting force, F_c, and thrust force, F_t, measured by the dynamometer, F_z and F_y, respectively, were analyzed in the software DIAdem. For the velocity of $100m/min$, the results for the repeated experiments can be seen in Figure 33. The first and second columns present the measured signal forces during the cutting for the first and second experiments, respectively. The magnitude of cutting forces was similar in both experiments. The same happens for the thrust force.

Table 4 and Figure 34 shows the effect of cutting speed on the magnitude of thrust force and cutting force. As it can be seen from the results both thrust and tangential forces decrease with increasing cutting speed. It can be observed that both forces decrease with the increasing cutting speed in the range of 100–150 m/min, and the highest cutting forces are recorded at lower cutting speed. As the cutting speed starts increasing, heat generation in the process due to shearing, friction and ploughing increases resulting in thermal softening of the workpiece with the reduction in machining forces. The magnitude of cutting forces was higher than the thrust forces under all cutting speed conditions.

Figure 33 – Force signals for cutting velocity $V_c = 100m/min$. The experiment was repeated twice. Each experiment resulted in cutting force, F_c, and thrust force, F_t.

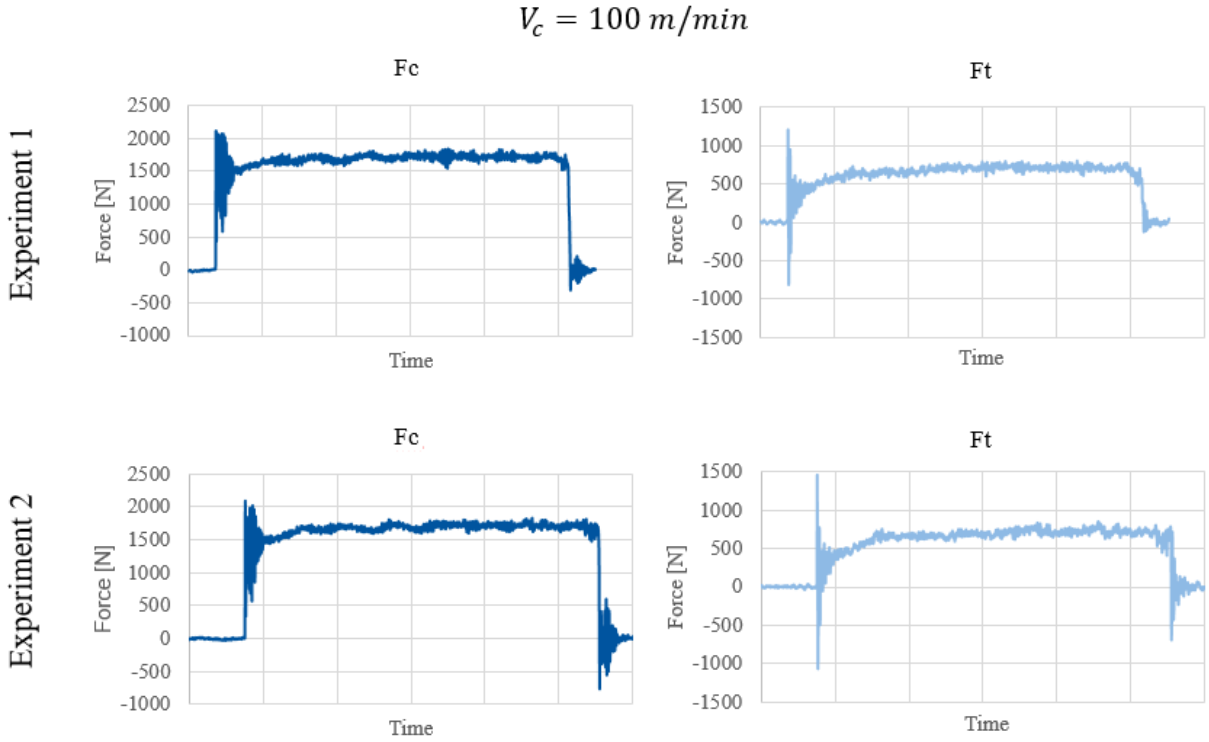

Source: Author.

Table 4 – Average of cutting forces results from the twice repeated experiments.

$V_c\ [m/min]$	$F_c\ [N]$	Max. and min. value of $F_c\ [N]$	$F_t\ [N]$	Max. and min. value of $F_t\ [N]$
100	1700, 185	1497, 604 1837, 398	694, 827	478, 308 830, 823
120	1640, 818	1433, 185 1872, 110	605, 071	339, 502 800, 893
150	1616, 852	1952, 396 1208, 580	535, 962	230, 657 733, 134

4.1.2 High Speed Measurement

The cutting process was captured by an ultra-high-speed camera, which enabled the measuring of the length of tool-chip contact, L_f. The experiments were repeated twice. In Figure 35, it is possible to observe the experiment during the time for the velocity of $V_c = 100\ m/min$. The moment of the first frame (Figure 35a) is before the cutting starts. Figure 35b shows the begging of the cutting process. The next sequences present in each frame the chip formation, until it ends the cutting. Figure 35h shows immediately after the cutting, in which the

Figure 34 – Average of cutting forces results from the twice repeated experiments.

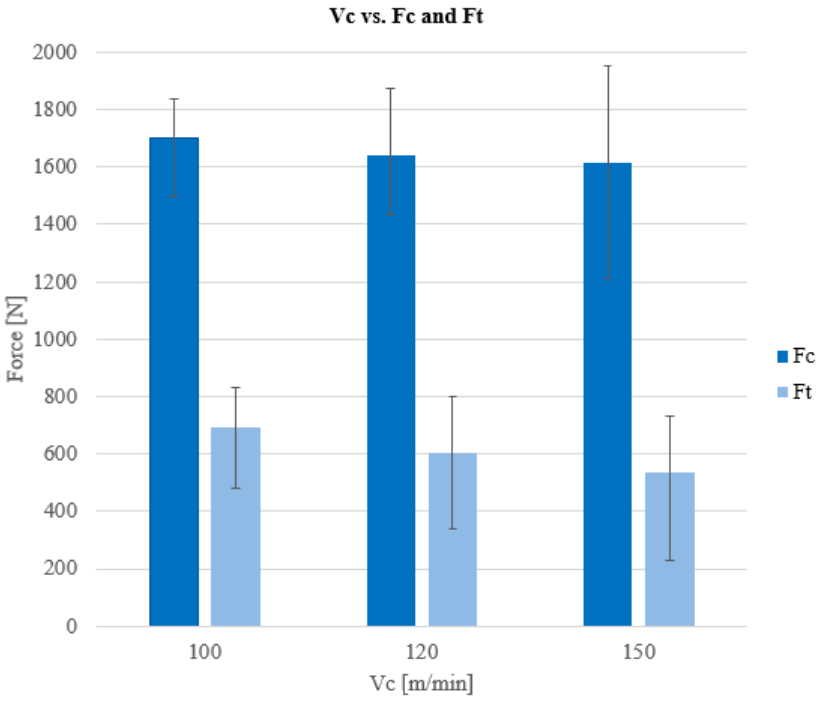

Source: Author.

chip and workpiece have no more contact with the tool.

The chip-tool contact length was measured in the PCC software as in Figure 36, resulting in a value of $0,05mm$ for $V_c = 100\ m/min$. For the same parameter of velocity, Figure 37 presents a microscope photo and a topography of the rake face of the tool after the cutting experiment (upper side view of Figure 35). In Figure 37a, the left side is where happened chip-tool contact. While in Figure 37b, this region is seen on the right side, by the increase in roughness. The topography result presents a similar chip-length contact of approximately $0,05mm$. For all the cutting speed and the repeated tests, the results of L_f can be analyzed in Table 5.

As Figure 21 shows, with the forces during the orthogonal cutting and the chip-tool contact measured, all the necessary parameter's values for the analytical models are obtained. These values are presented in Table 6.

Table 5 – $L_f[mm]$ for different cutting velocities.

$V_c\ [m/min]$	Average of $L_f[mm]$
100	$0,55$
120	$0,7$
150	$0,75$

Figure 35 – Cutting process captured by the ultra-high-speed camera for $V_c = 100\ mm/min$.

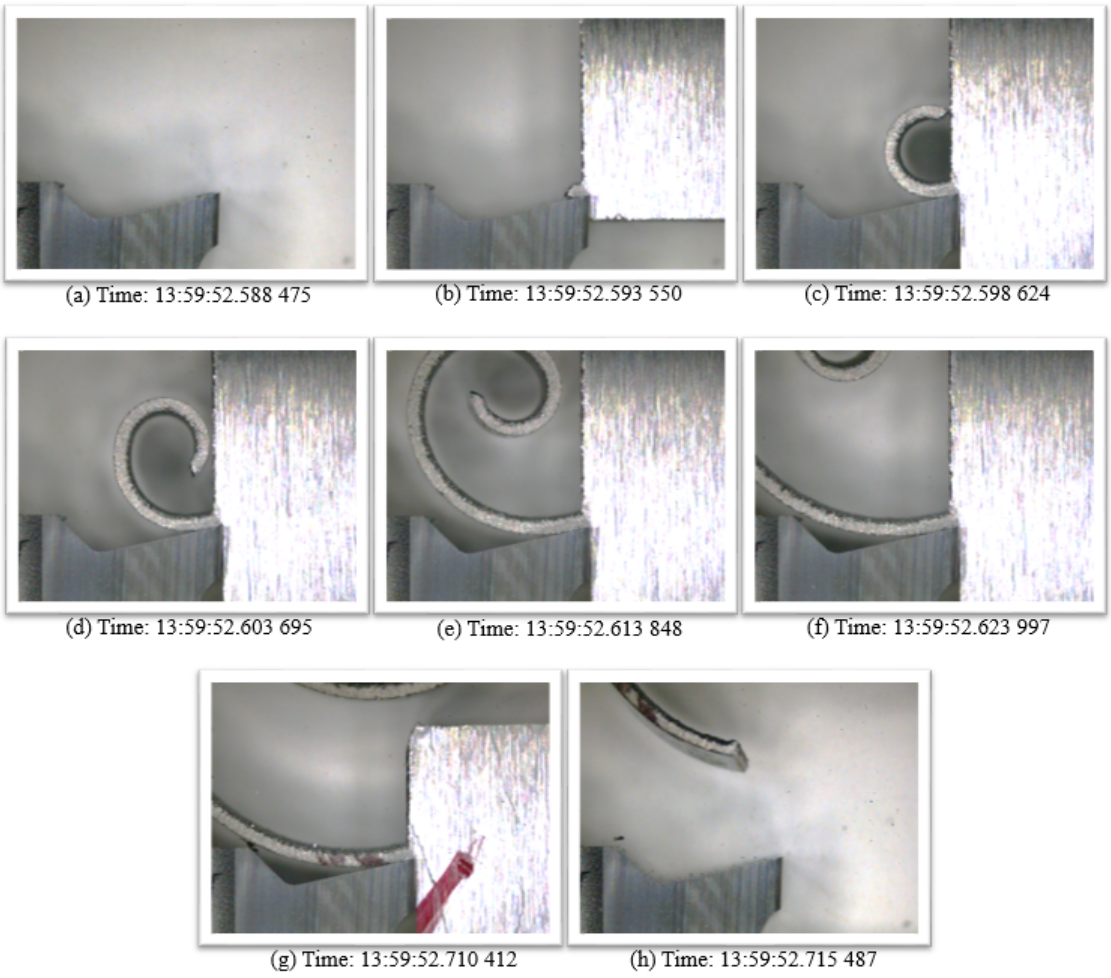

Source: Author.

Table 6 – List of parameter's values for the analytical models (Part II). The ■, ▲ and ★ symbols represent which parameters are necessary for the image method, semi-infinite Green's function solution and three-dimension finite Green's function solution, respectively.

Parameter	**Symbol**	**Value for the respective velocity** $V_c = 100; 120; 150\ [m/min]$
Cutting force	F_c ■▲★	$1700,185\ [N]$
		$1640,818\ [N]$
		$1616,852\ [N]$
Thrust force	F_t ■▲★	$694,827\ [N]$
		$605,071\ [N]$
		$535,962\ [N]$
Chip-tool contact length	L_f ■▲★	$0,55\ [mm]$
		$0,7\ [mm]$
		$0,75\ [mm]$

Figure 36 – L_f measurement for $V_c = 100\ m/min$ in PCC software. Figure (a) shows the region where it is the chip-tool contact, while Figure (b) shows the line of contact in red, which it is measured by the software as d in meters.

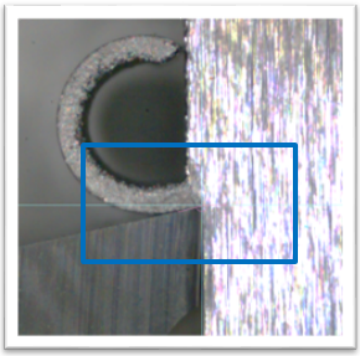

(a) Region of the measurement.

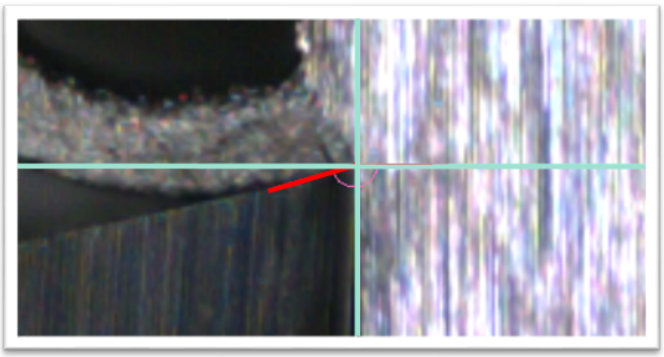

(b) Chip-tool contact.

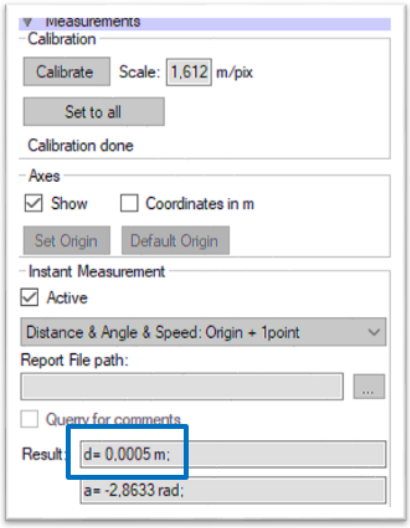

(c) Length's result.

Source: Author.

Figure 37 – Microscope photo and topography of the rake face of the tool for $V_c = 100\ m/min$ test.

(a) Microscope photo.

(b) Topography.

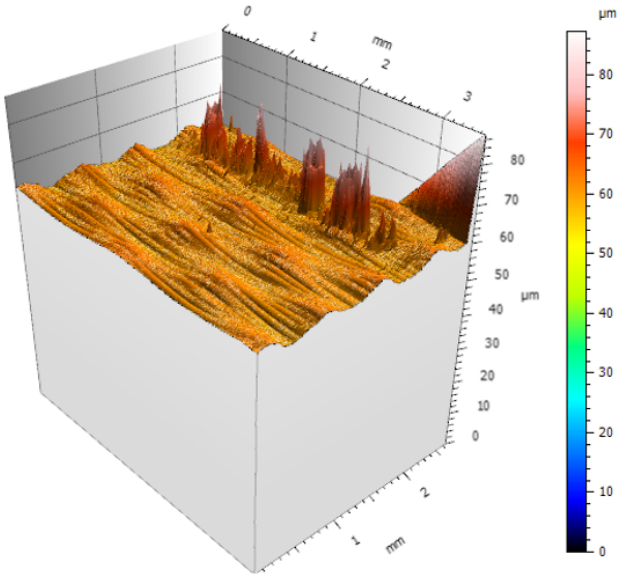

Source: Author.

4.2 ANALYTICAL MODELS

With all the parameter's values defined in Table 1 and Table 6, it is possible to simulate the analytical models with conditions from a real cutting process.

4.2.1 Comparison between Image Method and 3D-Green's Function in Orthogonal Cutting.

The comparison between Image Method and GFSE-3D in orthogonal cutting was presented to observe if the cutting process happens in the transient state and how it differs from the steady-state.

In Figure 38, the analytical model results can be seen for $V_c = 150m/min$. In this graph, it is presented results for image method, i.e., steady-state; GFSE-3D for the cutting time $t_c = 0,08s$ and for a high value of time, both at y for $x = W/2$. The results are as expected, the temperature distribution for the image method is bigger than for GFSE-3D. As the image method was applied for a steady-state, the heat transfer occurs in a longer period of time until reaches a stationary state.

Figure 38 – Temperature (at y for $x = W/2$) for the cutting conditions of $V_c = 150m/min$ for image method, i.e., steady-state; finite three-dimensional Green's Function for the cutting time $t_c = 0,08s$ and for a high value of time $t_{max} = 4,67s$ (maximum time for small cotime for the model assumed).

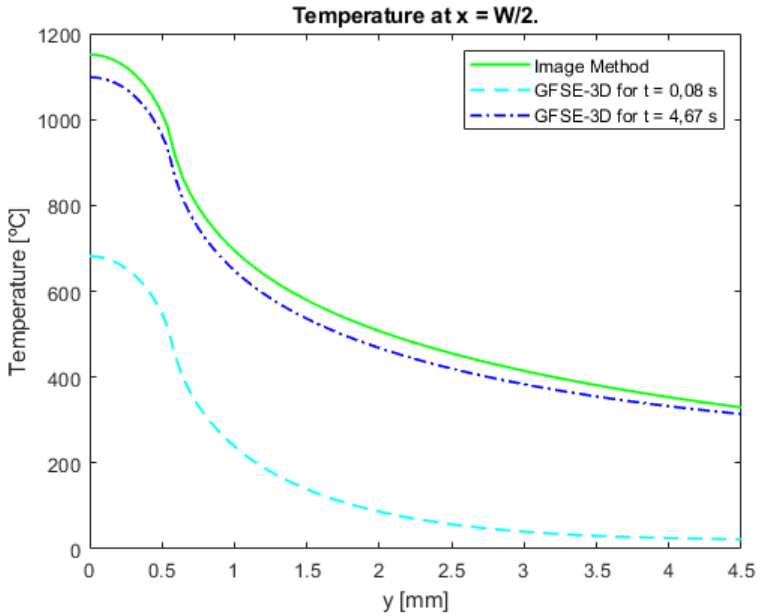

Source: Author.

As presented in Section 3.1.2.2, it was considered small cotime for the Green's Function utilized. This means that for each dimension, each expression used is valid for the condition of $\alpha(t - \tau)/L^2 \leq 0,25$. Considering, the three dimensions and the parameter's values for the cutting speed of $V_c = 150m/min$, the maximum time for a small cotime is $t_{max} = 4,67s$. In

Figure 38 this value is compared, this t_{max} does not reach the steady-state.

Besides applying a high value of time for the GFSE-3D than the cutting time, using t_{max}, both methods' temperature distributions were compared for the same plane in Figure 39. The temperature distribution in the background of the graph is the image method and the temperature distribution in dashed lines is the GFSE-3D. As also observed in Figure 38, the GFSE-3D's temperature is lower than the Image Method's temperature. But both have a similar distribution, with a higher variation near the chip-tool contact. However, the GFSE-3D does not reach the steady-state.

Figure 39 – Temperature distribution at cutting conditions of $V_c = 150m/min$ for image method and GFSE-3D for a $t_{max} = 4,67s$.

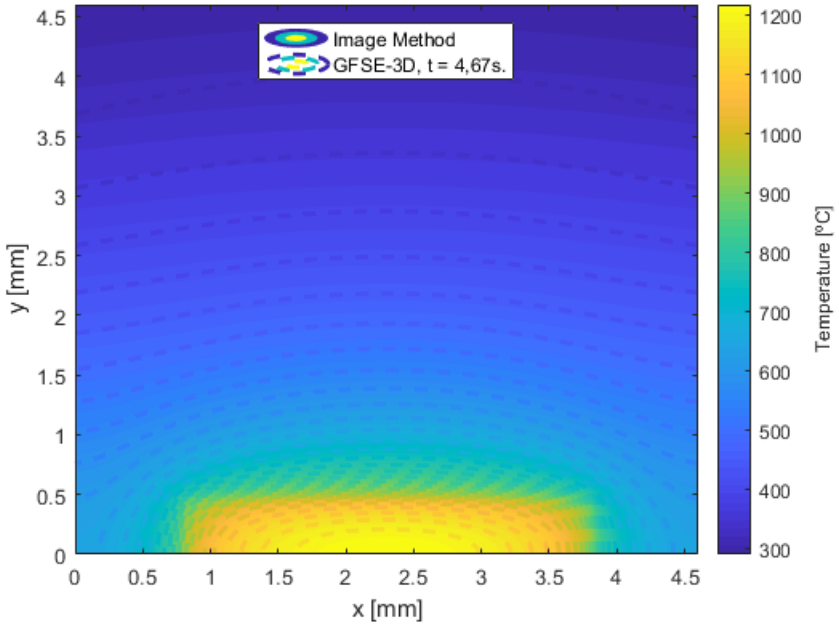

Source: Author.

4.2.2 Comparison between Analytical Models in Transient State in the Cutting Process

The comparison of the tool temperature distribution results between semi-infinite and finite three-dimensional Green's Functions has as purpose to analyze a method used in the literature and a new analytical solution. It is important to remind that both geometry assumptions are different. Besides one having a semi-infinite boundary and the second having a finite boundary, the heat flux part is located in a different position for the tool. The first has the heat distribution in the corner of the rake face (Figure 16), while the second has the heat in the inferior middle of the rake-face plane of the tool (Figure 28). Because of this purpose, the results are presented in the tool lateral face for both methods Figure 40. In addition, the experiment tests measure the lateral face of the tool, which will be present in Section 4.3.

Thus, in Figure 40, the temperature distribution in the lateral tool at cutting conditions of $V_c = 150m/min$ for both methods are presented. The whole length's tool (y-axis) has a value

Figure 40 – Temperature distribution in the lateral tool at cutting conditions of $V_c = 150m/min$ for: (a) GFSE-3D (image on the left side), and (b) semi-infinite Green's Function (image on the right side).

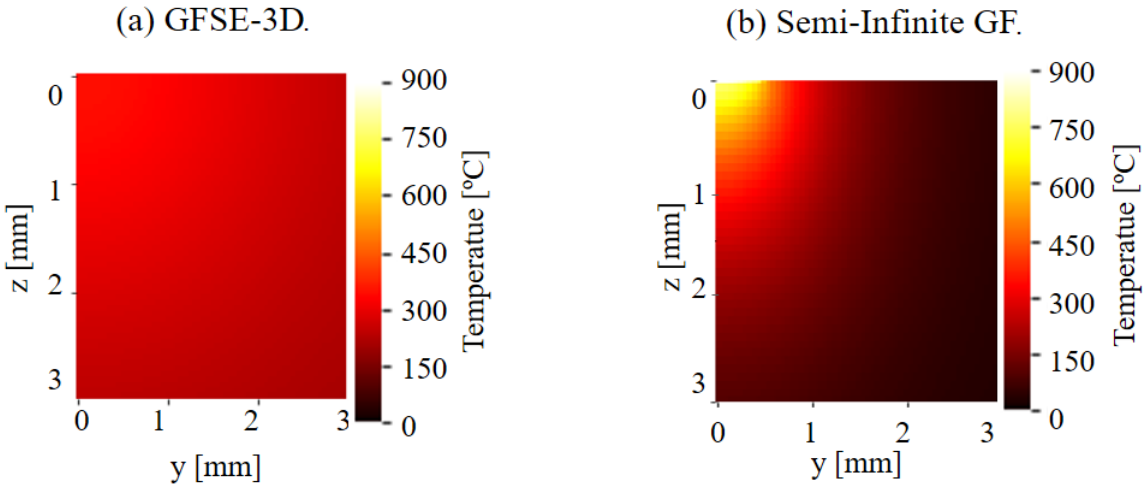

Source: Author.

of $25mm$, which was not plotted completely, for a better visualization of the edge. It is noticed a higher value at the edge for semi-infinite Green's Function (image on the right side), as its heat source is positioned in the corner of the rake face. Furthermore, the temperature distributions of both methods are different. A semi-infinite body will conduct its heat away from the tool differently from a limited boundary.

Besides the distribution of the temperature, it is important to predict the maximum temperature during the cutting, especially in the industry. Thus, the manufacturer can choose the better material to utilize for the tool, for example. Each material has a usable maximum temperature. The maximum application temperature of WC–Co cemented carbides is 800 to $900°C$. Above this temperature, the plastic deformation, caused by softening of the binder phase, leads to tool failure (UHLMANN et al., 2016).

Because of this, the maximum temperature in both methods was analyzed. The maximum temperature at y direction for the semi-infinite Green's Functions is for $x = 0$, while for the finite three-dimensional Green's Functions, $x = W/2$. In Figure 41, the result of this analysis is presented. Semi-infinite Green's Function obtained a higher value than GFSE-3D and a bigger magnitude of $900°C$ (near the plastic deformation temperature). The first presented a possibility to overestimate the maximum temperature, besides not having the same geometry as the orthogonal tests realized in this bachelor thesis.

Furthermore, as presented in Chapter 2.2.2, the consideration of a semi-infinite body of a finite body of thickness L can be represented by a semi-infinite body, $0 < x < \infty$, when the boundary condition at $x = L$ does not influence the temperature distributions near $x = 0$. This happens for the small dimensionless times of $\alpha t/L^2 < 0,05$ (COLE et al., 2010). However, for the parameters of velocity $v_c = 120$ and $150m/min$, this condition is not respected for the

Figure 41 – Temperature in tool at y at cutting conditions of $V_c = 150m/min$ for semi-infinite Green's Function and GFSE-3D.

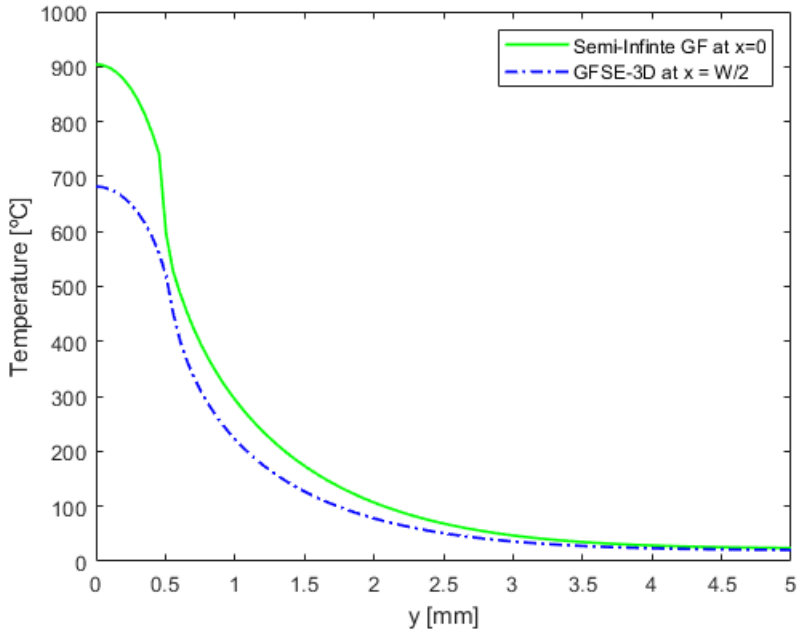

Source: Author.

tool's height (z-dimension) of $5mm$. As for the first cutting velocity, it should be $L_z > 5,35mm$, and for the second, $L_z > 6,42mm$. Nevertheless, for the condition of small cotime utilized in the GFSE-3D model (Chapter 3.1.2.2), $\alpha(t-\tau)/L^2 \leq 0,25$, is reached for all the simulation's parameters.

4.3 EXPERIMENTAL RESULTS: PART II

The thermography experiment captured the temperature distribution by a thermal camera during the cutting process. In Figure 42, it is possible to observe the experiment during the time. The moment of the first Figure 42a is in the begging the cutting. The whole sequence shows in each frame the temperature distribution of the tool and the chip formation, until it ends the cutting. Figure 42f shows the time immediately before the end of the cutting, while Figure 42g shows immediately after the cutting, which the chip has no more contact with the tool, similarly what happens to Figure 35h.

The GFSE-3D was compared to the experimental results. As explained in the methodology the time used for the analytical models was the time of cutting. Because of this, all the experimental test frames used to compare both methods were chosen as the correspondent frame that presents the time immediately before the end of the cutting, for example, Figure 42f. results for the experimental tests and the GFSE-3D results are presented for the three different parameters $V_c = 100; 120; 150m/min$ in Figures 43, 44 and 45. The temperature distribution in the background of the graph is the experiment and the temperature distribution in dashed lines is

Figure 42 – Cutting process captured by the thermal camera for $V_c = 100m/min$.

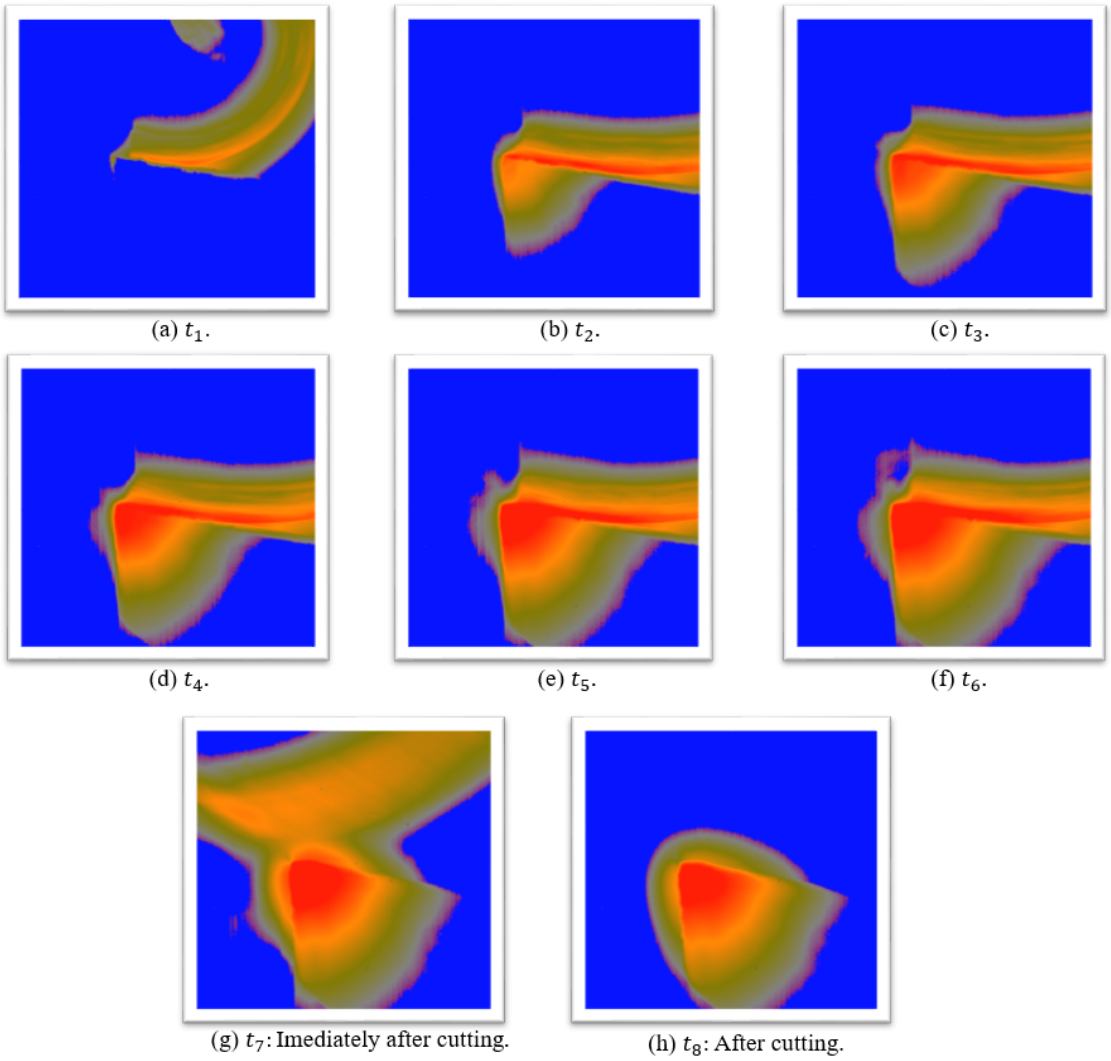

(a) t_1. (b) t_2. (c) t_3.

(d) t_4. (e) t_5. (f) t_6.

(g) t_7: Imediately after cutting. (h) t_8: After cutting.

Source: Author.

the GFSE-3D. For all three different parameters, the temperature distribution for the GFSE-3D model is similar to the experimental result.

Table 7 – Maximum temperature of experimental tests and GFSE-3D analytical results.

$V_c\ [m/min]$	Method	Maximum Temperature $[°C]$	Relative Error
100	Experiment	$367,0729$	$0,13\%$
	GFSE-3D	$366,5957$	
120	Experiment	$369,3487$	$1,07\%$
	GFSE-3D	$365,3978$	
150	Experiment	$363,8994$	$4,40\%$
	GFSE-3D	$347,8918$	

It is possible to notice that the temperature distribution for $V_c = 150m/min$ (Figure 45) has a smaller value of maximum temperature than for the others parameters in Figure 43 and

Figure 43 – Comparison between thermal experiment tests and finite three-dimension Green's Function Solution results for cutting condition of $V_c = 100m/min$. The surface observed is the tool lateral face (Figure 28).

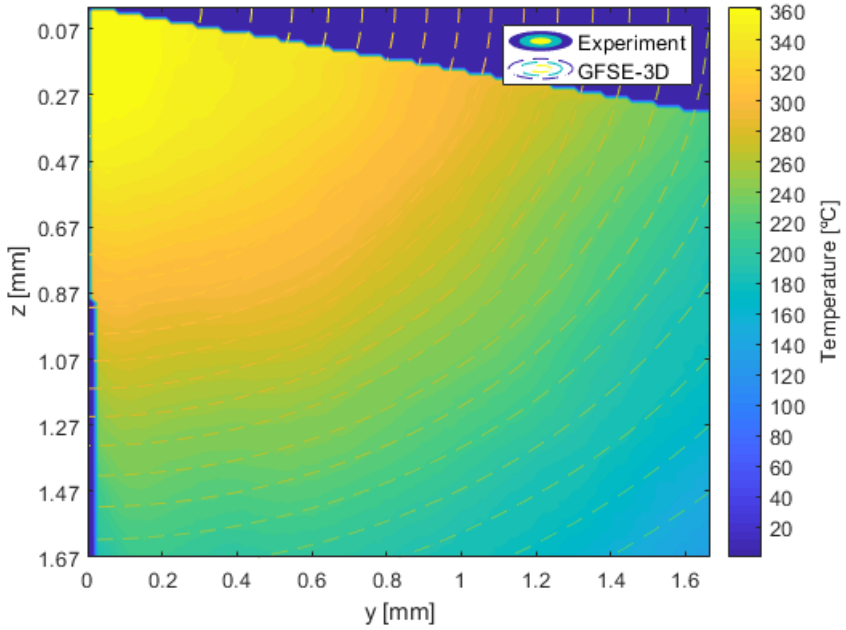

Source: Author.

Figure 44 – Comparison between thermal experiment tests and finite three-dimension Green's Function Solution results for cutting condition of $V_c = 120m/min$. The surface observed is the tool lateral face (Figure 28).

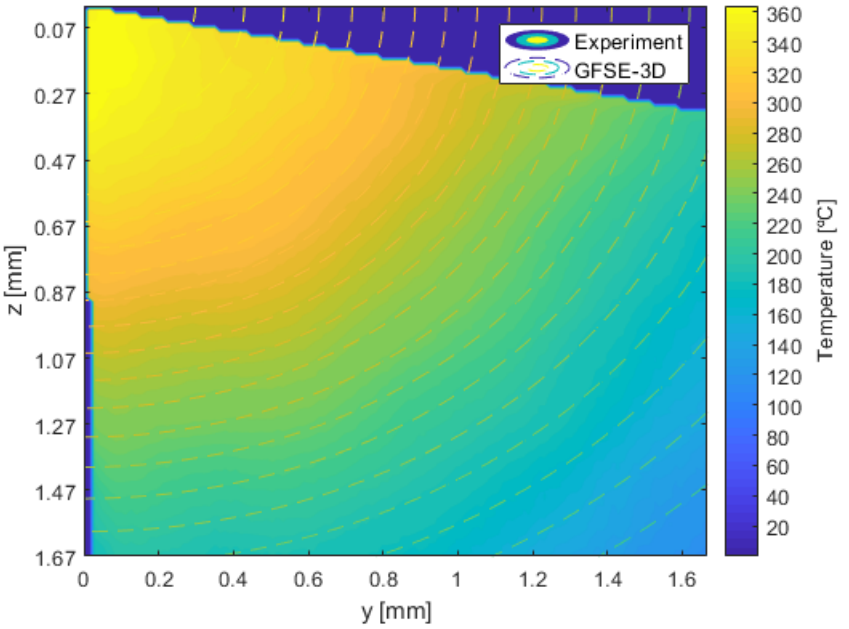

Source: Author.

Figure 44. In Table 7 can be observed the maximum temperature for the experiment test and GFSE-3D model results. For the GFSE-3D method, as higher the cutting speed, V_c, as smaller

Figure 45 – Comparison between thermal experiment tests and finite three-dimension Green's Function Solution results for cutting condition of $V_c = 150m/min$. The surface observed is the tool lateral face (Figure 28).

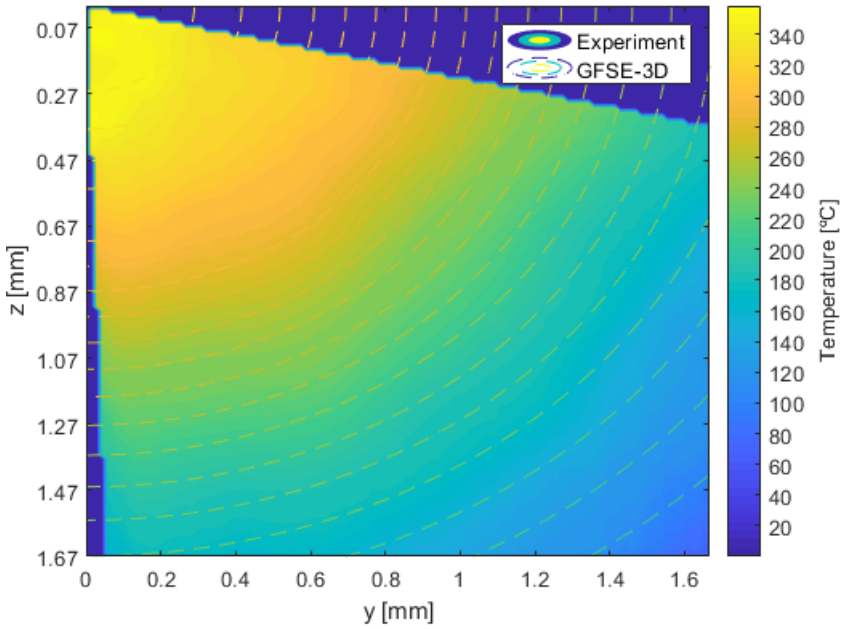

Source: Author.

the maximum temperature, which is expected. How as higher the cutting speed, V_c, as smaller the cutting force (Figure 34). Thus, a smaller value of heat flux is obtained, which results in a smaller temperature.

However, the same does not happen for the experiment results. For the middle velocity, $V_c = 120m/min$, the temperature is higher than for $V_c = 100$ and $V_c = 150m/min$. This happens because, as explained in Chapter 2, the heat partition — coefficient into cutting tool characterizes the proportion of cutting heat flowing into it — is non-constant. Besides that, the literature shows a correlation between the heat partition and the Peclét number, a dimensionless variable correlating with the heat partition into the tool with the undeformed chip thickness as the characteristic length:

$$N_{Pe} = \frac{V_c \cdot h}{\alpha_{tool}} \tag{53}$$

Augspurger (2018) presented that the heat partition into the tool rises with a decreasing undeformed chip thickness and a decreasing cutting velocity. Furthermore, with a rising Peclét number, partition into the tool decreases, probably due to the higher influence of the heat transportation velocity, as presented in Figure 47 for Inconel 718 and AISI 1045 (C45E). Hence, it suffices as a dimensionless number in order to estimate the parameter influence on the heat partition into the tool.

Nevertheless, the maximum temperature from the GFSE-3D method has similar results compared to experimental tests. It presented an acceptable relative error, it reached a maximum

Figure 46 – Relative error between thermal experiment tests and finite three-dimension Green's Function Solution results for cutting condition of $V_c = 150m/min$. The surface observed is the tool lateral face (Figure 28).

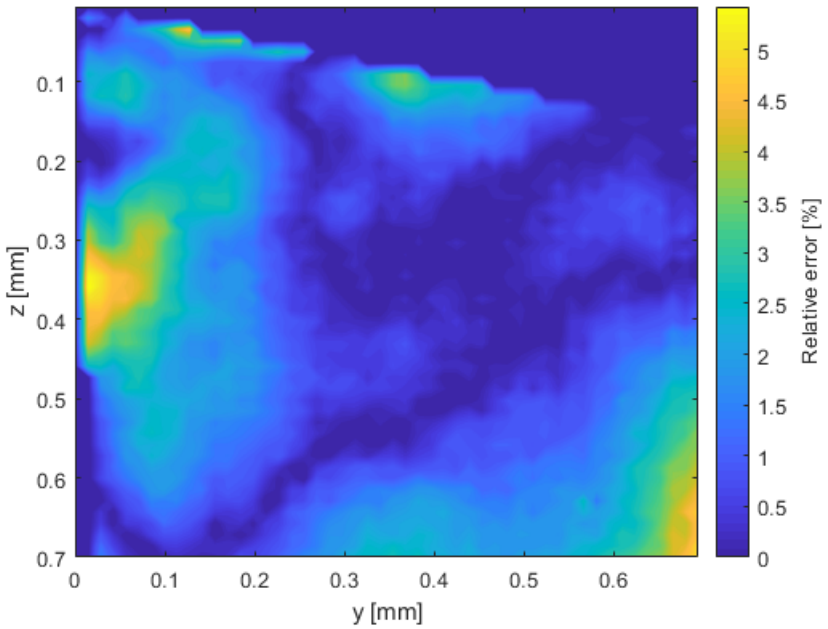

Source: Author.

Figure 47 – Heat partition into the tool and Peclét number.

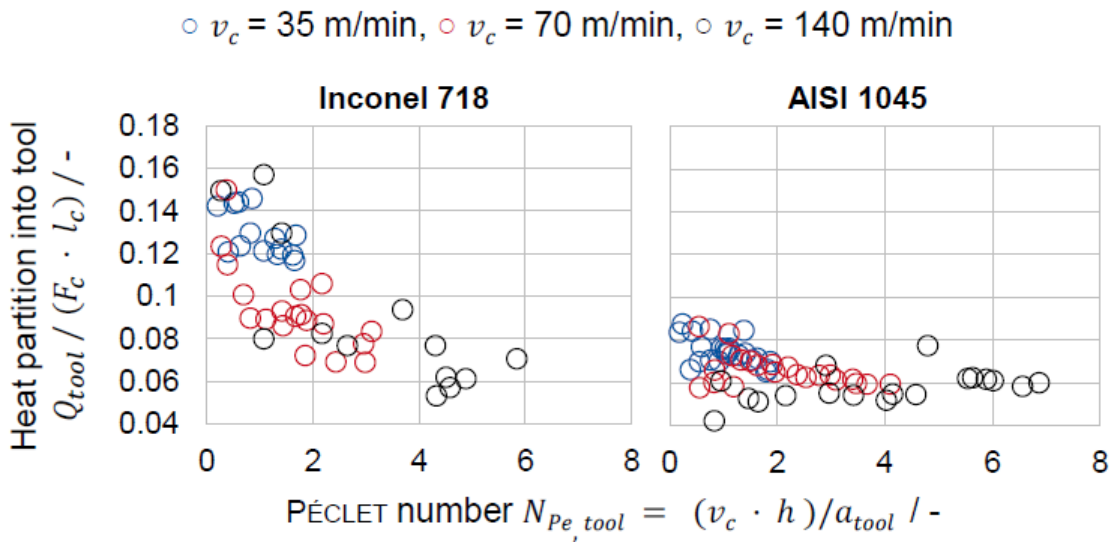

Source: (AUGSPURGER, 2018).

value of $4,40\%$ for $V_c = 150m/min$ (Table 7). As commented before, it is important to predict the maximum temperature during the cutting, for example, the manufacturer can choose a better material to utilize for the tool. Furthermore, this analytical model presented acceptable relative errors. Even for the results from the parameter with the higher relative error of the maximum temperature, its distribution of the relative error between GFSE-3D method and experiment tests

is less than 6% for the edge of the tool, as Figure 46 shows.

4.4 RESULTS OF THE APPLICATION OF THE ANALYTICAL MODEL FOR MILLING PROCESS

Regarding the research hypothesis, it was further investigated if the GFSE-3D model could be used in order to predict time-variant temperature fields in the tool during the cutting process. For this, the analytical GFSE-3D method was analyzed together with the image method at steady-state and other Green's function used in the state of the art of predicting the temperature at the cutting process. Subsequently, the measured transient temperature fields at the tool's lateral face were compared to analytically, time-variant, volumetric temperature fields at defined finite tool for three different parameter settings ($V_c = 100; 120; 150\ m/min$). The results of the analytical temperature fields showed good accordance with the observed conditions in the tool. Those results reveal a valid indicator for a possible step forward to apply the GFSE-3D model to the interrupted cutting process.

Thus, after the analytical model for the cutting process using GFSE-3D developed in this bachelor thesis and its comparison by experimental tests, the methodology was applied to the milling process. For this, the analytical model resolving the transient temperature fields through finite Green's functions, introduced and demonstrated in Chapter 3.1.2.2 and applied to the milling process in Chapter 3.3 was used. It simulated the time-variant temperature fields $T(x, y, z, t)$ in the tool approximated by a finite body during milling as the result of the former empirically modeled transient tool load $\dot{Q}_{tool}(t, v_c, a_e, d, f_z)$.

For $x = 0.8mm$, $y = 0.8mm$ and $z = 0.17mm$, the GFSE-3D for milling process at parameters presented in Chapter 3.3, Table 2, resulted in heat flow into the tool and temperatures at Figure 48. For the heat flow into the tool at the interrupted process, the tool temperature increase depending on the heat's cycles, which range depending on the contact of the tool defined by the cutter rotation angle. Besides the temperature's cyclic variation related directly to the heat's cycle, its magnitude increases.

Yet the heating of the tool was not predicted by the analytical model, and the milling results were not compared directly to experiments. The validation of the modeled temperature fields in the tool was achieved by an experimental setup enabling visibility of the tool's lateral face of an orthogonal cutting process. Those dynamics provide a significant methodology to apply the methodology to an interrupted process and understand thermal cycles at the tool during the milling processes. This kind of analytical simulation is important to understand how those high frequent temperature fluctuations cause alternating strains in the material and could cause tool wear and as well as cracks.

Figure 48 – Heat flow into the tool during the milling process and tool temperature using the GFSE-3D model.

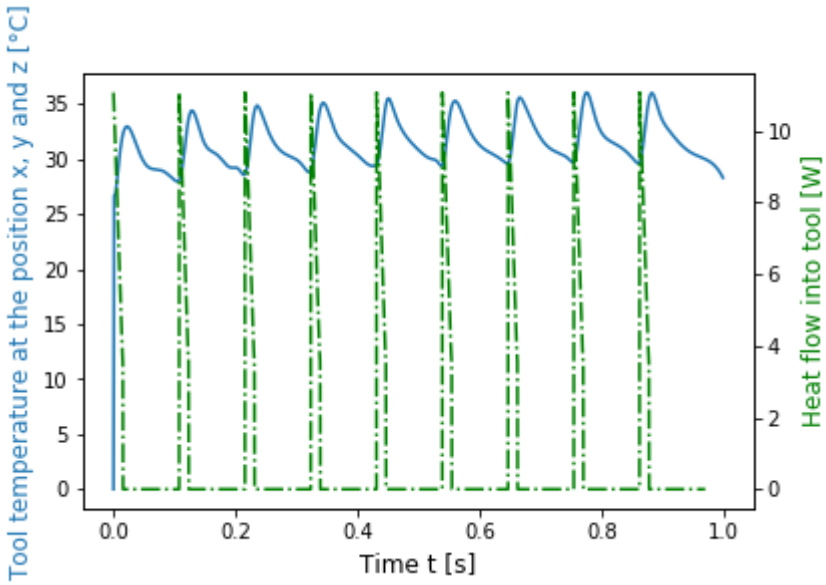

Source: Author.

5 CONCLUSIONS

The main objective of this bachelor thesis is to develop an analytical model of the tool temperature distribution prediction in the cutting process with a new boundary assumption. To accomplish this general objective, firstly, it was compared the new model to the previous analytical models in the state of art for cutting process divided into stationary and transient states. For last, a validation of the new analytical model using finite three-dimensional Green's Function with orthogonal cutting experiments, i.e., continuous cutting, was realized. Finally, after good accordance with the results, it was possible to achieve a step forward: to apply the GFSE-3D model to the interrupted cutting process aiming to present its usability.

With regard to the research hypothesis, it was investigated if the finite three-dimensional Green's functions model can be used in order to predict time-variant temperature fields in the tool. For this purpose, the comparison to the image method together the Jaeger's solutions for a stationary square heat source was realized. Thus, it was confirmed that the parameters utilized in the analytical simulations were in accordance with the transient state. Yet in the analysis of the previous analytical models in the state of the art for the cutting process, the Green's Function for semi-infinite rectangular geometry was investigated. The semi-infinite showed a possibility to overestimate the maximum temperature in comparison to the cutting's conditions analyzed, which presented temperature near the plastic deformation temperature for the edge of the tool. In addition, the finite three-dimensional have more accuracy of the real geometry of the orthogonal tests realized in this bachelor thesis. The condition of small dimensionless times for considering a semi-infinite was not reached for all the cutting parameters. While the finite three-dimensional presented accordance to small cotime condition for all the parameters.

Finally, a validation of the modeled temperature fields in the tool was achieved by an orthogonal cutting experimental setup enabling visibility of the tool's lateral face. Even for the results from the parameter of cutting velocity of $150mm/min$ that presented a higher relative error of the temperature, it obtained less than 6% of relative error for the edge of the tool. After validation of the model, an application of the GFSE-3D model to the milling process as an interrupted cutting was realized. As an interrupted process, it is important to predict its transient temperature, since cyclic heating and cooling may cause cycling strains and alterations of the microstructure and material properties.

Although good accordance of the results between the GFSE-3D model and the orthogonal cutting experiment were obtained, as it was discussed, the heat partition is actually non-constant. Therefore, for future works, the author suggests that the theory of a nonuniform heat partition ratio may be investigated into the analytical model developed in this bachelor thesis. Furthermore, in this work, it was also utilized a constant thermal conductivity as the state of the art for cutting process suggests, but this parameter has a dependence on the temperature.

Since the temperature of the tool can vary significantly due to the heat source in the chip-contact region, a study of the application of a non-constant thermal conductivity might bring a good contribution to the research of the cutting process. In addition, an investigation of a real tool temperature distribution for the milling process in comparison to the results of the application of the analytical model obtained in this work is suggested for future works. Finally, a consideration of the effects of the conductive and the radiation could improve the analytical model developed this bachelor thesis.

REFERENCES

ABUKHSHIM, N.; MATIVENGA, P.; SHEIKH, M. Investigation of heat partition in high speed turning of high strength alloy steel. **International Journal of Machine Tools and Manufacture**, Elsevier, v. 45, n. 15, p. 1687–1695, 2005.

ADMINISTRATION, I.; GROUP, E. P. G. A. M.; BOOTHROYD, G. Temperatures in orthogonal metal cutting. **Proceedings of the Institution of Mechanical Engineers**, SAGE Publications Sage UK: London, England, v. 177, n. 1, p. 789–810, 1963.

AUGSPURGER, T. **Thermal Analysis of the Milling Process**. [S.l.]: Apprimus Wissenschaftsverlag, 2018.

AUGSPURGER, T. et al. Model-based monitoring of temperatures and heat flows in the milling cutter. **The International Journal of Advanced Manufacturing Technology**, Springer, v. 107, n. 9, p. 4231–4238, 2020.

BAOHAI, W. et al. Cutting tool temperature prediction method using analytical model for end milling. **Chinese Journal of Aeronautics**, Elsevier, v. 29, n. 6, p. 1788–1794, 2016.

BECK, J. V.; BLACKWELL, B.; CLAIR JR, C. R. S. **Inverse heat conduction: Ill-posed problems**. [S.l.]: James Beck, 1985.

BHIRUD, N.; GAWANDE, R. Measurement and prediction of cutting temperatures during dry milling: review and discussions. **Journal of the Brazilian Society of Mechanical Sciences and Engineering**, Springer, v. 39, n. 12, p. 5135–5158, 2017.

BLOK, H. Theoretical study of temperature rise at surfaces of actual contact under oiliness lubricating conditions. **Proc. Instn. Mech. Engrs.(General discussion on lubrication and lubricants)**, v. 2, p. 222, 1937.

BONCH-BRUEVICH, V.; TYABLIKOV, S. The green function method in statistical mechanics (english transl.) north holland pub. **Co., Amsterdam**, 1962.

BOOTHROYD, G. Photographic technique for the determination of metal cutting temperatures. **British Journal of Applied Physics**, IOP Publishing, v. 12, n. 5, p. 238, 1961.

BRÖMMELHOFF, K. et al. Space resolved microstructural characteristics in the chip formation zone of orthogonal cut c45e steel samples characterized by diffraction experiments. **Journal of Materials Processing Technology**, Elsevier, v. 213, n. 12, p. 2211–2216, 2013.

CANNELL, D. George green: an enigmatic mathematician. **The American Mathematical Monthly**, Taylor & Francis, v. 106, n. 2, p. 136–151, 1999.

CAPELLO, E. Residual stresses in turning: Part i: Influence of process parameters. **Journal of materials processing technology**, Elsevier, v. 160, n. 2, p. 221–228, 2005.

CARVALHO, S. et al. Temperature determination at the chip–tool interface using an inverse thermal model considering the tool and tool holder. **Journal of materials processing technology**, Elsevier, v. 179, n. 1-3, p. 97–104, 2006.

CHAKRAVERTI, G.; PANDEY, P.; MEHTA, N. Analysis of tool temperature fluctuation in interrupted cutting. **Precision engineering**, Elsevier, v. 6, n. 2, p. 99–105, 1984.

CHAO, B. The significance of the thermal number in metal machining. **Trans. ASME**, v. 75, p. 109–120, 1953.

CHEN, W.-C.; TSAO, C.-C.; LIANG, P.-W. Determination of temperature distributions on the rake face of cutting tools using a remote method. **International communications in heat and mass transfer**, Elsevier, v. 24, n. 2, p. 161–170, 1997.

CHENWEI, S. et al. Prediction of machining-induced residual stress in orthogonal cutting of ti6al4v. **The International Journal of Advanced Manufacturing Technology**, Springer Nature BV, v. 107, n. 5-6, p. 2375–2385, 2020.

CHENWEI, S. et al. An improved analytical model of cutting temperature in orthogonal cutting of ti6al4v. **Chinese Journal of Aeronautics**, Elsevier, v. 32, n. 3, p. 759–769, 2019.

CHOU, Y. K.; SONG, H. Thermal modeling for white layer predictions in finish hard turning. **International Journal of Machine Tools and Manufacture**, Elsevier, v. 45, n. 4-5, p. 481–495, 2005.

COLE, K. et al. **Heat conduction using Greens functions**. [S.l.]: Taylor & Francis, 2010.

COMMITTEE, A. I. H. et al. **ASM Handbook, Volume 16-Machining**. [S.l.]: ASM International., 1989.

DAVIES, M. et al. On the measurement of temperature in material removal processes. **CIRP annals**, Elsevier, v. 56, n. 2, p. 581–604, 2007.

DEPPERMANN, M.; KNEER, R. Determination of the heat flux to the workpiece during dry turning by inverse methods. **Production Engineering**, Springer, v. 9, n. 4, p. 465–471, 2015.

DEUTSCHES INSTITUT FüR NORMUNG (ED.). **DIN 8580**: Fertigungsverfahren – begriffe, einteilung. Beuth, Berlin, 2003.

DINC, C.; LAZOGLU, I.; SERPENGUZEL, A. Analysis of thermal fields in orthogonal machining with infrared imaging. **Journal of materials processing technology**, Elsevier, v. 198, n. 1-3, p. 147–154, 2008.

FENG, Y. et al. Analytical prediction of temperature in laser-assisted milling with laser preheating and machining effects. **The International Journal of Advanced Manufacturing Technology**, Springer, v. 100, n. 9, p. 3185–3195, 2019.

FENG, Y.; PAN, Z.; LIANG, S. Y. Temperature prediction in inconel 718 milling with microstructure evolution. **International Journal of Advanced Manufacturing Technology**, v. 95, 2018.

FERNANDES, A. P. et al. Use of 3d-transient analytical solution based on green's function to reduce computational time in inverse heat conduction problems. **Applied Mathematical Modelling**, Elsevier, v. 34, n. 12, p. 4040–4049, 2010.

GIERLINGS, S. **Model-based temperature monitoring for broaching safety-critical aero engine components**. [S.l.]: Apprimus Wissenschaftsverlag, 2015.

HAHN, R. S. On the temperature developed at the shear plane in the metalcutting process. In: ASME-AMER SOC MECHANICAL ENG 345 E 47TH ST, NEW YORK, NY 10017. **Journal of Applied Mechanics-Transactions of the ASME**. [S.l.], 1951. v. 18, n. 3, p. 323–323.

HU, C. et al. Thermal-mechanical model for cutting with negative rake angle based on a modified slip-line field approach. **International Journal of Mechanical Sciences**, Elsevier, v. 164, p. 105167, 2019.

HU, C. et al. Three-dimensional analytical modeling of cutting temperature for round insert considering semi-infinite boundary and non-uniform heat partition. **International Journal of Mechanical Sciences**, Elsevier, v. 155, p. 536–553, 2019.

HU, C. et al. Cutting temperature prediction in negative-rake-angle machining with chamfered insert based on a modified slip-line field model. **International Journal of Mechanical Sciences**, Elsevier, v. 167, p. 105273, 2020.

HUANG, Y.; LIANG, S. Modelling of the cutting temperature distribution under the tool flank wear effect. **Proceedings of the Institution of Mechanical Engineers, Part C: Journal of Mechanical Engineering Science**, SAGE Publications Sage UK: London, England, v. 217, n. 11, p. 1195–1208, 2003.

HUANG, Y.; LIANG, S. Y. Cutting temperature modeling based on non-uniform heat intensity and partition ratio. **Machining science and technology**, Taylor & Francis, v. 9, n. 3, p. 301–323, 2005.

ISLAM, C. **A transient thermal model for machining**. Tese (Doutorado) — University of British Columbia, 2018.

JAEGER, J. C. Moving sources of heat and the temperature of sliding contacts. In: **Proceedings of the royal society of New South Wales**. [S.l.: s.n.], 1942. v. 76, p. 203–224.

JAEGER, J. C.; CARSLAW, H. S. **Conduction of heat in solids**. [S.l.]: Clarendon P, 1959.

JEELANI, S. Measurement of temperature distribution in machining using ir photography. **Wear**, Elsevier, v. 68, n. 2, p. 191–202, 1981.

JIANG, F. et al. Analytical modeling and experimental investigation of tool and workpiece temperatures for interrupted cutting 1045 steel by inverse heat conduction method. **Journal of Materials Processing Technology**, Elsevier, v. 213, n. 6, p. 887–894, 2013.

KARAGUZEL, U.; BAKKAL, M.; BUDAK, E. Modeling and measurement of cutting temperatures in milling. **Procedia CIRP**, Elsevier, v. 46, p. 173–176, 2016.

KARAGUZEL, U.; BUDAK, E. Investigating effects of milling conditions on cutting temperatures through analytical and experimental methods. **Journal of Materials Processing Technology**, Elsevier, v. 262, p. 532–540, 2018.

KARPAT, Y.; ÖZEL, T. Predictive analytical and thermal modeling of orthogonal cutting process—part i: predictions of tool forces, stresses, and temperature distributions. 2006.

KARPAT, Y.; ÖZEL, T. Predictive analytical and thermal modeling of orthogonal cutting process—part ii: effect of tool flank wear on tool forces, stresses, and temperature distributions. 2006.

KARPAT, Y.; ÖZEL, T. Analytical and thermal modeling of high-speed machining with chamfered tools. **Journal of Manufacturing Science and Engineering**, American Society of Mechanical Engineers Digital Collection, v. 130, n. 1, 2008.

KLOCKE, F.; KUCHLE, A. Fundamentals of cutting. In: **Manufacturing Processes 1**. [S.l.]: Springer, 2011. p. 39–94.

KLOCKE, F.; KUCHLE, A. Process design and process monitoring. In: **Manufacturing Processes 1**. [S.l.]: Springer, 2011. p. 339–382.

KLOCKE, F.; KUCHLE, A. Processes with rotational primary movement. In: **Manufacturing Processes 1**. [S.l.]: Springer, 2011. p. 383–444.

KOMANDURI, R. Machining and grinding: A historical review of the classical papers. 1993.

KOMANDURI, R.; HOU, Z. B. Thermal modeling of the metal cutting process—part i: temperature rise distribution due to shear plane heat source. **International Journal of Mechanical Sciences**, Elsevier, v. 42, n. 9, p. 1715–1752, 2000.

KOMANDURI, R.; HOU, Z. B. Thermal modeling of the metal cutting process—part ii: temperature rise distribution due to frictional heat source at the tool–chip interface. **International Journal of Mechanical Sciences**, Elsevier, v. 43, n. 1, p. 57–88, 2001.

KOMANDURI, R.; HOU, Z. B. Thermal modeling of the metal cutting process—part iii: temperature rise distribution due to the combined effects of shear plane heat source and the tool–chip interface frictional heat source. **International Journal of Mechanical Sciences**, Elsevier, v. 43, n. 1, p. 89–107, 2001.

KRAEMER, G. **Beitrag zur Erkenntnis der beim Drehen auftretenden Temperaturen und deren Messung mit einem Gesamtstrahlungsempfänger**. Tese (Doutorado) — Technische Hochschule hannover, 1937.

LANDWEHR, M. **Prediction and Compensation of Part Distortion Caused by Residual Stresses. Cooperation with Laboratory for Machine Tools and Production Engineering (WZL) of RWTH Aachen University**. 2021. https://predictionandcompensationofpartdistortion.dashboards.vfk.ipt.fraunhofer.de/. Accessed: 2021-10-22.

LAUSCHER, J. **Turning mit Siliciumnitrid-Schneidkeramik,**. Tese (Doutorado) — RWTH-Aachen, 1989.

LEONE, W. Distribution of shear-zone heat in metal cutting. In: ASME. [S.l.], 1953.

LIEW, W.; HUTCHINGS, I.; WILLIAMS, J. Friction and lubrication effects in the machining of aluminium alloys. **Tribology Letters**, Springer, v. 5, n. 1, p. 117–122, 1998.

LIMA, F.; MACHADO, A.; GUIMARAES, G. Experimental heat flux and cutting temperature estimation. In: **Proceedings of the Third International Conference on Metal Cutting and High Speed Machining, Metz**. [S.l.: s.n.], 2001. v. 1, p. 25–34.

LIN, S. et al. An investigation of workpiece temperature variation in end milling considering flank rubbing effect. **International Journal of Machine Tools and Manufacture**, Elsevier, v. 73, p. 71–86, 2013.

LIU, J. et al. Prediction of heat transfer process in helical milling. **The International Journal of Advanced Manufacturing Technology**, Springer, v. 72, n. 5-8, p. 693–705, 2014.

LOEWEN, E. On the analysis of cutting-tool temperatures. **Tras. ASME**, v. 76, p. 217, 1954.

MA, Y. et al. Prediction of surface residual stress after end milling based on cutting force and temperature. **Journal of Materials Processing Technology**, Elsevier, v. 235, p. 41–48, 2016.

MAGDA, D. Understanding the effect of residual stresses on surface integrity and how to measure them by a non destructive method. In: **2008 Annual Conference & Exposition**. [S.l.: s.n.], 2008. p. 13–1314.

MARTELLOTTI, M. An analysis of the milling process. **Trans ASME**, v. 63, p. 677, 1941.

MAYER, E. **Die Infrarot-Foto-Thermometrie, ein neues Arbeitsverfahren der Zerspanungsforschung**. Tese (Doutorado) — Technische Universität Berlin, 1966.

MERCHANT, M. E. Basic mechanics of the metal-cutting process. 1944.

MERCHANT, M. E. Mechanics of the metal cutting process. i. orthogonal cutting and a type 2 chip. **Journal of applied physics**, American Institute of Physics, v. 16, n. 5, p. 267–275, 1945.

MEURER, M. et al. Cutting force based surface integrity soft-sensor when hard machining aisi 4140. **tm-Technisches Messen**, De Gruyter Oldenbourg, v. 87, n. 11, p. 683–693, 2020.

MIRKOOHI, E.; BOCCHINI, P.; LIANG, S. Y. Analytical temperature predictive modeling and non-linear optimization in machining. **The International Journal of Advanced Manufacturing Technology**, Springer, v. 102, n. 5, p. 1557–1566, 2019.

MORSE, P. M.; FESHBACH, H. Methods of theoretical physics. **American Journal of Physics**, American Association of Physics Teachers, v. 22, n. 6, p. 410–413, 1954.

M'SAOUBI, R.; CHANDRASEKARAN, H. Experimental study and modelling of tool temperature distribution in orthogonal cutting of aisi 316l and aisi 3115 steels. **The International Journal of Advanced Manufacturing Technology**, Springer, v. 56, n. 9, p. 865–877, 2011.

NEE, A. Y. **Handbook of manufacturing engineering and technology**. [S.l.]: Springer, 2015.

NING, J.; LIANG, S. Y. Prediction of temperature distribution in orthogonal machining based on the mechanics of the cutting process using a constitutive model. **Journal of Manufacturing and Materials Processing**, Multidisciplinary Digital Publishing Institute, v. 2, n. 2, p. 37, 2018.

NING, J.; LIANG, S. Y. A comparative study of analytical thermal models to predict the orthogonal cutting temperature of aisi 1045 steel. **The International Journal of Advanced Manufacturing Technology**, Springer, v. 102, n. 9, p. 3109–3119, 2019.

NING, J.; LIANG, S. Y. Predictive modeling of machining temperatures with force–temperature correlation using cutting mechanics and constitutive relation. **Materials**, Multidisciplinary Digital Publishing Institute, v. 12, n. 2, p. 284, 2019.

ONYECHI, P. C.; OLUWADARE, B. S.; OBUKA, N. Analytical modeling of temperature distribution in metal cutting: finite element approach. **Int. J. Eng. Sci**, v. 2, n. 4, p. 17, 2013.

OTAI, D. **DIN C45E steel**. 2020. Disponível em: https://www.otaisteel.com/products/carbon-steel/din-c45e-steel-ck45-carbon-structural-steel-din-17200-en10083/. Acesso em: 13 Jan 2022.

OXLEY, P. L. B. **The mechanics of machining: an analytical approach to assesing machinability**. [S.l.]: Ellis Horwood, 1989.

OZISIK, M. Heat conduction, john willey & sons. **Inc., New York**, 1993.

RADULESCU, R.; KAPOOR, S. An analytical model for prediction of tool temperature fields during continuous and interrupted cutting. 1994.

RIBEIRO, S. et al. Estimation of a moving heat source due to a micromilling process using the modified tfbgf technique. **Mathematical Problems in Engineering**, Hindawi, v. 2018, 2018.

RICHARDSON, D.; KEAVEY, M.; DAILAMI, F. Modelling of cutting induced workpiece temperatures for dry milling. **International Journal of Machine Tools and Manufacture**, Elsevier, v. 46, n. 10, p. 1139–1145, 2006.

ROSENTHAL, D. The theory of moving sources of heat and its application of metal treatments. **Transactions of ASME**, v. 68, p. 849–866, 1946.

SALMON, R.; MCCULLOCH, G.; RICE, W. Isothermal patterns in cutting tools of different face lengths. **Annals of the CIRP**, v. 16, n. 3, p. 217–222, 1968.

SATO, M.; TAMURA, N.; TANAKA, H. Temperature variation in the cutting tool in end milling. **Journal of Manufacturing Science and Engineering**, American Society of Mechanical Engineers Digital Collection, v. 133, n. 2, 2011.

SCHWERD, F. über die bestimmung des temperaturfeldes beim spanablauf. **Zeitschrift des VDI**, v. 77, n. 9, p. 211–216, 1933.

SHAW, M. C.; COOKSON, J. **Metal cutting principles**. [S.l.]: Oxford university press New York, 2005. v. 2.

STEPHENSON, D. Tool-work thermocouple temperature measurements—theory and implementation issues. 1993.

STEPHENSON, D. A.; AGAPIOU, J. S. **Metal cutting theory and practice**. [S.l.]: CRC press, 2018.

STEPHENSON, D. A.; ALI, A. Tool temperatures in interrupted metal cutting. 1992.

TRIGGER, K. Progress report no. 1 on tool-chip interface temperatures. **Transactions of the ASME**, v. 70, p. 91–98, 1948.

TRIGGER, K. Progress report no. 2 on tool-chip interface temperatures. **Transactions of the ASME**, v. 71, p. 163–174, 1949.

TRIGGER, K. An analytical evaluation of metal-cutting temperatures. **Trans. ASME**, v. 73, p. 57, 1951.

TRIGGER, K.; CHAO, B. Temperature distribution at the tool-chip interface in metal cutting. **Trans. ASME**, v. 77, p. 1107–1120, 1955.

UEDA, T. et al. Temperature on flank face of cutting tool in high speed milling. **CIRP Annals**, Elsevier, v. 50, n. 1, p. 37–40, 2001.

UHLMANN, E. et al. Cutting and drilling of metals and other materials: a comparison. Elsevier, 2016.

VEIGA, F. et al. Analytical thermal model of orthogonal cutting process for predicting the temperature of the cutting tool with temperature-dependent thermal conductivity. **International Journal of Mechanical Sciences**, Elsevier, v. 204, p. 106524, 2021.

VERBEEK, H. Drp no. 359477. **Klasse 49a, Gruppe**, v. 3601, 1920.

VORNBERGER, A. et al. Influence of cemented carbide composition on cutting temperatures and corresponding hot hardnesses. **Materials**, Multidisciplinary Digital Publishing Institute, v. 13, n. 20, p. 4571, 2020.

WANG, Y. et al. Modeling of temperature distribution in turning of ti-6al-4v with liquid nitrogen cooling. **The International Journal of Advanced Manufacturing Technology**, Springer, v. 107, n. 1, p. 451–462, 2020.

XIONG, Y. et al. Analytical model of workpiece temperature in end milling in-situ tib2/7050al metal matrix composites. **International Journal of Mechanical Sciences**, Elsevier, v. 149, p. 285–297, 2018.

YAN, S. et al. Modeling and analysis of coated tool temperature variation in dry milling of inconel 718 turbine blade considering flank wear effect. **Journal of Materials Processing Technology**, Elsevier, v. 214, n. 12, p. 2985–3001, 2014.

ZHAO, J.; LIU, Z. Modelling for prediction of time-varying heat partition coefficient at coated tool-chip interface in continuous turning and interrupted milling. **International Journal of Machine Tools and Manufacture**, Elsevier, v. 147, p. 103467, 2019.

ZHOU, R. Analytical model of workpiece surface temperature prediction in 4-axis milling process. **The International Journal of Advanced Manufacturing Technology**, Springer, v. 111, n. 7, p. 2155–2162, 2020.